7-20-2015

Development of Polymer Composite Based Enabling Technologies for Lab-on-a-Chip Devices

Vinicio Carias
University of South Florida, vinicio@mail.usf.edu

Development of Polymer Composite Based Enabling Technologies for Lab-on-a-Chip Devices

by

Vinicio Carias

A dissertation submitted in partial fulfillment
of the requirements for the degree of
Doctor of Philosophy
Department of Chemical and Biomedical Engineering
College of Engineering
University of South Florida

Co-Major Professor: Ryan Toomey, Ph.D.
Co-Major Professor: Jing Wang, Ph.D.
Subhra Mohapatra, Ph.D.
Nathan Gallant, Ph.D.
Robert Frisina, Ph.D.

Date of Approval:
July 20, 2015

Keywords: Smart Materials, Microfluidics, AC Magnetic Hyperthermia, Photo-crosslinking, Photo-deprotection

DEDICATION

I would like to dedicate this dissertation to my mother, Adonia and my father, Rafael. This accomplishment would not be possible without your continuous prayers, love, and support. I love you both very much.

Also, in loving memory of my grandmother, Petrona Carias, who would call me Dr. Carias as a child. She was always intrigued by my constant questions and curiosity. I wish you were here to share this accomplishment with me.

ACKNOWLEDGMENTS

First and foremost I would like to thank God, for His grace and many blessings throughout my doctoral journey. Thank You for making all things work together for my good.

I would like to express my deepest gratitude and appreciation to my advisors, Dr. Ryan Toomey and Dr. Jing Wang, for their excellent guidance, mentorship, and for molding me into the researcher that I am today. I owe my academic success to you. I would also like to thank my committee members: Dr. Subhra Mohapatra, Dr. Nathan Gallant, and Dr. Robert Frisina for their invaluable feedback and supervision of this work.

Subsequent, I would like to thank my laboratory members from both, Dr. Toomey's group and Dr. Wang's group. Their friendship and support has been vital. They continuously made me feel like I had two USF families I could always reach out to for both research and personal encouragement.

Developing as a leader has always been important to me. Therefore, I would like to thank Dr. Karen Liller for selecting me to take part in the first cohort of the Doctoral Student Leadership Institute (DSLI), allowing me to home in on my leadership style and abilities. I would also like to thank the DSLI Fellows for their friendship and great leadership discussions during our leadership journal club. A big thank you to Dr. Thomas Weller for being my leadership mentor and allow me to learn from his leadership methods.

I offer my profound gratitude to Dr. Jürgen Rühe and Dr. Oswald Prucker for being my research advisors during my stay at the University of Freiburg-IMTEK, Freiburg, Germany.

Thank you for taking me in as one of your own. I would also like to thank Jan-Niklas Schönberg, Marc Zinggeler, Vitaliy Kondrashov, Sirsa Poomkeaw, and Sharareh Asiaee for their friendship and many helpful research discussions during my stay in Germany.

I am extremely grateful to Dr. Javier Alonso Masa and Kristen Stojak from the Functional Materials Laboratory in the USF Department of Physics for allowing me to use their magnetic induction heating system. The magnetic hyperthermia part of this dissertation would not have been possible without their help.

I also express my gratitude to Mr. Bernard Batson for being instrumental in me becoming a USF graduate student and for always looking out for me. I am also thankful to the Bridge to the Doctorate family for their friendship and mentorship

I would like to extend my sincere thanks to my family and friends for being there for me throughout my doctoral process. I would like to give a special thank you to my parents. They have shown me through their sacrifices that success is obtained through hard work and perseverance. Last, I would like to thank Mariana Fackos for being an integral part of my support system from the very beginning of my academic voyage.

TABLE OF CONTENTS

LIST OF TABLES

LIST OF FIGURES

ABSTRACT

This dissertation presents enabling technologies to fabricate thermo-responsive polymer composite based Lab-on-a-Chip (LOC) devices. LOC devices, also known as micro-total-analytical systems (microTAS) or microfluidic devices can amalgamate miniaturized laboratory functions on a single chip. This significant size reduction decreases the amount of required fluid volumes down to nano or pico-liters. The main commercial application of LOC devices is the biomedical fields. However, these devices are anticipated to make a technological revolution similar to the way miniaturization changed computers. In fact, medical and chemical analyses are predicted to shift from room-sized laboratories to hand-held portable devices.

This dissertation is divided into three technologies. First, a series of terpolymer systems were synthesized and characterized to fabricate crosslinked coatings for phototunable swelling and create chemically patterned regions in order to conjugate cationic markers, proteins, or nanoparticles to the terpolymer coating. Second, antifouling surfaces were fabricated using magnetic thermo-responsive hydrogel structures via soft lithography. The structures were remote control activated with the use of AC magnetic fields. Finally, in order for LOC devices to fulfill its promise of bringing a laboratory to a hand-held device, they will have to be integrated with CMOS technology. Packaging will play a crucial role in this process. The last section will focus on the importance of coefficient of thermal expansion (CTE) mismatch in multi-chip modules.

For the first technology, multi-functionalized terpolymer systems have been developed comprising of three units: N-isopropylacrylamide (NIPAAm), a stimuli responsive monomer that swells and collapses in response to temperature; methacryloxybenzophenone (MaBP), a photo-crosslinkable monomer that is activated at λ = 365 nm; and phenacyl methacrylate (PHEm), a photolabile protected functional group that generates localized free carboxyl groups in response to deprotection at λ = 254 nm. The multifunctional terpolymers can be spin-casted to form thin films of well-defined thickness, photo-crosslinked by a long UV wavelength light (λ = 365 nm) to form distinct structural patterns, and subsequently photo-chemically modified by a short UV wavelength light (λ = 254 nm). The photocleavage reaction by UV irradiation allows the production of free carboxylic groups that can be used to conjugate cationic markers, proteins, or nanoparticles to the terpolymer coating. Furthermore, the free carboxyl groups can be used to locally tune the swelling characteristics and transition temperature of the coatings.

For the second technology, when Fe_3O_4 magnetic nanoparticles are integrated into PNIPAAm based composite systems, their resultant hyperthermia behavior becomes an ideal mechanism for remote controlled actuation. In this work, nano Fe_3O_4 octopods were seeded in fabricated PNIPAAm hydrogel micro-actuators. When the magnetic hydrogel structures were exposed to a magnetic field strength of 63 kA/m at a frequency of 300 kHz, the hydrogel micro-beams underwent a buckling effect when the field was absent and an unbuckling effect when the field was present. The hydrogel micro-beams were fabricated at an approximate distance from one another developing micromanipulating surfaces that were remote control activated. The response time, heating efficiency, and magnetic behavior were thoroughly studied. Lastly, micron sized polystyrene beads were exposed to the antifouling surfaces and movement of the beads was observed as the magnetic hydrogel micro-beams underwent their physical changes.

For the third technology, a major reason of device failure in multi-chip module assemblies is a CTE mismatch between the underfill encapsulant material and the integrated circuit chip. Some of the failure mechanisms of microelectronic packaging due to CTE mismatch include fractures, delamination, or cracks through the device. In this section, the CTE of a commercially available underfill material is greatly reduced by loading the polymer resin material with hollow glass beads, to realize an overall effective CTE of 6.6 ppm/°C. Furthermore, the newly developed composite material exhibited outstanding thermomechanical stability at high temperatures beyond 150°C by holding a 3X lower CTE and a higher glass transition temperature.

CHAPTER 1: BACKGROUND AND MOTIVATION

1.1 Lab-on-a-Chip

Miniaturization of devices has attracted tremendous attention from academia and industry. Ever since physicist Richard Feynman's lecture "There's Plenty of Room at the Bottom" at the American Physical Society in 1959 [1], there has been an ever-growing interest in the miniaturization of electric devices. The machining of mechanical microdevices was first introduced during the 1970s [2], which was later known as microelectromechanical systems (MEMS). The development of microfluidics was first observed in the late 1980's after Manz et al. introduced microfluidics to the life sciences and chemistry [3]. Lab-on-a-chip (LOC) technology is composed of MEMS, microfluidics, and microbiology.

LOC devices involve the flow of small volumes of liquids (10^{-9} – 10^{18} liters) such as solvents and reagents through channels in the micron-scale size. LOC devices can be used in a wide range of applications, such as biochemical assays [4], chemical applications [5, 6], and biological applications [7, 8]. However, the foremost application of LOC devices is biological analysis [9-11]. LOC devices offer many unique advantages, including low operating and maintenance costs, affordability of mass production and replacement costs, short analysis time, high-resolution detection, the ability to require very small amounts of solvents, samples, or reagents, great portability and point-of-care testing. Particularly, the ability to provide portable point-of-care testing is one of the major promises of LOC devices.

Elastomers such as polyurethane and polydimethylsiloxane (PDMS) have been widely used in microfluidic applications. PDMS has proven to be an outstanding biocompatible material [12]. Furthermore, PDMS is a popular structural material for microfluidics due to straightforward processing and micromachining techniques [13-15]. PDMS plays an integral role in the development of microfluidic channels, along with functional components such as pumps [16, 17], valves [18-20], and mixers [19, 21-24].

1.2 Stimuli Responsive Polymers

Stimuli responsive polymers, also known as smart polymers or materials, are polymers that undergo abrupt physical-chemical changes in response to changes in their environment. Some of the stimuli that allow these changes to take place are changes in temperature [25], light [26], ionic strength [27], pH [28], electric field [29], and magnetic field [30]. Several polymers may respond to a combination of two or more stimuli. The recent advancement in the field of stimuli responsive polymers has generated great opportunities for the development of innovative biomedical applications. Some of the biotechnology and biomedical applications that have emerged thanks to the risen use of stimuli responsive polymers are tissue engineering [31], bio-separation [32], cell culture [33], bio-sensors [34], bio-actuation [35], and drug delivery [36]. The effects of external stimuli on polymers have been investigated as early as the 1960s by Heskins and Guillet [37].

1.2.1 Poly(N-isopropylacrylamide)

Poly(N-isopropylacrylamide) (PNIPAAm) is a soluble polymer under 32˚C and it precipitates in water when above 32˚C [25, 38, 39]. An important aspect of responsive polymers is controlling the lower critical solution temperature (LCST), which is the phase transition temperature. When working below LCST, the hydrogen bond interactions between amide

groups in water and polymer molecules allows the dissolution of polymer chains. On the contrary, the hydrogen bonds are broken when heated above the LCST, which in turn forces out water molecules from the polymer to cause its precipitation [40]. This response is reversible by controlling the system temperature, which makes it ideal for fabricating valves or actuators for applications in fluidic environments. Figure 1.1 shows a PNIPAAm hydrogel undergoing physical-chemical transition after reaching the LCST. NIPAAm has been employed as a strategic monomer in copolymers [41] and terpolymers [42] for multi-stimuli applications.

An interesting area of research is metal-seeded PNIPAAm copolymers. This is when metal is integrated into a gel with the use of co-polymerizable metal ligands, followed by metal complex formation. PNIPAAm gels that are seeded with magnetic materials have demonstrated susceptibility to AC magnetic fields, which in turn contributes to the swelling and de-swelling properties in the responsive polymer [43]. When the responsive polymer is triggered by the external stimulus, it displays an abrupt change in its physical-chemical properties. Change in the internal temperature of the thermally responsive polymer will induce a physical volumetric change. Particularly, an externally applied AC magnetic field can excite the embedded magnetic particles to heat up, and the resultant temperature increase above the LCST will cause the thermally-responsive polymer to collapse from its swollen state. Once the magnetic field is removed, the responsive polymer will return to its normal swollen state. The newly developed magneto-thermal responsive polymers offer unprecedented opportunities for implementation of implantable sensors and actuators under the control of the external AC magnetic fields, thus enabling novel in-vivo device applications such as the remotely controlled drug release [44].

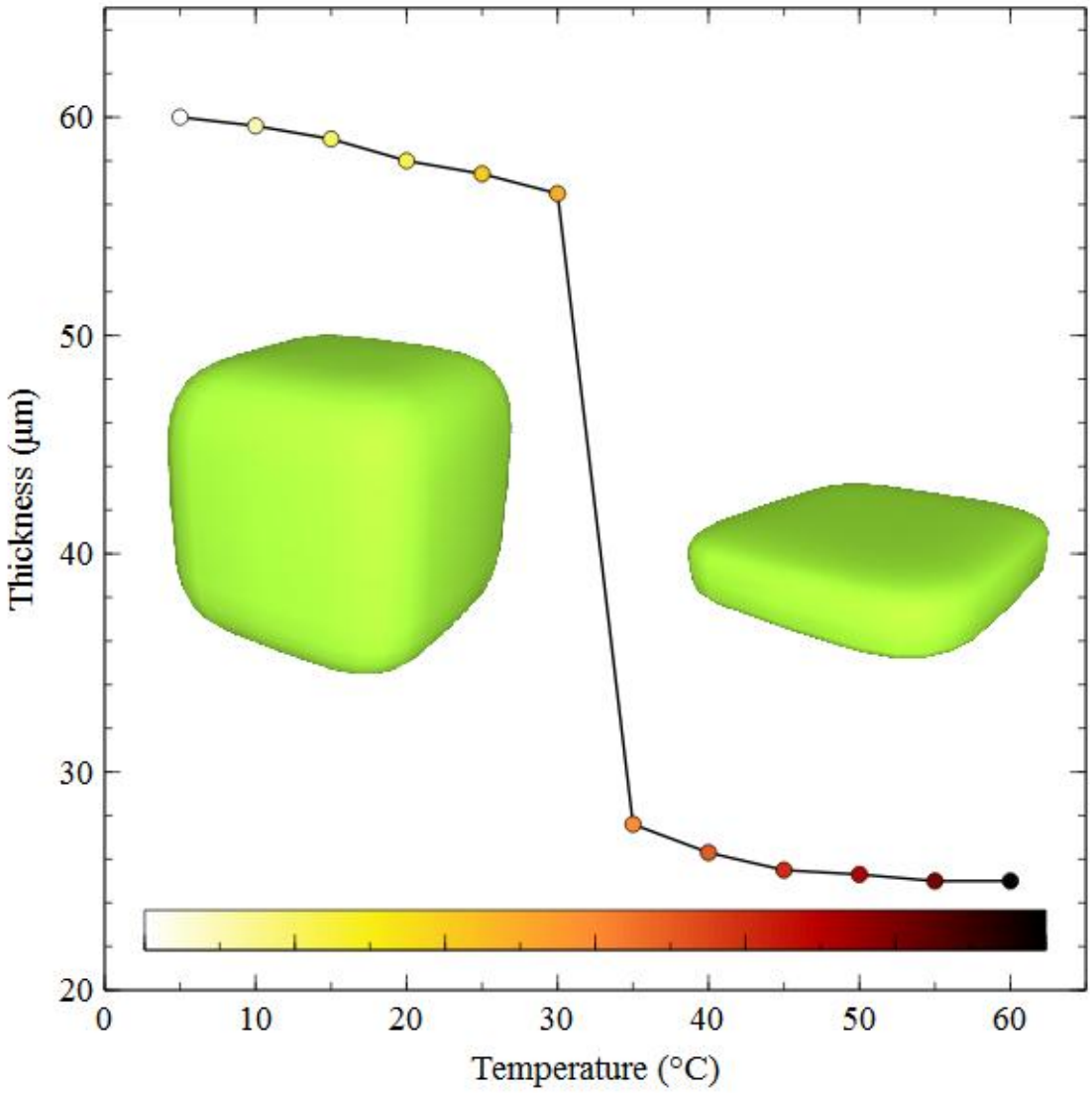

Figure 1.1: Conceptual illustration of the PNIPAAm hydrogel deswelling phenomenon after reaching the LCST.

1.2.2 Sol-Gel Reversible Hydrogels

The aqueous solutions of certain polymers go through a sol to gel transition as a response to a change in temperature. Proteins, cells, and drugs may be mixed in a sol state, and with a syringe it may be injected into the subcutaneous layers. In situ gelling injection systems generate great benefits to surgical procedures. The transition of sol to gel makes poloxamers an appealing solution to drug delivery applications, especially when dealing with in situ gel forming devices

[45]. On the other hand, due to the weak cross linking between micelles the poloxamer gel integrity does not last more than a few hours. This is crucial when working with drug delivery systems, since the long term delivery is often time desired. An injectable depot system was designed to increase gel durability along with improving biocompatibility [46]. For instance, Poly(ethylene glycol-b-(DL-lactic acid-*co*-glycolic acid)-b-ethyrlne glycol) or PEG-PLGA-PEG is a triblock copolymers aqueous solution that flows freely at room temperature, but develops into a gel at body temperature [47]. The sol to gel transition of these triblock copolymers can be controlled between 15˚C to 45˚C by changing its molecular parameters. Hydrophobicity plays a significant role, since the more hydrophobic a polymer is the stronger the shear stress that is needed to force the gel flow. As a result, the high transition temperature can be manipulated between 45˚C and 60˚C. At the high transition temperatures, the gel to sol transition is noticed to change into a 3D micellar structure. In rats, the integrity of the gel continued for more than a month. This demonstrates that the use of PEG-PLGA-PEG triblock copolymers is a promising tool for long term injectable drug delivery systems. Chitosan-glycerol phosphate water systems display similar inverting thermo-gelling properties [48]. At room temperature it is observed to be a sol, while at body temperature it is observed to be a gel. This system is currently under investigation for applications such as tissue engineering, protein delivery, and gene delivery.

1.2.3 pH Sensitive Polymers

Polymers that have an ionizable functional group that reacts to a change in pH are known as pH sensitive polymers. Some of the most common pH responsive polymers are poly(L-lysine), poly(N.N-dimethyl aminoethyl methacrylamide), poly(ethylene imine), polyacrylic acid, and polymethacrylic acid (PMAA) [49-51]. In recent times, there has been an increasing interest in pH-sensitive polymers for applications such as gene delivery and gene therapy research. Due

to the negative charges and the large size of DNA molecules, the transportation of naked DNA into a cell is a challenging task. As a result, positively charged polymers are utilized to balance the charge, while reducing the DNA size to nanoparticles of about 100 nm [52]. The down side is that the pH sensitive polymers are non-biodegradable. However, hydroxy proline and poly(L-lysine) ester analog polymers were synthesized, where hydroxy proline has exhibited bio-degradability within one day during in-vitro experiments. Other examples of pH-sensitive polymers that are currently being applied to gene delivery are poly(propyl acrylic acid) (PPA) and poly(ethacrylic acid) (PEA). Both of these polymers display an abrupt conformational transformation at a pH value of about 5 and 6 [53]. Poly(N-acryloyl-N-propylpiperazine) (PNANP) is known for being a dual stimuli responsive polymer, and aqueous solutions of PNANP experience a LCST at 37˚C, and its transition temperature fluctuates from 65˚C at a pH of 6 to 25˚C at a pH of 10 [54]. When taking into account that there is a minor pH difference among normal cells, pH-sensitive polymers are extremely useful and important in identifying pharmaceutical agents in cancer cells.

1.2.4 Hybrid Hydrogels

Peptides experience conformational transformations that may be triggered by pH, temperature, and specific binding behavior. Pairing these peptides with a synthetic polymer or other polypeptides generates stimuli sensitive hybrid systems. ProLastin is a polypeptide block copolymer that is made out of elastin like (GVGVP soft segment) -silk-like (GAGAGS hard segment) polypeptides. ProLastin experiences sol to gel transformations at 37˚C. The transformation is triggered by the crystallization of hard blocks that are produced by hydrogen bonding of amino acids [55]. Hybrid hydrogels made out of synthetic polymer and protein

folding structures were also developed. These hydrogels break down at about 40˚C, which can be ascribed to the supportive conformational transition of the coiled protein domain [56].

1.2.5 Light-Sensitive Polymers

There has been increasing attention towards light-sensitive polymers in the last decade. Light is a versatile stimuli due to its ability to target a localized area for a controlled period of time. Additionally, selectivity can be assured by tuning the irradiation parameters, such as wavelength and intensity according to the photosensitive moieties used [57]. There have been several reports of photosensitive moieties including azobenzene [58-62], coumarin [63, 64], *o*-nitrobenzyl [65, 66], pyrene [67], and spiropyran [62, 68]. Along similar lines, light-sensitivity can be combined with other types of stimuli to develop multi-functional polymers.

1.3 Magnetic Nanoparticle Hyperthermia

Magnetic nanoparticles that are exposed to an AC magnetic field have demonstrated their ability to generate heat effectively. This technique was first introduced by Gilchrist in 1957 [69] where maghemite nanoparticles were used to heat lymph nodes in dogs and later progress was shown on a variant on humans [70, 71]. This hyperthermia work is based on the observations that tumor cells could be destroyed by heating the cells at temperatures between 43°C and 46°C while healthy cells were less affected [72, 73]. Iron oxide (Fe_3O_4) magnetic nanoparticles have been demonstrated to have excellent biocompatibility, monodispersity, and magnetic resonance. Therefore, they are the most popular magnetic nanoparticles for biomedical applications, which include cellular imaging [74], separation of biochemical products [75], sorting and labeling of cells [76], targeted drug delivery [77, 78], magnetic resonance imaging [79, 80], magnetic fluids [81, 82], .and tissue specific releasing of therapeutic agents [83].

1.3.1 Magnetic Nanoparticle Heating Mechanisms

Depending on the magnetic material, heat can be generated by Joule heating heat due to eddy currents, magnetic heating due to Neel and Brownian relaxations, and magnetic heating due to hysteresis losses [84].

1.3.1.1 Eddy Currents

The Faraday-Lenz law of electromagnetic induction states that when an AC field penetrates a conducting sample, the associated time-varying magnetic flux will induce the evolution of eddy currents opposing the applied field. This generates a field attenuation that depends on the field frequency, material electrical conductivity and its permeability. Eddy currents also occur in tissue. However, its low specific electrical conductivity of 0.6 Ωm^{-1} is approximately eight orders of magnitude smaller than found in metals [85]. For that reason, this heating mechanism is not practical for therapeutic dosage.

1.3.1.2 Neel and Brownian Relaxations

A single super spin is a set of individual magnetic moments inside a magnetic particle, and it accounts for the total magnetization per particle. Small ferromagnetic or ferrimagnetic nanoparticles in the range of a few nanometers to a couple of tens of nanometers thermally activate a process called superparamagnetism, where thermal fluctuations overcome the magnetic energy, thus causing a fast flipping of the magnetization away from its equilibrium state.

Rotation of magnetic nanoparticles suspended in liquid is governed by two relaxation mechanisms. The first is Neel relaxation, which involves an orientation change of all the spins in the particle, in turn, changing the magnetization direction. However, there is no physical rotation of the particle as illustrated in Figure 1.2. Louis Neel proposed that the magnetization of the

nanoparticles is temperature dependent and that there is a characterization time, relaxation time τ_N [86] as defined by the following:

$$\tau_N = \tau_0 e^{(\frac{E_B}{k_B T})} \tag{1.1}$$

where, k_B is the Bolzmann constant and E_B is the anisotropy energy barrier, and τ_o is the attempt time, which presumed to be constant with a value range between 10^{-9} – 10^{-13} seconds.

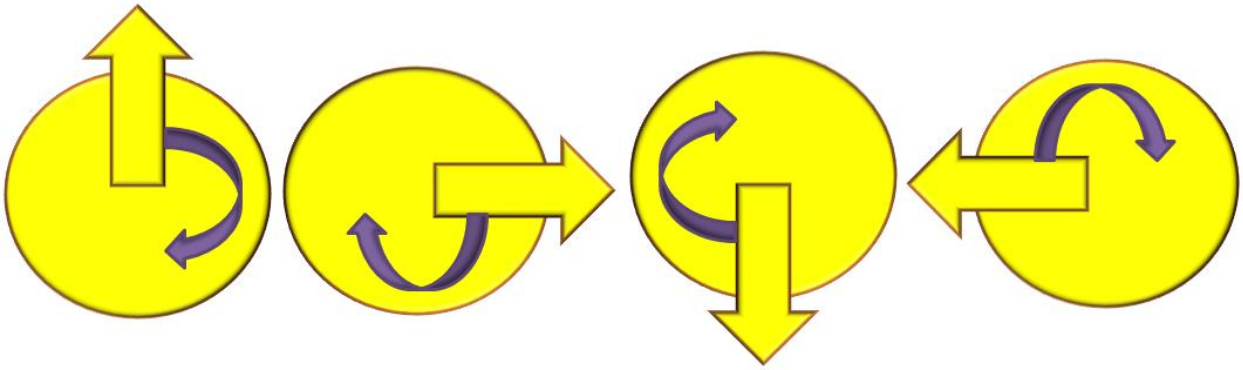

Figure 1.2: Neel relaxation diagram showing the rotation of the nanoparticle magnetic moment

A shown in Figure 1.3, the second relaxation mechanism is called Brownian relaxation. Here the nanoparticle physically rotates dependent on the hydrodynamic parameters of the nanoparticles and the medium at a characteristic time as defined by the following [87]:

$$\tau_B = \frac{3V_h\eta}{k_B T} \tag{1.2}$$

where, V_h is the hydrodynamic volume and η is the viscosity of the liquid.

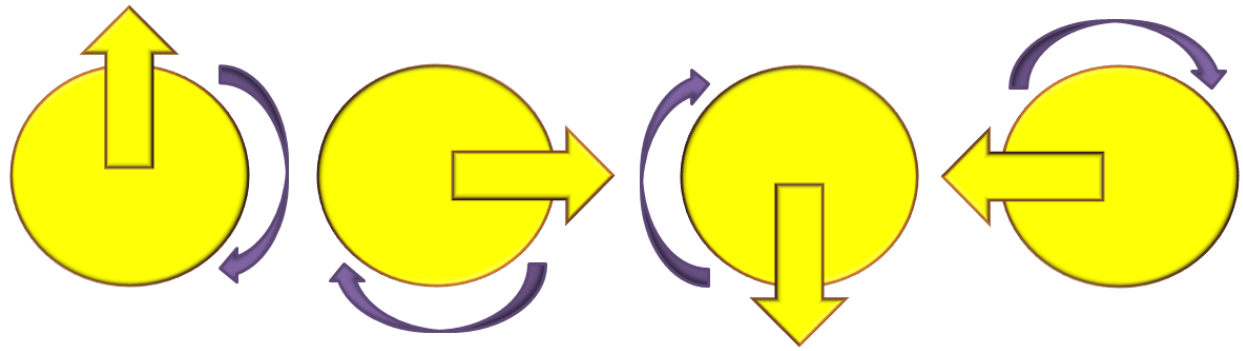

Figure 1.3: Brownian relaxation diagram showing the rotation of the nanoparticle

At a short range of particle sizes, Neel relaxation dominates as the fastest process. However, above a specific critical size, Brownian relaxation dominates. Furthermore, heat dissipated through Neel relaxations does not depend on the local environment, which is the reason why this heating method is preferred in clinical trials [88].

1.3.1.3 Hysteresis Losses

The magnetic structure of ferromagnetic materials is spontaneously split into domains, or groups of magnetic moment regions with the same orientation. Moreover, when the ferromagnetic materials are exposed to an AC magnetic field, they exhibit a non-linear behavior demonstrated by the hysteresis loop shown in Figure 1.4. Here, M_s is point of magnetic saturation of the material and it is reached when all of the material magnetic moments are aligned with the field. M_r is the remanence or remanent magnetization, and it is the point where the magnetic field (H) is reduced to zero from the saturation state. Some of the magnetic domains lose their alignment but some maintain to be aligned. This means that some magnetic flux density is still retained in the material. H_c is coercivity or coercive field, which is the magnetic field intensity required to demagnetize a saturated ferromagnetic material. Here the majority of the domains are oriented randomly and the magnetic flux density is equal to zero. As the field (H) is increased to the negative direction, magnetization (M) reaches saturation in the opposite direction. Here all of the domains are aligned in the opposite direction of the positive saturation. The area under the hysteresis loop is related to the amount of heat being generated per cycle P_{FM} [89] and it is defined by the following:

$$P_{FM} = \mu_0 f \oint H \, dM \tag{1.3}$$

where, f is the frequency of the magnetic field, H is the magnetic field strength, and M is the magnetization.

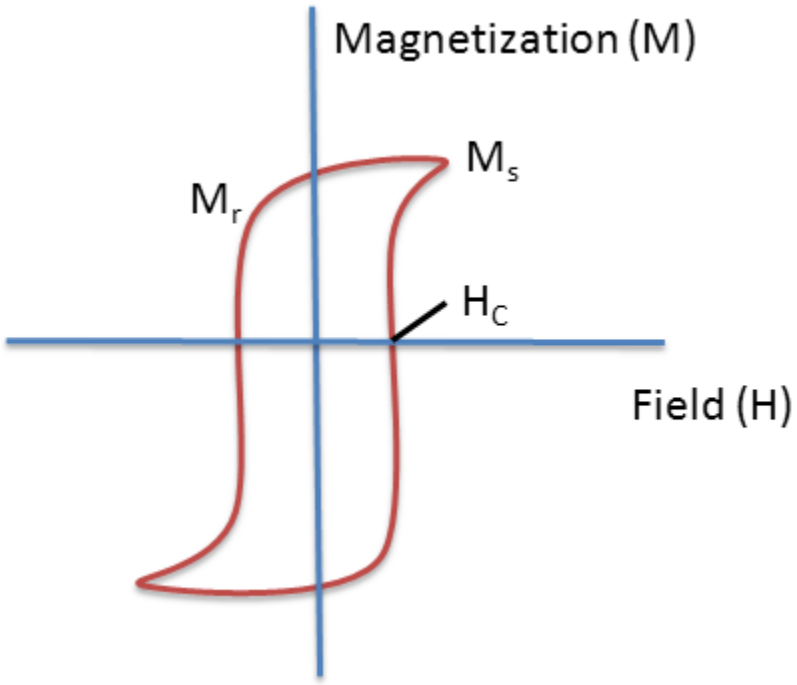

Figure 1.4: Conceptual illustration of a typical M-H hysteresis loop diagram

1.3.2 Specific Absorption Rate (SAR)

The specific absorption rate (SAR) quantifies the nanoparticle heating efficiency and it is the amount of energy absorbed during the exposure of electromagnetic radiation [90] and it is defined by the following:

$$SAR = (\Delta T \cdot c) \cdot t^{-1} \tag{1.4}$$

where, ΔT is the temperature increment, c is the material specific heat, and t is the time of the sampling period. Specific loss power (SLP) is an equivalent term frequently found in literature.

1.3.3 Magnetic Nanoparticle Shape

Not much research has been performed on the effect of the shape on the magnetic properties of nanoparticles of equivalent size. On the other hand, there have been many studies on the synthesis of different shaped magnetic nanoparticles, such as maghemite nanorods [91],

andmagnetite tetrapods [92], Au-MnO nanoflowers [93], ferrite nanocubes [94], cobalt nanodiscs [95], and magnetite nanooctopods [96].

Figure 1.5 shows a nanosphere and nanocube with a magnetic field traveling in the same direction. At this point the magnetic moments are aligned in the same direction for both particles. When the magnetic field is switched to the opposite direction, it is easier for the magnetic moments at the edge of the nanosphere to re-align, since they are already angled. On the other hand, the nanocube has flat surfaces, which means that it will require more work for the magnetic moments to adjust its alignment. This work difference for alignment adjustment results in an increase in coercivity, which is reflected on their respective M-H hysteresis loops. Therefore, more heat is anticipated to be generated by the nanocubes.

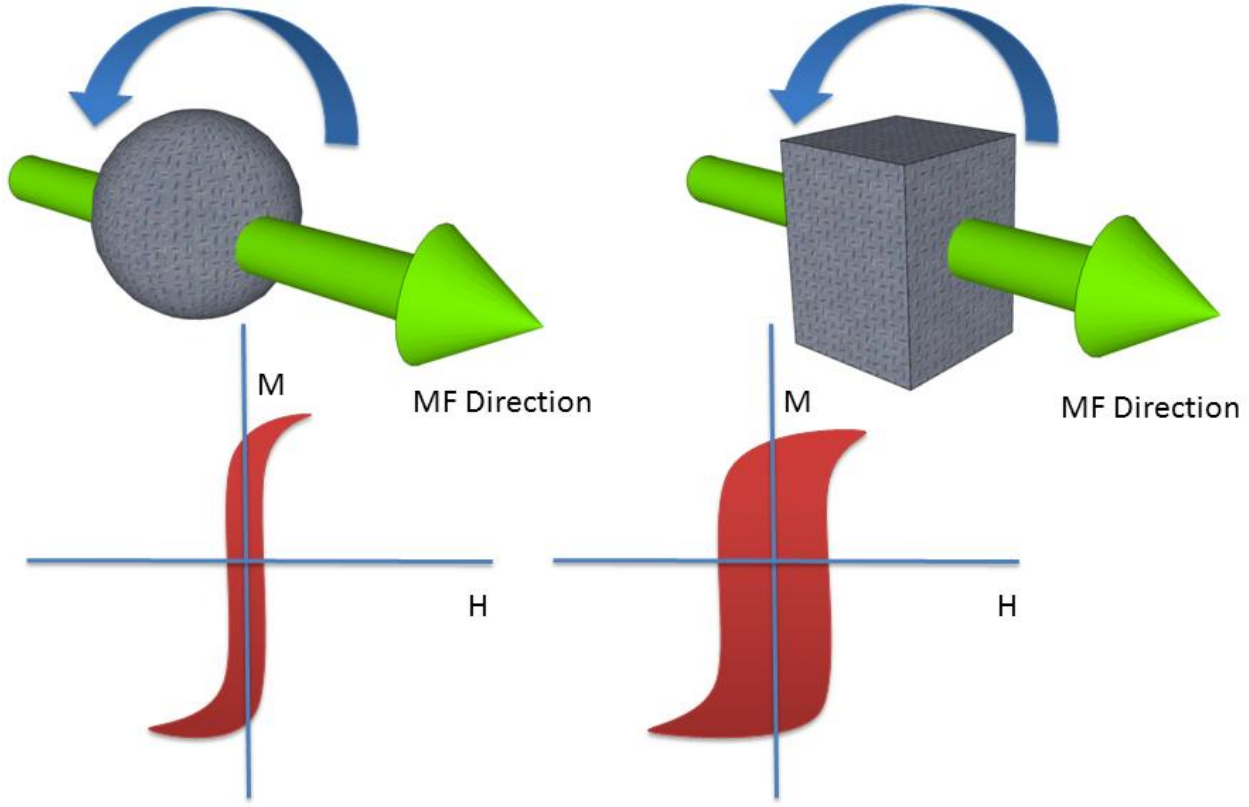

Figure 1.5: Conceptual diagram showing the heat generation by nanosphere vs. nanocube

CHAPTER 2: MATERIALS AND METHODS

2.1 Characterization Techniques

2.1.1 Ellipsometry

Ellipsometry is a non-perturbing optical measurement technique that accurately detects changes in the polarization state of light after reflection from the sample surface. Ellipsometry samples can be examined without any prior preparation or special environment.

In the 1660s Robert Hooke published wave theory of light. Shortly after, Christian Huygens presented his own wave theory of light and published Treatise on light in 1690 [97]. Huygens proposed that light was emitted as a series of waves from a point source. Using his experiments with slits, Thomas Young confirmed that light is based on waves. Interference is a fundamental concept in wave theory and it is crucial to the understanding of light reflection from surfaces. In 1823 Augustin-Jean Fresnel showed that if light was transverse in wave nature instead of longitudinal, the polarization of light was possible. In 1873 James Clerk Maxwell developed the electromagnetic field theory. In 1902 Paul Drude published "The Theory of Optics" [98], where without using the word ellipsometry, he was able to illustrate all the necessary optical components needed to perform ellipsometry. Drude is known as the father of ellipsometry. In the late 1920s Leif Tronstad performed research on thin films and in 1930 he published a manuscript entitled "The investigation of thin surface films on metals by means of the reflected polarized light"[99]. However, it was not until 1945 that the term "ellipsometry" was used for the technique in a paper by Alexandre Rothen [100]. Peculiarly, ellipsometry

principles have been established for more than 100, but the instrument has not been considered productive until lately. The 1960s saw a boom in the computer technology, requiring the use of automated ellipsometry systems for the area of semiconductors. The commercialization of ellipsometry systems has now expanded to research universities and industry.

2.1.1.1 Fundamental Parameters

Ellipsometry measures change in light polarization, where ψ (PSI) determines the differential changes in amplitude and Δ (DELTA) determines the differential changes in phase during reflection. The Fresnel reflection coefficients r_p and r_s cannot be measured separately,. However, ellipsometer methods can be applied to measure their ratio p, which is defined by the following:

$$p = \frac{r_p}{r_s} \tag{2.1}$$

Given:

$$r_v = \frac{R_v}{E_v} e^{i(\beta_v - \alpha_v)} \qquad v = p \text{ or } s \tag{2.2}$$

Substituting from equation (2.2) gives:

$$p = \frac{\frac{R_p}{E_p} e^{i(\beta_p - \alpha_p)}}{\frac{R_s}{E_s} e^{i(\beta_s - \alpha_s)}} \tag{2.3}$$

which can be arranged to give:

$$p = \frac{\frac{R_p}{R_s}}{\frac{E_p}{E_s}} e^{i(\Delta_r - \Delta_i)} \tag{2.4}$$

where, $\Delta_i = \alpha_p - \alpha_s$ and $\Delta_r = \beta_p - \beta_s$. Δ_i (Δ_r) represents the phase difference between the p and s components of the reflected electric field. Equation (2.4) can be further simplified to:

$$p = \tan\psi \, e^{i\Delta} \tag{2.5}$$

where, $\tan\psi = \frac{\frac{R_p}{R_s}}{\frac{E_p}{E_s}}$ represents the amplitude ratio change upon reflection, and $\Delta = \Delta_r - \Delta_i$ represents the phase difference change between the *p* and *s* components caused by reflection. Equation (2.5) is known as the basic equation of ellipsometry.

Keep in mind that ψ and Δ are angles. Angle ψ may have any value between 0° and 90° and angle Δ may have any value between 0° and 360°. Therefore, reflection may be characterized by ellipsometry using angles ψ and Δ.

2.1.1.2 Obtainable Parameters

Some of the optical constants that can be obtained with an ellipsometer are the refractive index (n) and the extinction coefficient (k) of a sample surface. The refractive index (n) is the propagation speed of the wave through the sample and the direction of propagation. The extinction coefficient (k) determines how much wave energy is absorbed by the material.

From the known refractive index of a material the layer thickness can be accurately measured, including very thin angstrom-scale film samples. This process is very popular in the semiconductor industry.

The majority of commercial ellipsometers are variable angle instruments. Measurements are taken at a range of angles, usually between 40° and 90°. This is done to study the samples near or at the Brewster angle, for optimum sensitivity.

Materials transmit or reflect light differently depending on the light wavelength. Therefore an ellipsometer may be coupled with a spectrometer to facilitate variable wavelength light to be used.

It is possible to measure the thickness of multiple layers. After measuring a range of angles and wavelengths and using known sample optical parameters, computer processing modeling can be used to determine sample thickness of up to 20 layers. Although an

ellipsometer is unable to provide the layer thickness directly, the obtained data is very accurate, allowing the fitting of the proposed model.

2.1.1.3 Ellipsometer Working Principle

The basic principle of ellipsometry is illustrated in Figure 2.1. A 632.8 nm He-Ne laser is the used light source and it emits un-polarized light. This light is linearly polarized by a polarizer at a fixed angle of 45°. The light then hits the sample at an identified angle ρ. The light penetrates the layer until it reaches the layer-substrate interface, where it is reflected. The light beam exits the layer at the same angle as the incidence angle ρ. The light beam then reaches the rotating analyzer, where reflectance measurement for all Δ phases takes place. Finally, a photodetector measures the light beam intensity as a function of the angle of the rotating analyzer.

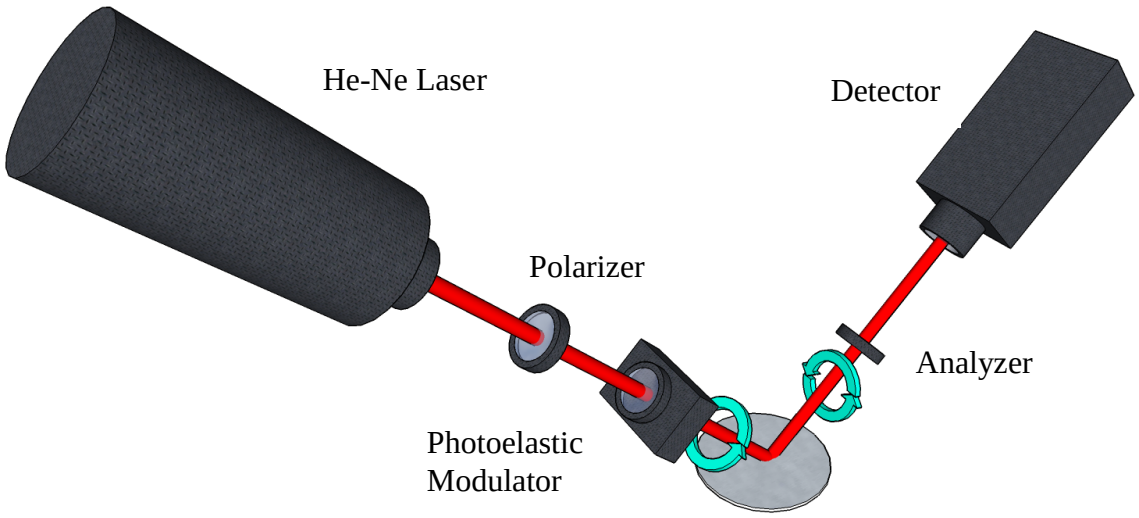

Figure 2.1: Ellipsometer schematic

2.1.2 Ultra Violet Visible Spectroscopy

Spectroscopy is science that studies the interaction of matter with light. Ultraviolet-visible spectroscopy (UV-Vis) is an instrumental technique of analysis that determines the micro

or semi-micro quantities of analytes in a sample. The UV-Vis spectrum is a result from the interaction of electromagnetic radiation with molecules, ions, or complexes in the UV-Vis region. This is the basis of analysis of different organic, inorganic, and biochemical substances.

The idea of UV-Vis originated in 1666 when Sir Isaac Newton's curiosity sparked an interest in the origin of colors. Newton performed an experiment where he allowed sunlight to enter a window shutter and passed it through a glass prism. He noticed that the white light from the sun was divided into a spectrum of colors that were projected onto a screen. He then passed the individual colors through a prism in reverse position and witnessed the white light being restored. Newton concluded that white light was in fact created by different colors that was bent as it passed through the prism [101]. This was the birth of spectroscopy. In 1859 Gustav Kirchhoff proposed the theory of absorption and emission, which tried to explain the Fraunhofer lines in the sun's continuous spectrum [102]. Kirchhoff's theory specified that any good light emitting substance of a certain wavelength would also absorb light at the same wavelength. His conclusion was that the dark lines in the solar spectrum were generated by cooler outer layer of gases in the sun's atmosphere absorbing from the continuous spectrum. This was a big breakthrough for Kirchhoff, since his findings coupled with the fact that each atom and molecule produced a characteristic and unique line spectrum would generate great potential in visible spectroscopy for chemical analysis.

The commercialization of UV-Vis spectrophotometers took place in the early 1940s, after vitamin research revealed that several vitamins absorbed UV light in the 1930s. This originated as an American government interest to measure the vitamin content in soldier's rations using UV and UV-Vis light. In 1941, the Beckman DU spectrophotometer, an instrument created by Arnold O. Beckman at the National Technical Laboratories Company, was the first commercial

UV-Vis spectrophotometer to be developed and sold [103]. UV-Vis spectrophotometers are vital for measuring analyte concentrations. As a matter of fact, Nobel laureate Bruce Merrifield referred to the UV-Vis spectrophotometer as "probably the most important instrument ever developed toward the advancement of bioscience" [103].

2.1.2.1 Spectrophotometry and the Spectrophotometer

Every chemical compound absorbs, transmits, or reflects light over a certain range of wavelengths. Spectrophotometry is a measurement of the amount of absorbance or transmittance in a chemical substance. A spectrophotometer is the instrument that measures the intensity of absorbed light after it passes through the sample solution. Substance concentrations can be determined by the detected light intensity.

The spectrophotometer can be categorized by two types, depending on the light source wavelength range. It can be categorized as a UV-Vis spectrophotometer, which operates between 185 – 400 nm (UV range) and between 400 – 700 nm (visible range) of the electromagnetic radiation spectrum, or it can be categorized as an IR spectrophotometer, which operates between 700 – 15000 nm (IR range) of the electromagnetic radiation spectrum.

The basic structure of a conventional single-beam spectrophotometer is shown in Figure 2.2. The light source directs polychromatic light towards the entrance slit, which transmits a narrow light band. This is the entrance of the monochromator. The narrow light beam is passed through a dispersion device (prism), which splits the light into a component of different wavelengths. The exit slit passes a narrow band of wavelengths, which pass through the sample. The sample absorbs and the light that makes it through the other side of the sample is received by the detector for absorbance analysis. When working with a single-beam spectrophotometer, it is required to first zero the instrument before measuring the sample.

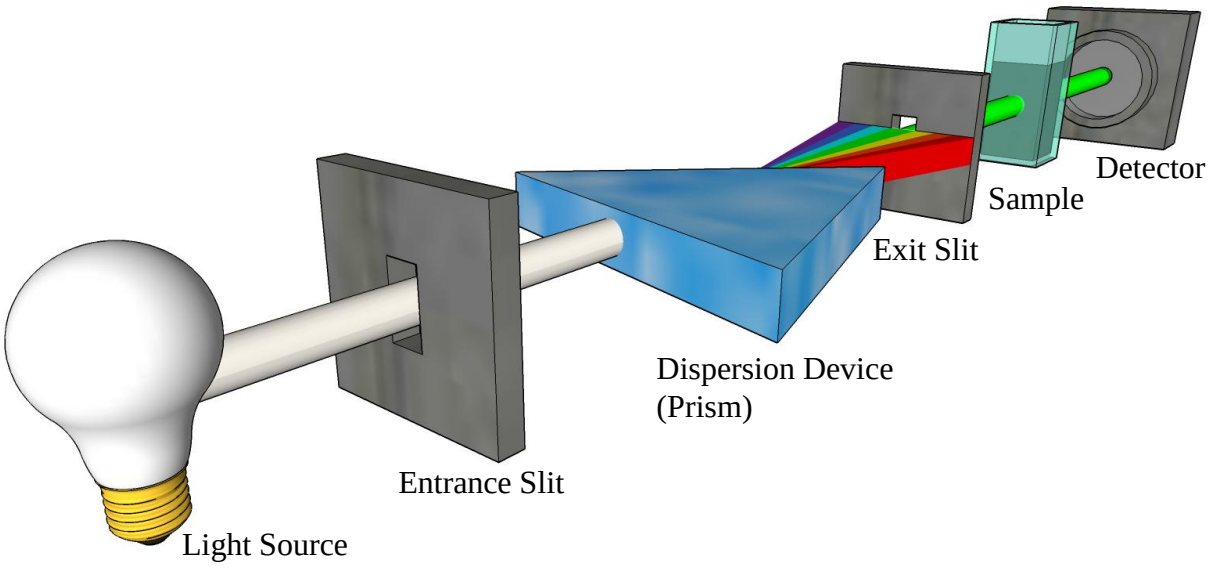

Figure 2.2: Structure of conventional single beam spectrophotometer

2.1.2.2 The Electromagnetic Spectrum

The electromagnetic spectrum is the distribution of electromagnetic radiation corresponding to energy. From looking at Figure 2.3, it is clear to see that the UV and visible radiation consist of a very small part of the electromagnetic spectrum. The electromagnetic spectrum ranges from very short wavelength (Gamma rays) to very long wavelengths (AM radio waves).

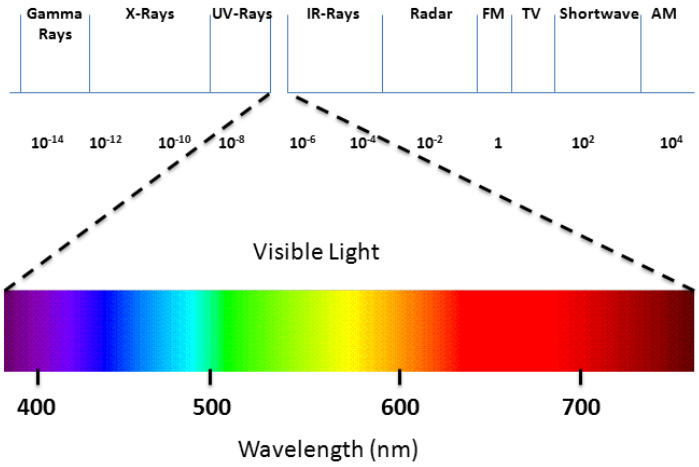

Figure 2.3: The electromagnetic spectrum

2.1.2.3 Quantum Theory

For this section it important to visualize radiation as stream of photons instead of waves. Molecules and atoms dwell in different defined levels or energy states and level changes require absorption or emission of a quantum, or photon. The photon energy absorbed or emitted during a molecular energy level transition is defined by the following:

$$E = h\nu \tag{2.6}$$

where, E is the energy in joules, h is the Planck's constant of 6.62 x 10^{-34} Js, and ν is the frequency in seconds. Due to the fact that radiation behaves as a wave, it can be categorized in terms of wavelength or frequency. These are correlated in the following:

$$\nu = \frac{c}{\lambda} \tag{2.7}$$

where, ν is frequency in seconds, c is the speed of light 3 x 10^{8} ms^{-1}, and λ is the wavelength in nanometers. It can be seen from equations 2.6 and 2.7 that UV light with low wavelength has the highest amount of energy. The energy of visible light is about 170 kJ mol^{-1} (photon mole) for red light and 300 kJ mol^{-1} for blue light. The elevation of electrons to different energy levels occurs in the visible and the UV region of the electromagnetic radiation. Table 2.1 demonstrates the electron transitions between 190 and 900 nm.

Table 2.1: Frequency, wavelength, and energy radiation used for UV-Vis spectroscopy

Spectrum Range	Frequency ν (Hz)	Wavelength λ (nm)	Energy (kJ mol^{-1})
Infrared	3.33 x 10^{14}	900	137.5
Red Light	4.29 x 10^{14}	700	171.2
Blue Light	7.50 x 10^{14}	400	299.3
Ultraviolet	1.58 x 10^{14}	180	630.5

Since light is a form of energy, light absorption by matter generates the energy content of the molecules or atoms to increase. The overall energy of a molecule corresponds to the sum of electronic, vibrational, and rotational energies.

$$E_{Total} = E_{Electronic} + E_{Vibrational} + E_{Rotational} \quad (2.8)$$

In certain molecules and atoms, UV and visible light photons contain enough energy to trigger transitions between different electronic energy levels. The absorbed light wavelength may have enough energy for an electron to move from a lower energy level to a higher energy level. These energy level transitions generate narrow absorbance bands at specific wavelengths for the particular absorbing material. In simple molecules, the electronic energy levels are widely separated and only the absorption of a high energy photon has the ability to excite a molecule to another level. In complex molecules, the energy levels are closely spaced and photons in the near UV and visible light can cause the transition. Consequently, these complex molecules will absorb light in the near UV and visible regions. Molecular vibrational energy states are much closer together than the electronic energy levels, so lower energy protons can generate vibrational changes. Light absorption caused by vibrational changes takes place in the infrared region. Molecular rotational energy states are so close together that light in the far IR and microwave regions have enough energy to generate changes.

Table 2.2: Energy types in each electromagnetic spectrum region

Region of Spectrum	**Energy Transitions**
X-rays	Bond Breaking
Ultraviolet/Visible	Electronic
Infrared	Vibrational
Microwave	Rotational
Radio Frequencies	Nuclear Spin (Nuclear Magnetic Resonance) Electron Spin (Electron Spin Resonance)

2.1.2.4 UV-Vis Absorption Spectra

The absorption of UV and visible light is due to the excitation of electrons from lower energy levels to higher energy levels. Because matter energy levels are quantized, only light

with the exact amount of energy can cause these energy level transitions, and in turn, be absorbed.

Valance electrons can be found in one of the following three types of electron orbital: Single σ bonding orbitals, double or triple bonds (π bonding orbitals), and non-bonding orbitals (lone pair electrons). Figure 2.4 shows possible electronic transitions that may be caused by light. Most of the transitions from binding orbitals have too high of a frequency to measure. Therefore, most absorptions only involve $\pi \rightarrow \pi^*$, $n \rightarrow \sigma^*$, and $n \rightarrow \pi^*$ transitions. Much more energy is required to excite electrons to a higher energy level when the energy level gaps are larger.

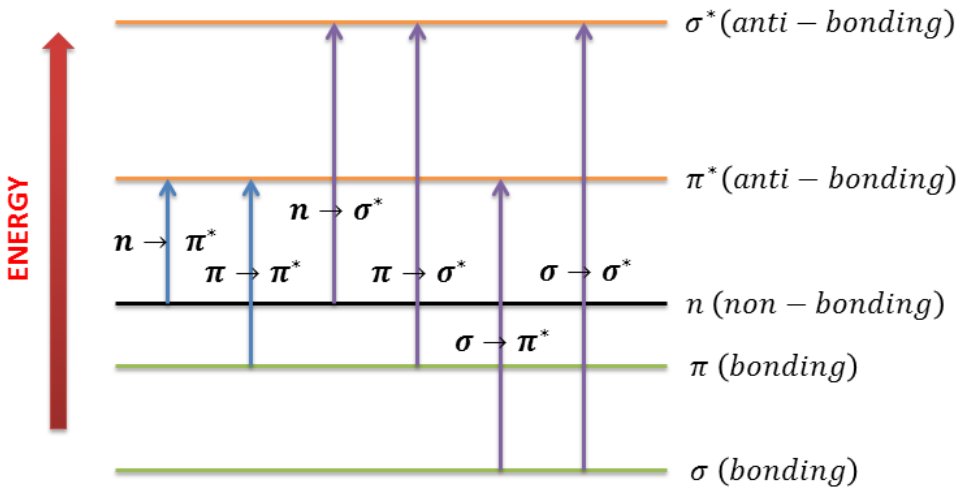

Figure 2.4: Possible electronic transitions

It is probable to predict the wavelengths that are most likely to be absorbed by a substance with color. When white light passes through or is reflected by a substance with color, a characteristic fraction of the mixed wavelength is absorbed. The light that remains undertakes the color of the absorbed wavelength. Table 2.3 demonstrates the relationship between light absorption and color.

Table 2.3: Light absorption and color relationship

Color Absorbed	Color Observed	Absorbed Radiation (nm)
Violet	Yellow – green	400 – 435
Blue	Yellow	435 – 480
Green – blue	Orange	480 – 490
Blue – green	Red	490 – 500
Green	Purple	500 – 560
Yellow – green	Violet	560 – 580
Yellow	Blue	580 – 595
Orange	Green – blue	595 – 605
Red	Blue – green	605 – 750

When light passes through or is reflected from a sample, the amount of absorbed light is the difference between the incident radiation I_0 and the transmitted radiation I. The amount of absorbed light is said to be absorbance or transmittance. Transmittance is typically expressed as a percentage or a fraction of 1.

$$\%T = \frac{I}{I_0} \times 100 \ \ or \ \ T = \frac{I}{I_0} \tag{2.9}$$

Absorbance is expressed as:

$$A = -logT \tag{2.10}$$

2.1.2.5 Beer-Lambert Law

The Beer-Lambert law is the most important principle in absorption. This law states that absorbance is proportional to the concentration of the substance in a solution [104]. Consequently, UV-Vis spectroscopy can also be used to measure the concentration of a sample. The Beer-Lambert law can be expressed as follows:

$$A = \varepsilon cl \tag{2.11}$$

where, A is the absorbance, ε is the molar extinction (constant for a specific substance at a specific wavelength) in $dm^3\ mol^{-1}\ cm^{-1}$, c is the concentration of the solution in mol dm^{-3}, and l is

the optical path length in cm. The concentration rate change of a sample can be verified by measuring the increase or decrease of absorbance of a colored solution.

2.1.3 Atomic Force Microscopy (AFM)

Atomic force microscopy (AFM) is a method used to study material surfaces by obtaining images with atomic resolutions of 10^{-1} m. This method can be applied to soft and hard synthetic materials, and biological structures.

The development of the AFM began in1892 when Binning, Rohrer, Gerber, and Wiebel developed the scanning tunneling microscope (STM) at IBM in Zurich, Switzerland [105]. Binning and Rohrer won the Nobel Prize in Physics for this invention of the STM in 1986. The STM was built upon the work of Russell Young's topografiner [106]. The STM had much higher resolution than the topografiner, since it monitored electron tunneling. Still, both methods had sample analysis limitations. In 1986, Binning, Quate, and Gerber, in collaboration between IBM and Stanford University, developed the AFM [107]. They were able to replace the electron tunneling from a fine wire of the STM with the AFM cantilever approach. In 1987, Wickramsinghe developed an AFM setup with a vibrating cantilever technique with an optical interferometer to measure cantilever vibration amplitude [108]. Commercial AFM instruments have been available since 1988 and have been a ground-braking contributor to research in the areas of material sciences [109], biological sciences [110], pharmaceutical sciences [111], and polymer sciences [112].

2.1.3.1 Principle of Operation

A probe is kept at close contact with the sample surface through a feedback mechanism while it scans the surface. When the sample-to-probe distance remains constant, it is known to be the sample topography. A scanner controls the movement of the probe over the sample

surface, which is usually made from piezoelectric materials so that it precisely moves the probe in the x, y, and z axes. The photodetector signal passes through the feedback circuit and into the z-movement component of the scanner. This is how the probe-to-sample distance is remained constant. The cantilever behaves as a spring. Therefore, the fixed cantilever deflection indicates that a probe-to-sample force is maintained. The sample topography is determined by the amount by which the scanner moves in the z axis in order to maintain the cantilever deflection. Figure 2.5 shows the AFM operation and Figure 2.6 shows a 2D and 3D image of a spin coated poly(N-isopropylacrylamide) based polymer on a silicon substrate.

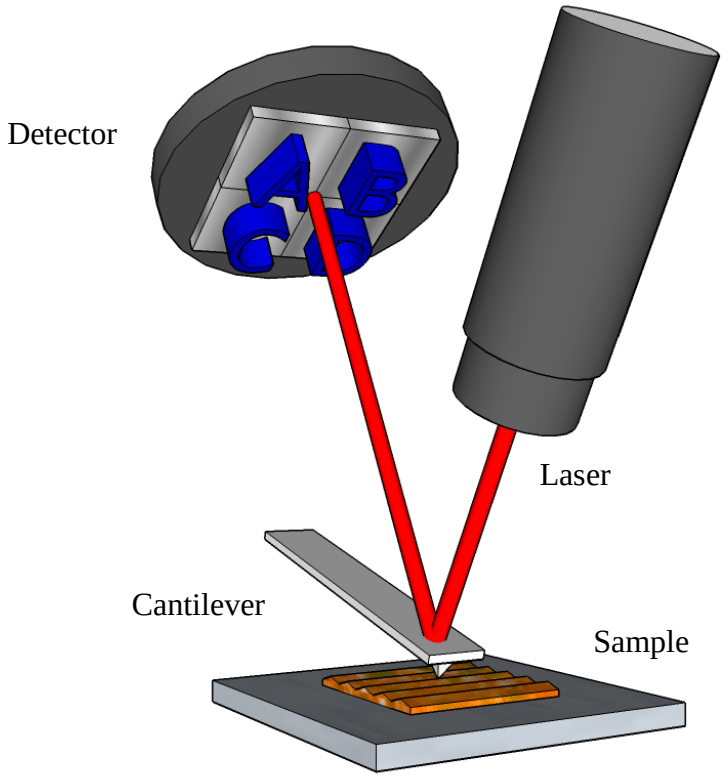

Figure 2.5: Principle of AFM operation

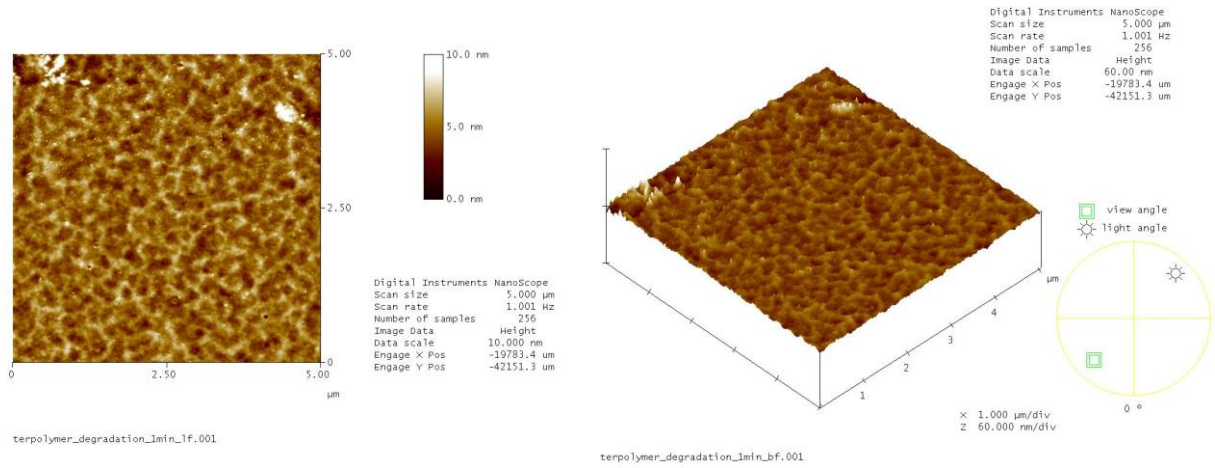

Figure 2.6: 2D and 3D images of a spin coated poly(N-isopropylacrylamide) based terpolymer on a silicon substrate

2.1.3.2 Principle of Probe Sample Atomic Interaction

The AFM consists of a micron-scale cantilever with a sharp nanometer-scale tip at the end. This tip is used to scan above the sample surface. When the tip is brought into proximity of the sample surface, Van der Waals forces between the tip and the sample cause a deflection of the cantilever. At very small tip-to-sample distances, usually a few angstroms, a very strong repulsive force is present between the tip and the sample atoms. This is due to the electronic orbitals at atomic distances. The tip and sample are in contact when the repulsive force is predominant. On the other hand, an attractive force (Van der Waals) is present when an instantaneous polarization of an atom induces a polarization in nearby atoms.

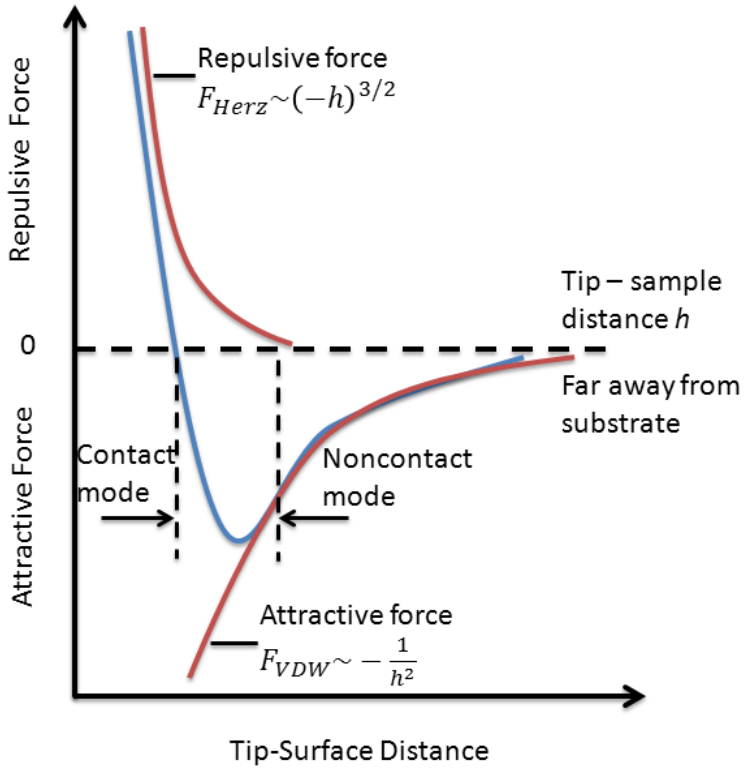

Figure 2.7: Atomic interaction

2.1.3.3 AFM Operation Modes

The most common modes of AFM operation modes are contact mode AFM (C-AFM or CMAFM), tapping mode AFM (TMAFM, IC-AFM, or AM-AFM), and noncontact mode AFM (NC-AFM, FM-AFM, or close contact AFM)

In contact mode AFM the probe is dragged across the sample surface [113]. As the sample topography changes, the z-scanner repositions itself in order to maintain constant deflection. The z-scanner motion is directly proportional to the sample topography. The force is calculated from Hooke's Law:

$$F = -kx \tag{2.12}$$

where, F is force, k is the spring constant, and x is the cantilever deflection. Force constants range from 0.01 N/m to 1.0 N/m, thus resulting in forces ranging from nN to μN in ambient temperature.

In non-contact mode AFM the cantilever is vibrated close to its resonance frequency around 100 kHz [114]. The tip is oscillated over the surface and the amplitude of the oscillation is kept constant. The tip-to-sample separation is between 1 nm to 10 nm.

Tapping mode AFM is a combination of contact and non-contact mode AFM. This mode is appropriate for imaging soft samples [115]. While the resolution is comparable to contact mode AFM, the applied forces are lower. Alike non-contact mode AFM, the cantilever oscillates close to its resonance frequency. However, the oscillation amplitude is 20-200 nm greater than non-contact mode AFM.

There are many non-topographic AFM modes to measure sample properties. Some of these samples are magnetic force microscopy MFM, which measures the magnetic field distribution on in the sample, and kelvin probe microscopy KPM, which measures the contact potential difference across the sample. Force spectroscopy modes can measure individual molecular interactions. Thermal modes can measure thermal properties within the sample. Nanoindentation modes can measure sample hardness or softness.

2.1.3.4 AFM Cantilever

Common commercially available cantilevers are made out of Si_3N_4 and SiO_2. Typical AFM cantilever length ranges from 100 to 500 μm, width from 30 to 50 μm, thickness from 0.5 to 8 μm, force constant ranges from 0.06 to 50 N/m, and resonance frequency ranges from 1 kHz to 1 MHz. AFM tip radius of curvature is usually below 10 nm. Figure 2.8 shows a diagram of a straight shape cantilever.

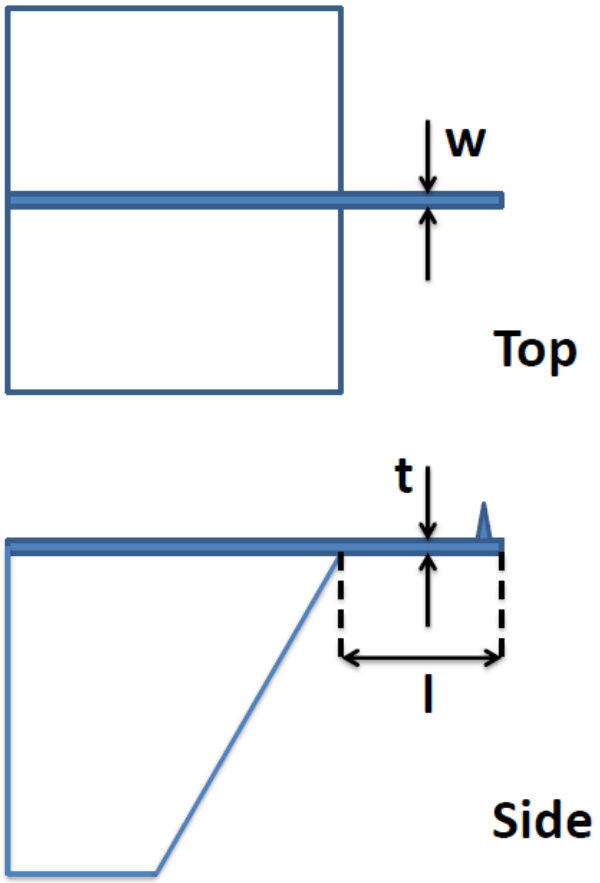

Figure 2.8: Straight shape cantilever

The softer the lever, the better it is for sensing deflection. However, this required a small mass to keep a high frequency. The resonance frequency of a cantilever is expressed by the following:

$$f_0 = \frac{1}{2\pi} \times \left(\frac{k}{m_0}\right)^{0.5} \tag{2.13}$$

$$k = \frac{Ewt^3}{4l^3} \tag{2.14}$$

where, k is the spring constant, E is the Young module, t is the thickness, l is the length, w is the width, m_0 is the effective mass of the lever. Typical resonance frequency is around 150 kHz.

2.1.4 Magnetic Induction Heating

The idea of magnetic induction heating originated when Michael Faraday discovered induced currents by a magnet. Later, James C. Maxwell developed the unified theory of electromagnetism. This was followed by James P. Joule describing the produced heat of current in a conductor, establishing the fundamental principles of magnetic induction heating.

In 1887 Sebastian Z. de Ferranti filed the first patent for the industrial application of melting metals by magnetic induction heating. In 1891 F. A. Kjellin demonstrated the first fully induction functional furnace. However, the major advancement in the area arrived when in 1916 Edwin F. Northrup developed the first high frequency induction furnace at Princeton University. During the same timeframe, M. G. Ribaud created high frequency induction heating technology by using spark-gap generators. Afterwards, Valentin P. Vologdin created induction heating generators using machine generators and vacuum tubes. During and after World War II the aircraft and automotive industry increased the use of induction heating mostly for melting metals. The magnetic induction heating technology went through a second major revolution with the development of solid-state generators. Yet, after the transistor was developed in 1945, it empowered the design of higher efficiency power converters, in turn, expanding magnetic induction heating to many applications. Magnetic induction heating has made a domestic application via cookers since the late 1980s. Lately, there has been a special interest in magnetic induction heating for medical applications for localized heating for hyperthermia treatment. Magnetic induction heating has been a revolutionizing technology that has impacted industrial [116-136], domestic [137-161] and medical [162-175] fields.

2.1.4.1 Magnetic Induction vs. Magnetic Field

There is a misperception about the difference between magnetic induction and magnetic field. The magnetic field *H* depicts the generated field generated by a free current only, where the magnetic induction depicts the field generated by a current plus the effect of magnetization of a material. Certain materials have the ability to increase and decrease the magnetic induction. These materials are called diamagnetic or paramagnetic. The relation between magnetic induction and magnetic field is constant.

$$B = \mu_0 \times H \tag{2.15}$$

where, μ_0 is the constant of permeability with a value of 4π x 10^{-7} Vs/Am or 1.256 x 10^{-6} Vs/Am in SI units. This relation extends to magnetic materials as well.

$$B = \mu_r \times \mu_0 \times H \tag{2.16}$$

where, μ_r equals 1 in vacuum or air and is able to reach values above 1000 for soft magnetic materials. Table 2.4 shows units for magnetic induction *B* and magnetic field *H* and Table 2.5 shows conversions for common magnetic units.

Table 2.4: Magnetic induction *B* and magnetic field *H* units

Unit System	Magnetic Induction *B*	Magnetic Field *H*
SI units	Tesla: 1 T = 1 Vs/Am^2	A/m
Older units	Gauss: 1 G = 10^{-4} T	Oersted: 1 Oe = $10^3/4\pi$ A/m

Table 2.5: Conversion table for common magnetic units

	mT (Tesla)	G (Gauss)	kA/m	Oe (Oersted)
1 mT	= 1.0000	= 10.000	= 0.7960*	= 10.000*
1 G	= 0.1000	= 1.0000	= 0.0796*	= 1.0000*
1 kA/m	= 1.2560*	= 12.560*	= 1.0000	= 12.560
1 Oe	= 0.1000*	= 1.0000*	= 0.0796	= 1.0000

* in free air

2.1.4.2 Magnetic Field Strength

The magnetic field strength (H) is a way to measure the magnetic field intensity. (H) can be measured in amperes per meter (A/m) or oersteds (Oe). The second way to measure magnetic field intensity is the magnetic flux density (B), which is measured in Newton-meters per ampere (Nm/A) and it is also called tesla (T). The presence of a magnetic field can be pictured as magnetic field lines. (H) relates to the density of these field lines. The total number of magnetic field lines penetrating an area is called magnetic flux. The unit for magnetic flux is tesla meter squared ($T*m^2$).

The following is a helical coil magnetic field calculation:

$$H = \frac{N \times I \times a^2}{2\ z^2+a^2\ ^{3/2}} \tag{2.17}$$

where, *N* is the number of turns in the coil, *I* is the current in amperes, *a* is the radius of the coil in meters, *z* is the distance from the center of the coil on the z axis in meters. Through this equation the magnetic field (H) can be calculated at any point on the z axis. See Figure 2.9 for illustration.

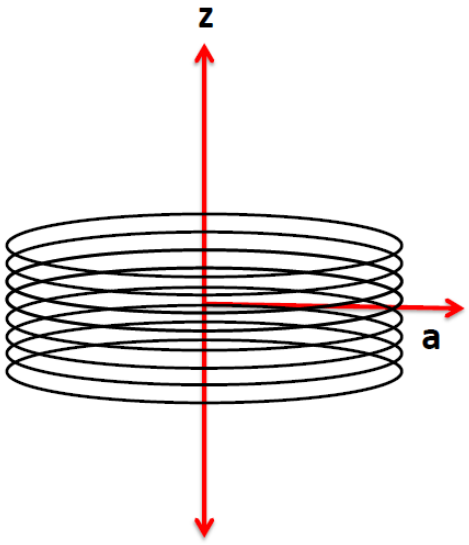

Figure 2.9: Helical coil

2.1.4.3 Coil Design

In coil design, an inductor is comparable to a primary transformer and the workpiece is comparable to a secondary transformer. For that reason, several transformer characteristics are useful in coil design. Some of the important transformer features that are consistent in coil design are the following: Efficiency of coupling between the windings is inversely proportional to the square of the distance between them. Also, the current in the primary transformer multiplied by the amount of primary turns is equal to the current in the secondary transformer multiplied by the number of the secondary turns. With this analogy in mind, there are several conditions that should be followed when designing a coil.

- The coil should be coupled to the part as close as possible for maximum energy transfer. This will ensure the largest number of flux lines intersecting the workpiece.
- The maximum number of flux lines in a solenoid coil is located at the center of the coil. Therefore, maximum heating rate is found at that location.
- Due to the fact that the magnetic flux is concentrated close to the coil turns, the geometric center of the coil has the weakest flux path.

After looking at these principles, it is clear to see that the center of a helical solenoid would have greatest amount of magnetic flux. Therefore, this would be the ideal coil for a sample to receive the highest possible magnetic field density.

Helical coils used around workpieces have the highest values of coil efficiency and internal coils have the lowest efficiency (See Table 2.6) [176]. To be clear, coil efficiency is energy that is delivered to the coil, which is transferred to the workpiece. Due to the fact that

heating pattern reflects the coil geometry, inductor shape is most likely the most important factor.

Table 2.6: Typical coupling efficiencies for inductor coils

Frequency	10 Hz		450 kHz	
Type of Coil	**Magnetic Steel**	**Other Metals**	**Magnetic Steel**	**Other Metals**
Helical	0.75	0.50	0.80	0.60
Pancake	0.35	0.25	0.50	0.30
Hairpin	0.45	0.30	0.60	0.40
One turn	0.60	0.40	0.70	0.50
Channel	0.65	0.45	0.70	0.50
Internal	0.40	0.20	0.50	0.25

2.1.4.4 Precision Induction Heating Instrument

A variety of magnetic induction heating systems have been used for hyperthermia applications [177-180], including home-built units [181, 182]. In literature, Ambrell EASYHEAT systems are some of the most popular units for hyperthermia experiments [183-189]. An Ambrell EASYHEAT 0224 nanoparticle heating system was used for the magnetic induction heating experiments in this dissertation. This system is a solid state induction heating system that converts three-phase line voltage to 2.4 kW terminal output over a range of radio frequencies (RF) and voltages. This energy is delivered to a remote series resonant circuit that includes the coil. The delivered power depends on the coupling efficiency of the coil geometry and proximity. Water is flowed through the system water head to limit any excess heat that may be produced by the internal components.

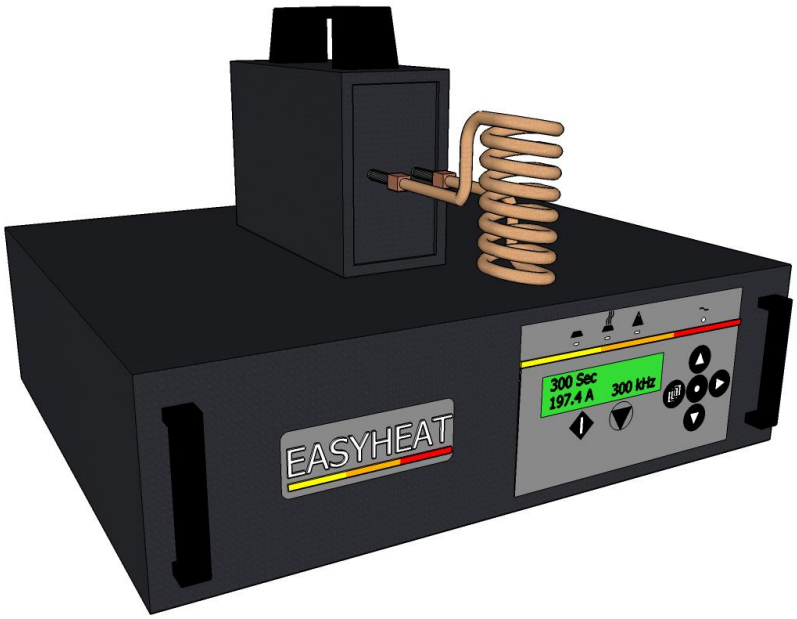

Figure 2.10: Ambrell EASYHEAT magnetic induction heating apparatus

The resonating frequency can be manipulated by changing capacitors in the workhead assembly. The coil used is an 8 turn helical coil with an inner diameter of 25 mm and a length of 43 mm. Table 2.7 shows the maximum obtainable magnetic field strength and output frequencies for each of the available capacitors.

Table 2.7: EASYHEAT 02402, 2.4kW generator

Workhead Capacitance (uf)	Individual Capacitance (uf)	Transformer Tap Setting	Operating Frequency (kHz)	Maximum Magnetic Field Strength (kA/m)
0.2	2 x 0.1	11	356	65
0.34	2 x 0.17	11	268	76.5
0.66	2 x 0.33	11	193	93
1.0	2 x 0.5	11	154	93.6

2.1.5 Thermomechanical Analysis

Thermomechanical Analyzers (TMA) measure a number of material properties, including coefficient of thermal expansion, heat deflection, melting temperature, elevated temperature

creep, and glass transition temperature. The need for TMAs grew for hardness or penetration tests, but they were first used for testing on polymers in 1948 [190].

2.1.5.1 Coefficient of Thermal Expansion

TMAs provide the coefficient of thermal expansion (CTE) α, which is a thermal property that measures the fractional increase in the length per unit rise in temperature. This expansion is due to the greater energy the molecules have in the presence of heat. Due to the fact that the molecules have more heat, they will expand as they move more rapidly.

The CTE may be documented as the mean $\alpha(\Delta T)$ or the differential α(T) and it is calculated in accordance with DIN 53 752 , ISO 113591part 1 and 2. The mean CTE is derived as follows:

$$\alpha(\Delta T) = \frac{1}{l_0} \times \frac{l_2 - l_1}{T_2 - T_1} = \frac{l}{l_0} \times \frac{\Delta l_{th}}{\Delta T} \quad [\frac{\mu m}{m\,°C}] \tag{2.18}$$

where α is the mean CTE in $°C^{-1}$, l_0 is the initial reference sample length in mm, Δl is the sample expansion in mm, and ΔT is the temperature change in mm. The differential CTE is derived as follows:

$$\alpha(T) = \frac{l}{l_0} \times \frac{dl_{th}}{dT} \quad [\frac{\mu m}{m\,°C}] \tag{2.19}$$

The CTE is calculated by the slope of the linear sections of the transition curve as demonstrated on Figure 2.11**.** It is common to report the CTE as two values, one below the glass transition temperature and one above glass transition temperature. This way the user can know how the material behaves at different thermal points. Large differences in the CTE can lead to internal stress build up and composite cracking or splitting. Since the CTE values are usually very small, it is common to express the measured expansion as part per million or ppm. The value of 0.000019 mm per mm would be expressed as 19 ppm. Therefore, CTE values may be given in units of µm/m°C or ppm/°C.

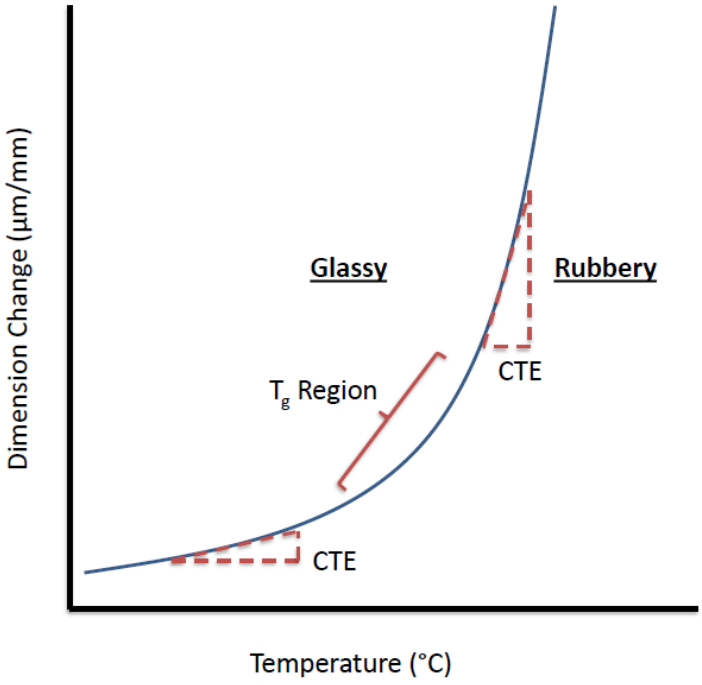

Figure 2.11: Coefficient of thermal expansion (CTE) curve

2.1.5.2 Glass Transition Temperature

The glass transition temperature (T_g) is the temperature range where a material transitions from hard or glassy state to a rubbery state. This temperature region is not linear. Also, it is important to note that the T_g is not a discrete thermodynamic transition, but a temperature range where the polymer chain mobility significantly increase. There are two factors that determine the T_g when working with epoxies, the chemical structure if the epoxy resin, the type of hardener, and the degree of cure. The T_g of a material can be located by looking at the CTE curve. The T_g is the point where a CTE change is identified, or where the two CTE curves intercept. Figure 2.12 shows the location of the T_g on a CTE curve.

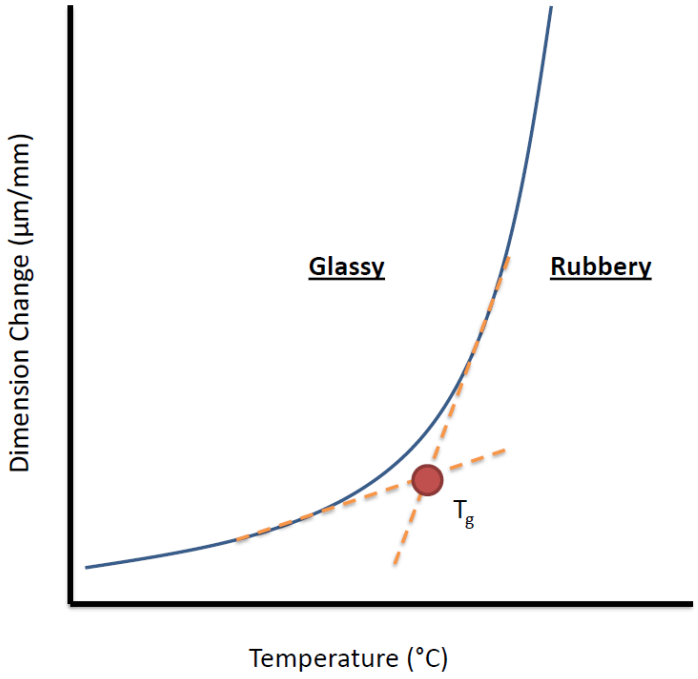

Figure 2.12: Location of the glass transition temperature (T_g) on a CTE curve

2.1.5.3 Thermal Expansion Measurement

The TMA instruments involve an analytical train that allows precise position measurements, a furnace or temperature control system, a heat sink, a thermocouple, a stage, and a probe. The stage and the probe are usually made out of quartz because of its low CTE.

The material of interest is required to be molded or cut into a small cylindrical or square shape with parallel ends. For expansion measurements using the TA Q400 system, the best dimensions is a cylinder-shaped sample with a minimum diameter of approximately 3 mm (it can be up to 10 mm) and a length of between 5 mm and 10 mm. Ideally, the sample diameter should be the same diameter as the probe diameter. For stable placement on stage and adequate resolution, it is important for the samples to be flat as possible, with parallel ends.

The system probe is placed on top of the sample, and as the sample is heated or cooled, the dimensional changes are measured by observing the probe motion. The heat is supplied by the system furnace. Figures 2.13 and 2.14 show a thermal expansion measurement setup.

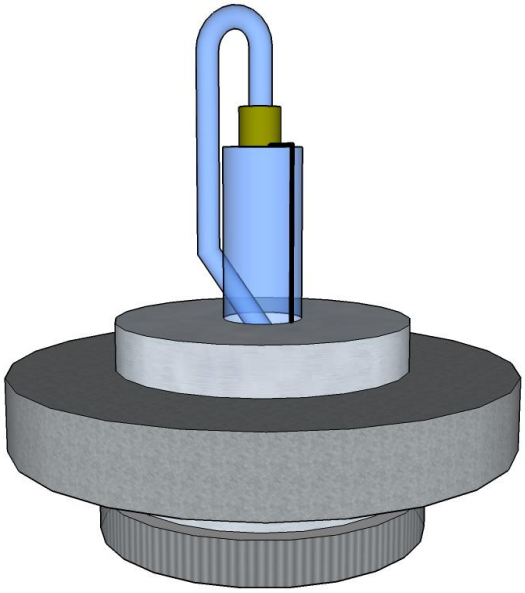

Figure 2.13: CTE measurement setup

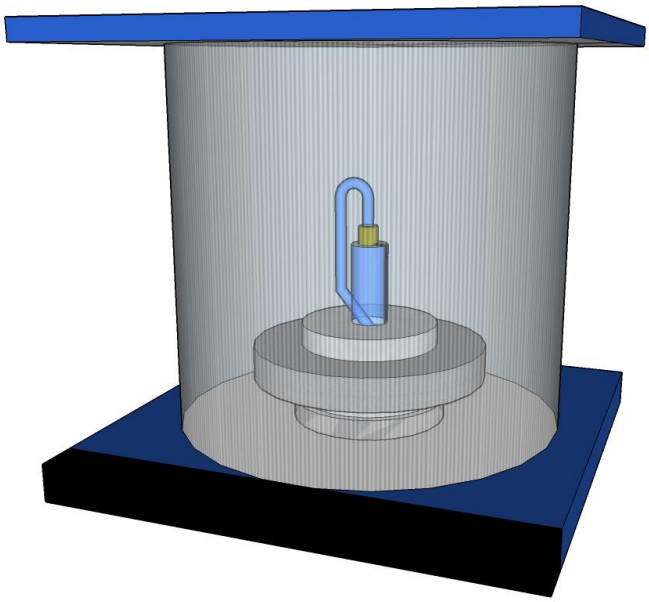

Figure 2.14: CTE measurement setup in furnace

2.2 Synthesis of Fe_3O_4 Nanoparticles

Fe_3O_4 nanoparticles were synthesized through a thermal decomposition reaction. Iron(III) acetylacetonate, oleylamine, ethanol hexane, benzyl ether and oleic acid were used for the synthesis. 50 ml of benzyl ether, 50 ml of oleylamine, and 3.5 g of iron salt (Iron(III) Acetylacetonate) were placed in a 500 ml three-neck bottom rounded flask. The mixture was magnetically stirred under continuous argon flow at room temperature for 5 minutes. The mixture was then heated at 110°C for 1 hour, by incrementing the temperature at a rate of 20°C per minute. The mixture is then heated up to 300°C to reflux for 2 hours, by incrementing the temperature at a rate of 20°C per minute. A continuous argon flow and magnetic stirring was maintained throughout the synthesis to maintain an inert environment and to ensure a homogenous result. 200 ml of ethanol were added to the resultant mixture. The precipitate was collected by centrifugation at 5000 rpm for 5 minutes. The synthesized magnetic nanoparticles were suspended in hexane, 0.05 ml of oleic acid, and 0.05 ml of oleylamine. Oleylamine behaves as a surface coating that hinders oxygen to react with the nanoparticles. The combination of oleic acid and oleylamine helps the stabilization of the nanoparticles in hexane for a longer period of time.

2.2.1 Characterization of Fe_3O_4 Nanoparticles

The synthesized Fe_3O_4 nanoparticles were characterized with the use of a transmission electron microscope (TEM). With the use of this microscope we were able to study the dispersion and morphology of the magnetic nanoparticles. 600 mg of Fe_3O_4 magnetic nanoperticles were suspended in 30 ml of Hexane using a 40 ml vial. The solution was agitated using a vortex mixer at 2200 rpm for 5 minutes, followed by ultrasonic bath placement for 5 minutes. 3 drops of solution were added to 2 ml of hexane to for dilution. The sample now

looked translucent. The diluted sample was agitated using a vortex mixer at 2200 rpm for 2 minutes, followed by ultrasonic bath placement for 2 minutes. One drop of the Fe_3O_4-hexane solution was placed on a copper coated TEM grid. The solvent was evaporated at 60°C for 5 minutes. Figure 2.15 shows a TEM image of the synthesized Fe_3O_4 nanoparticles demonstrating a mean size of 7±3 nm.

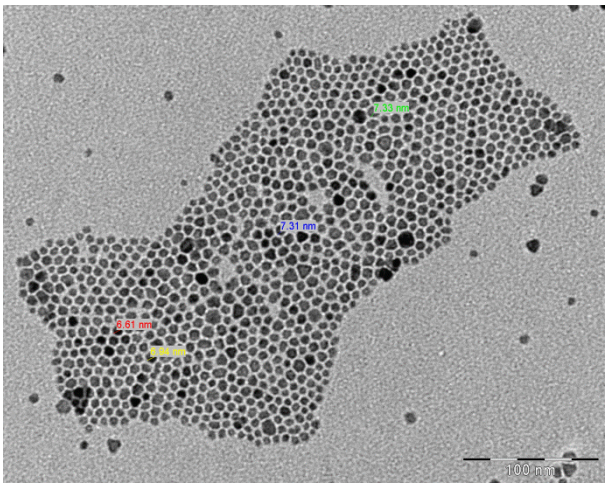

Figure 2.15: TEM image of Fe_3O_4 nanoparticles with mean size of 7±3 nm.

CHAPTER 3: POLY(N-ISOPROPYLACRYLAMIDE) CROSS-LINKED COATINGS WITH PHOTO-TUNABLE SWELLING

3.1 Notice to Reader

This chapter was published in Langmuir [191]. Permission is included in Appendix A.

3.2 Abstract

A series of terpolymers were synthesized comprising the following monomers: N-isopropylacrylamide (NIPAAm), a stimuli responsive structural unit that swells and collapses in response to temperature; methacryloxybenzophenone (MaBP), a photo-crosslinking unit that is activated at a wavelength of 365 nm; and phenacyl methacrylate (PHEm), a photolabile protected carboxyl group that can be deprotected at a wavelength of 254 nm. It is shown that the terpolymers can be photo-crosslinked at long UV wavelength light (λ = 365 nm) to establish surface-attached, cross-linked coatings and subsequently photo-chemically cleaved at short UV wavelength light (λ = 254 nm), which is found to be consistent with 1^{st} order kinetics. The photo-cleavage reaction produces free carboxylic groups, which can be used to locally tune the swelling characteristics and transition temperature of the coating, which depends on both the irradiation exposure and the overall PHEm content. For instance, for a terpolymer with 7.1 mole % PHEm, the transition temperature between the swollen and collapsed states increased from 20 to 50 °C at a pH of 8.5 with an exposure dose of 0.52 J/cm^2 at 254 nm. Finally, photo-cleavage can be used to create chemically patterned regions to provide a basis by which to conjugate cationic markers, proteins, or nanoparticles to the terpolymer coating.

3.3 Introduction

There has been significant interest in using light-sensitive polymers. Light is advantageous due to its ability to spatially target a specified area for modification. Moreover, wavelength selectivity can be accomplished through the absorption characteristics of the photosensitive moieties used.[57] There have been several reports of photosensitive moieties including azobenzene [58-62], coumarin [63, 64], *o*-nitrobenzyl [65, 66], pyrene [67], and spiropyran[62, 68, 192], all of which impart light-sensitivity, either in a reversible or irreversible.

Light-sensitivity can also be combined with other types of stimuli to develop multi-responsive polymers. So-called "smart" polymers, which undergo abrupt changes in solubility in response to an environmental cue, have been investigated as early as the 1960s by Heskins and Guillet. [37] Common stimuli include temperature [193], ionic strength [27], pH [28], electric fields [29], and magnetic fields [30]. One of the better known smart polymers is poly(N-isopropylacrylamide) (PNIPAAm), which is soluble in water below a temperature of approximately 32 ˚C and insoluble above 32 ˚C.[193] Stimuli responsive polymers have shown great potential in biomedical applications including tissue engineering [31], bio-separation[32], cell culture [33], bio-sensors [34], bio-actuation [35], and drug delivery. [36]

Here we present the synthesis and characterization of a series of multifunctional terpolymers based on the following monomers: 1. N-isopropylacrylamide (NIPAAm), a temperature responsive unit; 2. methacryloxybenzophenone (MaBP), a photo-crosslinkable unit that is activated at λ = 365 nm; and 3. phenacyl methacrylate (PHEm), which is the photo-labile protected acid that is deprotected at λ = 254 nm. Irradiation of a thin film of the terpolymer at λ = 365 nm drives structural patterning of the polymer through cross-linking of the benzophenone groups to neighboring aliphatic groups without deprotecting the PHEm. Subsequent patterning

at 254 nm generates acidic COOH groups, which is found to be consistent with 1st order kinetics. The presence of the deprotected regions causes pH-dependent swelling of the irradiated areas. The transition temperature between the swollen and collapsed states can be controlled depending on the PHEm content. At 7.1 mole % PHEm, the transition temperature between the swollen and collapsed states increased from 20 to 50 °C at a pH of 8.5 after irradiating the sample at 254 nm with a dose of 0.52 J/cm^2. At 17 mole % PHEm, while swelling of the irradiated regions increased after exposure to 254 nm, no transition temperature was observed, neither before nor after irradiation. Finally, deprotection permits attachment of positively charged groups, which is demonstrated by the selective binding of a cationic dye to irradiated regions.

3.4 Experimental Section

3.4.1 Materials

N-Isopropylacrylamide (NIPAAm), 4-hydroxybenzophenone, methacroyl chloride, triethylamine, silica gel, benzene, methacrylic acid, dimethylformamide, triethylamine, 2-bromo-4'-methoxyacetophenone, ethyl acetate, magnesium sulfate, 2,6-di-*tert*-butyl-4-methylphenol, hexane, azobisisobutyronitrile (AIBN), dioxane, diethyl ether, deuterated chloroform ($CDCl_3$), ethanol, 3-aminopropyltriethoxysilene, acetone, trizma base, and hydrochloric acid (HCL) (37%) were purchased from Sigma-Aldrich. YOYO-1 Iodide 1mM solution in DMSO was purchased from Life Technologies Corp. and diluted to obtain a 0.04 mM solution in water. Acetone was distilled from calcium hydride before use and NIPAAm was recrystallized from hexanes. All other chemicals were used as received.

3.4.2 Instruments

Nuclear magnetic resonance (NMR) spectroscopy was used to determine the chemical properties of the monomer, copolymer, and terpolymer. These materials were characterized and

confirmed with an INOVA 400 NMR spectrometer. All of the obtained spectra were measured in $CDCl_3$.

UV visible spectroscopy was used to confirm the photolytical cleavage by means of UV light. The photo-deprotection was observed through the use of a Shimadzu UV - 2101 /3101 PC UV-visible spectrometer.

The polymer solutions were spin-casted with a WS-650MZ-23NPP/LITE spin coater from Laurel Technologies Corporation. The polymers were spun with a two-step process; step 1 - 500 rpm for 10 seconds, followed by step 2 - 1200 rpm for 30 seconds. The samples were then cross-linked under a 365 nm UV light for 30 minutes.

Multiple-angle ellipsometry was used to determine both dry and swollen film thickness on a function of temperature. The ellipsometer uses an ATR-type configuration where the sample is spun on the backside of a LaSFN9 prism. The experimental set-up has been described by Habicht et al. [194] and detailed information about the measurement and fitting has been described previously.[195]

Flourescent microscopy images were taken to confirm attachment between the cationic fluorescent dye and the deprotected anionic polymer surface. The images were taken with a Nikon Eclipse Ti flourescent mircoscope. The flourescent dye attachment intensity was analyzed with the flourescent microscope's NIS – Elements Imaging software.

UV deprotection was accomplished with the use of a 90-0012-01 (11SC-1) UVP Pen-Ray mercury lamp. The lamp emits a mercury spectrum with primary energy at 254 nm. The power supply used was a 99-0055-01 (PS-1) UVP Pen-Ray power supply and delivers 115V at 60Hz with a nominal lamp current of 18 mA. At a distance of 0.75 cm above the sample, the lamp irradiates 4400 microwatts per cm^2.

3.4.3 Methacryloxybenzophenone (MaBP) Synthesis

MaBP was synthesized from 4-hydroxybenzophenone and methacroyl chloride at 0°C. Triethylamine was employed to work as an acid scavenger. The reaction ran for 5-6 hours. The collected product was run through a column for purification using silica gel as the stationary phase and benzene as the solvent. Finally, the monomer was collected and dried under vacuum.

3.4.4 Phenacyl Methacrylate (PHEm) Synthesis

PHEm was synthesized by following a procedure by Millaruelo et al.[196] Methacrylic acid, dimethylformamide, triethylamine, and 2-bromo-4'-methoxyacetophenone were mixed and stirred for 30 minutes at room temperature, allowing the blend to react. Water and ethyl acetate were then added. The aqueous phase of the solution was extracted three times by using ethyl acetate and the organic extract was collected and washed with water. The organic phase was dried with magnesium sulfate and filtered. A rotor evaporator was used to remove the solvent under pressure. A white solid product was obtained and purified by re-crystallization with 2,6-di-*tert*-butyl-4-methylphenol (thermal inhibitor) in hexane.

3.4.5 Copolymer and Terpolymer Synthesis

The poly(NIPAAm-*co*-MaBP) copolymer was polymerized with 3 mol% MaBP. The poly(NIPAAm-*co*-MaBP-*co*-PHEm) terpolymer was polymerized with 3 mol% MaBP and 5-20 mol% PHEm. Distilled dioxane was used as a solvent. The reactants with 1 mole% AIBN were placed in a Schlenk tube and degassed freeze-thaw cycles prior to the reaction. The reaction mixture was then placed in a water bath at 70°C for 18 hours. The polymers were then precipitated into diethyl ether. To verify composition, ^{1}H NMR in $CDCl_3$ was conducted. The mole percentage of MaBP was calculated from the integration of the aromatic hydrogens at δ = 7.2-8.0 ppm. The mole percentage of PHEm was calculated by the integration of the methylene

group (-CH2-) at $\delta = 5.2$ ppm. Both were referenced against the integration of the methyl groups ($-CH_3$) at $\delta = 1.0$ ppm. GPC on all samples were performed on a Viscotek ^{TM} using RI, VIS, RALS, and LALS. Molecular weights were determined by the triple detection method. Number-average molecular weights of ranged between 40,000 – 60,000 with a polydispersity of 3-4. The ^1H NMR spectrum of the terpolymer in $CDCl^3$ is shown in Figure 3.1 and the chemical structure of the synthesized terpolymer is shown in Figure 3.2. The compositions as calculated by ^1H NMR data are shown in Table 3.1.

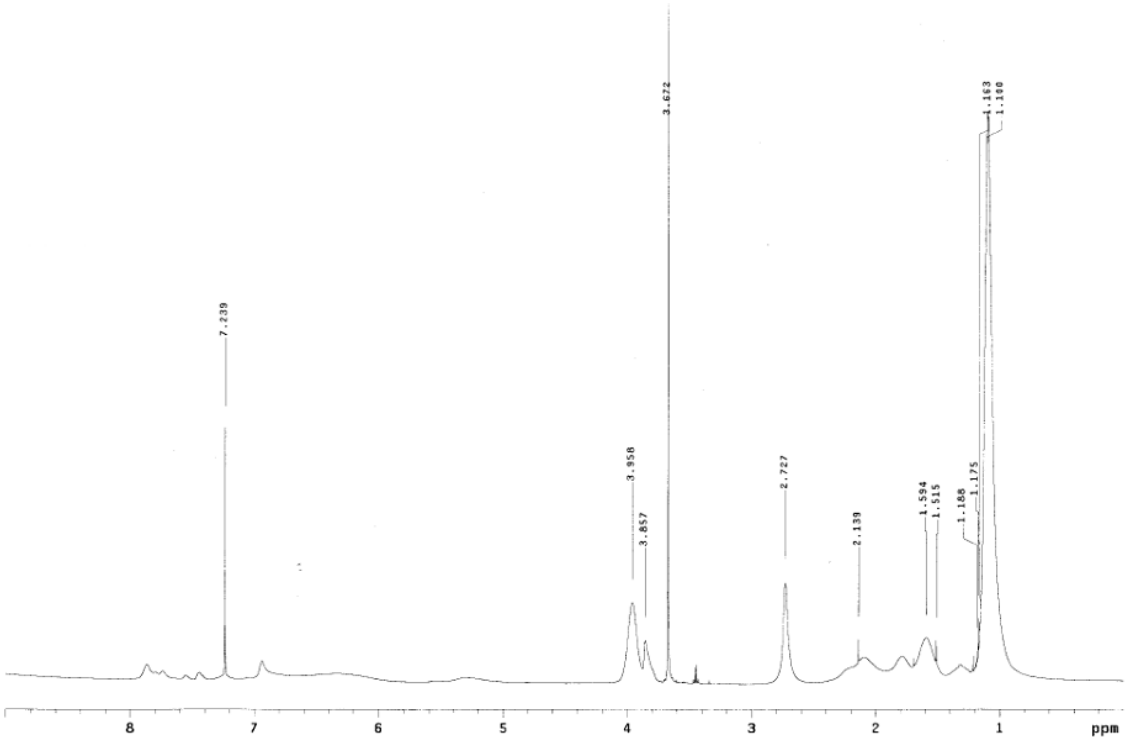

Figure 3.1: ^1H NMR spectrum of terpolymer poly(NIPAAm-*co*-MaBP-*co*-PHEm) in $CDCl_3$.

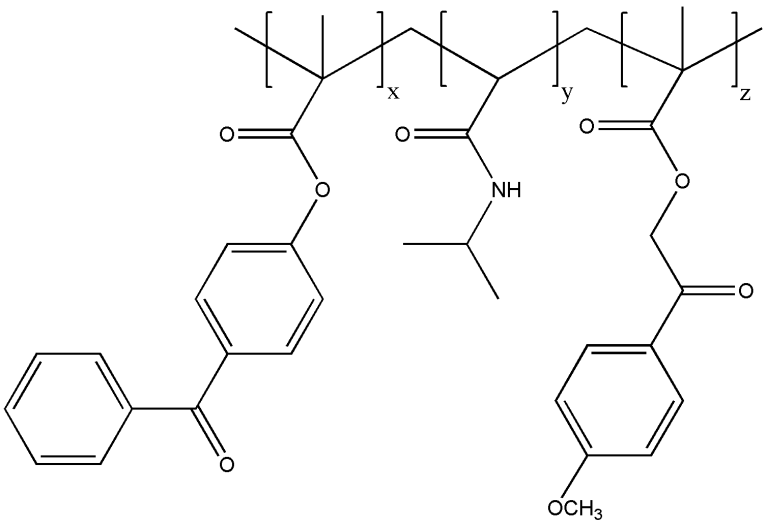

Figure 3.2: Terpolymer poly(NIPAAm-co-MaBP-co-PHEm) chemical structure.

Table 3.1: Composition of polymers. All percentages are given as mole %.

Sample	Feed		Calculated from ^{1}H NMR	
	MaBP(%)	**PHEm(%)**	**MaBP (%)**	**PHEm (%)**
Diblock	3.0	0.0	3.0	0
Terpolymer(5)	3.0	5.0	2.7	7.1
Terpolymer(10)	3.0	10.0	3.0	11.8
Terpolymer(20)	3.0	20.0	3.0	17.0

3.4.6 Fluorescent Marker Preparation

A flourescent dye solution was prepared following the procedure by Millaruelo et al. [197] YOYO-1 is a positively charged dye ideal for the cojugation with the deprotected, acidic areas in the terpolymer coating. A buffer solution was first prepared by dissolving 1.21 g of Trizma base in 100 mL of water and slowly adding HCL to adjust the pH down to 8.8. 10 μL of the YOYO-1 dye was mixed with 300 μL of the prepared buffer solution. The mixture was placed over the coating for 1 minute. The samples were then rinsed with DI water and dried under a nitrogen gas stream.

3.4.7 Photolithography Mask

A mask was developed to allow the 254 nm UV light to penetrate the desired areas in the terpolymer system, in turn, obtaining deprotected patterned areas. This mask was composed of 343 μm through-holes. AZ P4000 broadband photoresist was spin-casted over a silicon wafer. Spin-casting consisted of three steps; step 1 – 500 rpm for 10 seconds, step 2 – 1000 rpm for 40 seconds, and step 3 – hard bake at 115°C for 1.5 minutes. The obtained thickness was 15.6 μm. A Karl Suss MA-56 mask aligner was used at 25 mW for 120 seconds to perform photolithography and develop circle features on the silicon wafer. The wafer was then developed in AZ 400K developer (1:3 with DI water) for 40 seconds. An Adixen AMS 100 deep reactive ion etcher (DRIE) was used to etch the exposed silicon all the way through the wafer. The final step was to remove the photoresist with oxygen plasma.

3.4.8 Sample Characterization Preparation Techniques

The ellipsometer system is composed of a He-Ne laser with a wavelength of 633nm. A LaSFN9 prism with refractive index of 1.845 was used. The ellipsometry experiment examples were prepared by first cleaning the LaSFN9 prism with ozone to remove impurities. The prism was then treated with a 50 μl 3-aminopropyltriethoxysilane (in 5 ml acetone) for two minutes. Both the terpolymer and copolymer were both dissolved in dioxane and the concentration was adjusted to control the thickness. The polymer solutions were spin-casted with a WS-650MZ-23NPP/LITE spin coater from Laurel Technologies Corporation. The polymers were spun with a two-step process; step 1 - 500 rpm for 10 seconds, followed by step 2 - 1200 rpm for 30 seconds. The samples were then cross-linked under a 365 nm UV light for 30 minutes. The radiation of this long-wave UV light on the terpolymer film activates the n,π* transition in the benzophenone moieties causing a biradicaloid triplet state that abstracts a hydrogen from a neighboring

aliphatic C-H group, in turn, generating a stable C-C bond.[198] The prism was then rinsed with acetone and dried under a steady nitrogen gas flow.

For the UV visible spectroscopy experiments, 400 nm thick coatings were spun onto quartz substrates using the same procedure described above and cross-linked. UV spectra were taken before and after irradiation at 365 nm. Measurements were then performed after irradiation at 254 nm, each at specified time intervals.

3.5 Results and Discussion

A series of the (NIPAAm-*co*-MaBP-*co*-PHEm) terpolymers were synthesized, with the mole percent of PHEm varying from 7.1 to 17% while keeping the MaBP mole percent constant at 3 %. PHEm is a photolabile protected COOH group, which has previously been shown to undergo complete photo-deprotection when exposed to UV light (λ = 254 nm) in the presence of a hydrogen bond donor. Laser flash experiments have demonstrated that the initial point of the deprotection process is the hydrogen transfer from the solvent to the phenacyl carbonyl group.[199, 200] For the following experiments, all photo-cleavage experiments were performed after exposing the terpolymer coating to ethanol, which has been shown to be a good hydrogen donor for phenacyl esters.[201] Without this step, deprotection was not observed.

It is important to investigate how the thickness of poly(NIPAAm-*co*-MaBP-*co*-PHEm) system behaves after UV irradiation compared to the poly(NIPAAm-*co*-MaBP) thickness change under the same UV exposure. Therefore, we UV irradiated the poly(NIPAAm-*co*-MaBP) and poly(NIPAAm-*co*-MaBP-*co*-PHEm) to compare the resulting thickness. Figure 3.3 shows the thermally induced deswelling transition of the copolymer poly(NIPAAm-*co*-MaBP) and terpolymer poly(NIPAAm-*co*-MaBP-*co*-PHEm). It is important to observe that in both cases, the thickness of the materials increases after each UV irradiation. Since the irradiation is being

performed under ethanol environment, we are observing a reaction that allows the generation of OH groups, making the material more hydrophilic with each irradiation. Additionally, Figure 3.3(a) shows that although poly(NIPAAm-*co*-MaBP) was UV irradiated three times, the material underwent the collapsing sequence with a LCST around 35°C. On the other hand, Figure 3.3(b) shows that poly(NIPAAm-*co*-MaBP-*co*-PHEm) behaved very differently from poly(NIPAAm-*co*-MaBP). After UV irradiation, poly(NIPAAm-*co*-MaBP-*co*-PHEm) does not exhibit the same collapsing sequence as poly(NIPAAm-*co*-MaBP). We also observe that a shift takes place. This is due to the developed OH group charges, in turn, we obtain an increase in the transition temperature of the system. These results are consistent with the decrease of absorption in the UV-vis experiments, which confirms that the terpolymer is undergoing deprotection.

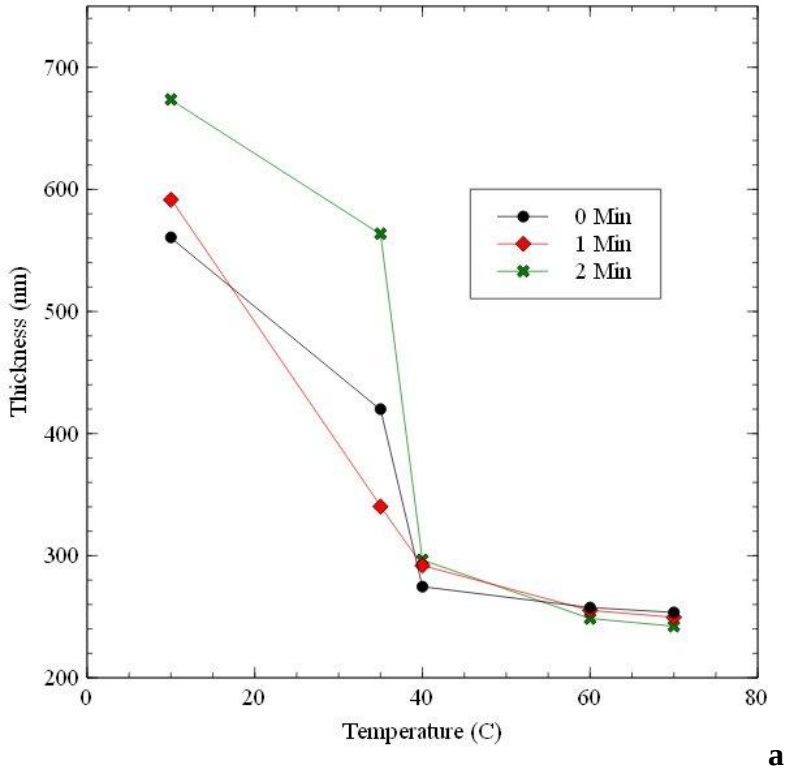

Figure 3.3: Film thickness change before and after UV irradiation of the copolymer poly(NIPAAm-*co*-MaBP) (a) and the terpolymer poly(NIPAAm-*co*-MaBP-*co*-PHEm) (b).

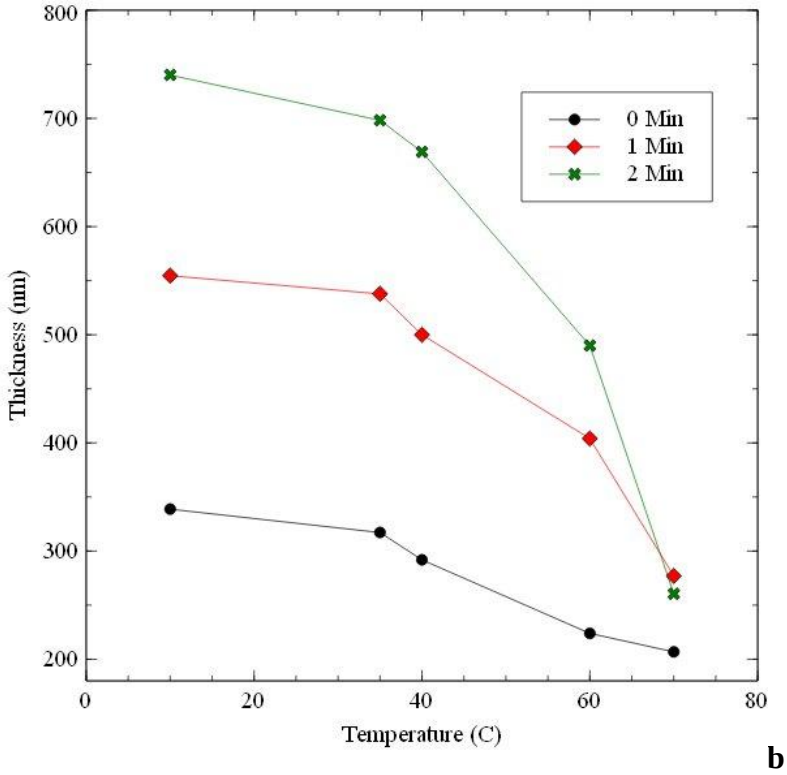

b

Figure 3.3: (Continued)

Figure 3.4 shows the degree of swelling vs. temperature of a 340 nm thick cross-linked terpolymer coating containing 7.1 % PHEm in water (pH = 8.5) as a function of UV radiation at 254 nm. Cross-linking was first carried out by irradiation of the coating at 365 nm with an intensity of 21,700 μW/cm^2 for a total of 30 minutes. This irradiation time was selected for two reasons. First, after 30 minutes, no leaching or loss of mass of the layer after irradiation was observed. Second, the 30 minute time ensured complete cross-linking with no aging effects. After cross-linking at 365 nm but prior to irradiation at 254 nm radiation, the swollen thickness at 15 °C is 625 nm (or a swelling ratio of 1.8) and the transition temperature between the swollen and collapsed state was 20 °C. The transition temperature is defined where the height of the layer is

$$H = (H_{swollen+}H_{collapsed})/2 \tag{3.1}$$

or half-way between the fully swollen state and the collapsed state. In comparison, the equivalent poly(NIPAAm-*co*-MaBP) polymer without PHEm swells to 790 nm (or a swelling ratio of 2.3) and has a transition temperature of 32 °C. The reduction in both the swelling ratio and transition temperature of the terpolymer is due to the hydrophobic nature of the PHEm.

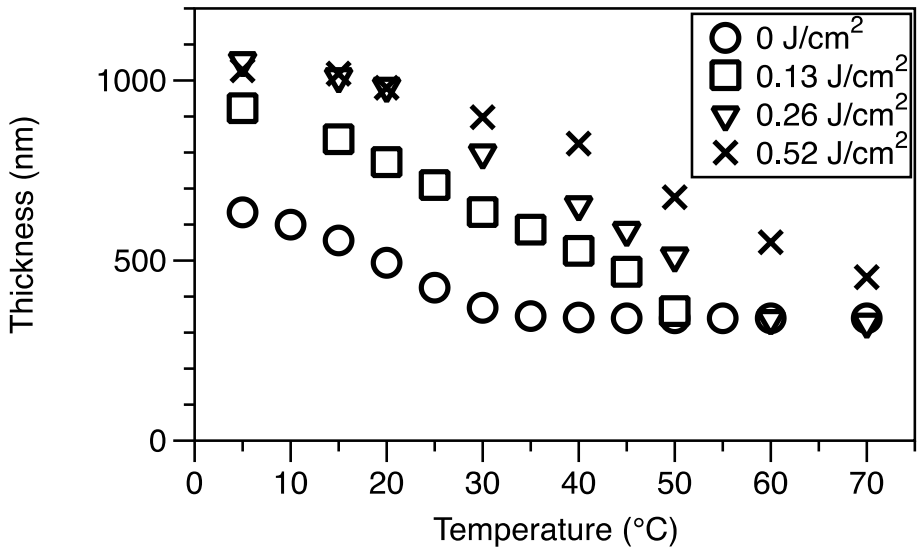

Figure 3.4: Thickness of poly(NIPAAm-*co*-MaBP-*co*-PHEm) cross-linked coatings versus temperature as a function of irradiation dosage at 254 nm. The PHEm content of the terpolymer is 7.1%, as determined by NMR. The dry layer thickness is 340 nm. Measurements are reproducible to within 5% of the reported thickness.

Irradiation of the cross-linked layer at 254 nm with an intensity of 4,400 μW/cm^2 for a period of 15, 30, 60 seconds (represented by an exposure dosage of 0.13, 0.26, and 0.52 J/cm^2, respectively) increases both the swollen thickness at 15 °C and the transition temperature, as shown in Figure 3.5. After 60 seconds of exposure, the degree of swelling of the terpolymer increased from 1.8 to 3.1 at 15 °C and the transition temperature increased from 20 to 50 °C. For comparison purposes, after 60 seconds of irradiation of the control, poly(NIPAAm-*co*-MaBP), the degree of swelling increased from 2.3 to 2.4 and there was negligible change in the transition temperature.

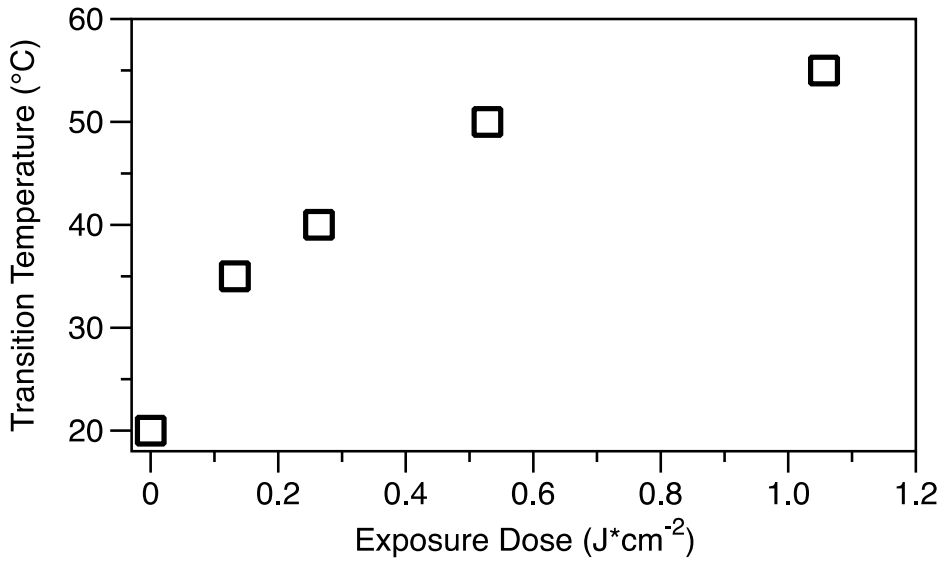

Figure 3.5: Transition temperature of poly(NIPAAm-*co*-MaBP-*co*-PHEm) cross-linked coatings as a function of irradiation at 254 nm. The PHEm content of the terpolymer is 7.1%, as determined by NMR.

As deprotected PHEm is a weak polyacid (methacrylic acid), the swelling vs. temperatures curves are highly dependent on pH. Figure 3.6 establishes the trend between swollen thickness at 15 °C and the fully protonated methacrylic acid (pH = 4.5) and unprotonated methacrylic acid (pH = 10.5). Interestingly, at pH 4.5, the swollen thickness is only weakly dependent on radiation dosage (presumably due to the hydrophobic nature of protonated methacrylic acid), whereas the swollen thickness at pH = 10.5 is strongly dependent on UV dosage, reaching a swelling ratio of 3.2 after 120 seconds of irradiation. This trend is presumably due to the strong influence of ionization on the degree of swelling.

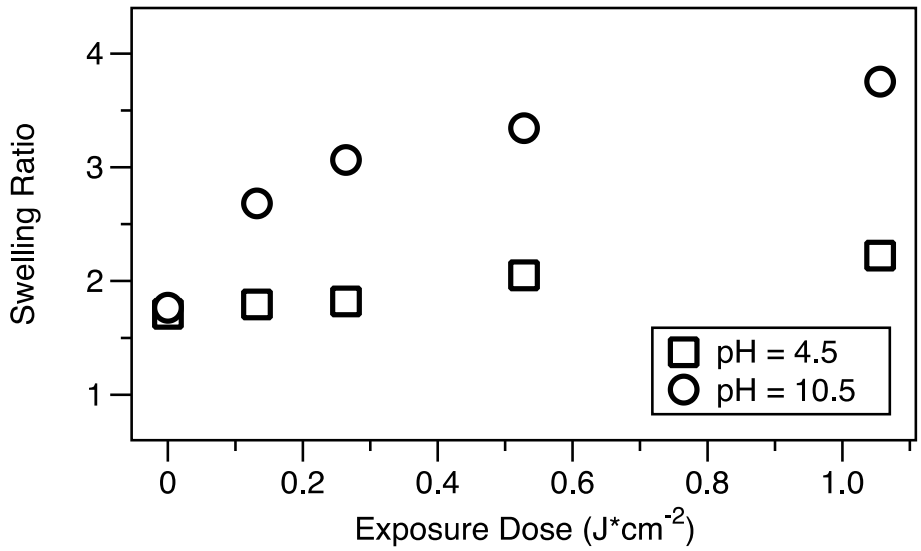

Figure 3.6: Swelling ratio of poly(NIPAAm-*co*-MaBP-*co*-PHEm) cross-linked coatings as a function of irradiation dose at 254 nm. The PHEm content of the terpolymer is 7.1%, as determined by NMR.

To put these results into better context, a sample with 17 % PHEm was also synthesized. Figure 3.7 shows the relationship between the degree of swelling as a function of radiation dosage upon exposure to both pH = 4.5 and pH 10.5 aqueous solutions. In contrast to the 7.1% sample, after cross-linking at 365 nm for 30 minutes but before deprotection at 254 nm, the terpolymer did not swell at 15 °C. At short irradiation times at 254 nm, the swollen thickness of the terpolymer coating increased at 15 °C for both pH = 4.5 and 10.5 samples. The pH = 4.5 samples level off at a swelling ratio of 1.8 and the pH = 10.5 samples level off at a swelling ratio of 3.5. At this high percentage of PHEm, moreover, a much narrower set of pH conditions were needed for a temperature transition between swollen and collapsed states, i.e. neither a clear transition was observed at pH = 4.5 nor 10.5. Transitions were observed near a neutral pH (pH = 7) but may also have been due to drifts in pH as the result of carbon dioxide absorption (which lowers the pH to 6). This is currently under further study.

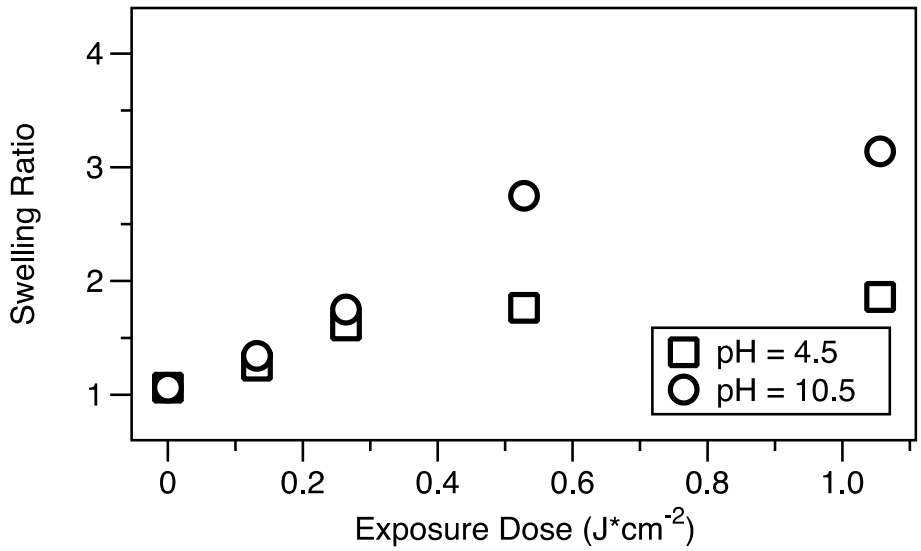

Figure 3.7: Swelling ratio of poly(NIPAAm-co-MaBP-co-PHEm) cross-linked coatings as a function of irradiation dose at 254 nm. The PHEm content of the terpolymer is 17%, as determined by NMR.

To verify the above experimental observations, the irradiation of both the terpolymer films (with PHEm) and copolymer films (without PHEm) were monitored with UV-Vis absorption. Polymers with PHEm exhibit a pronounced 270 nm absorption band that decreases when exposed to short wavelength (254nm) UV irradiation.[202] While the copolymer poly(NIPAAm-*co*-MaBP) also shows a small, but distinct, absorption peak at 270 nm, irradiation at 365 nm (the cross-linking wavelength) completely extinguishes the peak after 30 minutes. The terpolymer samples (with PHEm), on the other hand, still had a prominent peak at 270 nm after the 30 minute exposure at 365 nm. Further irradiation at 254 nm brought a reduction in the peak intensity, which fits first order reaction kinetics as shown in Figure 3.8. In this figure the change in the normalized absorbance is shown as a function of exposure dosage for the 7.1%, 11.8%, and 17% terpolymer samples. The best fit to the data yields a rate of constant of 0.79 $(J/cm^2)^{-1}$. Figure 3.9 shows the variation in the initial (non-normalized) absorbance at 270 nm for

the three samples. A best fit to the data yields an intercept close to 0, indicating that the absorbance is primarily due to PHEm.

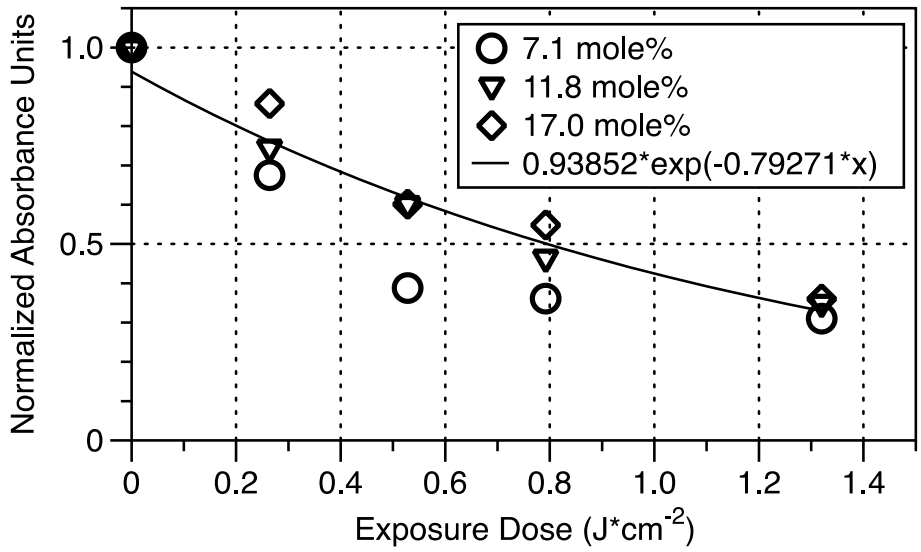

Figure 3.8: Normalized absorbance of poly(NIPAAm-*co*-MaBP-*co*-PHEm) cross-linked coatings for PHEm = 7.1 ,11.8, and 17%. The solid line represents a fit of 0.93852*exp(-.79271*x).

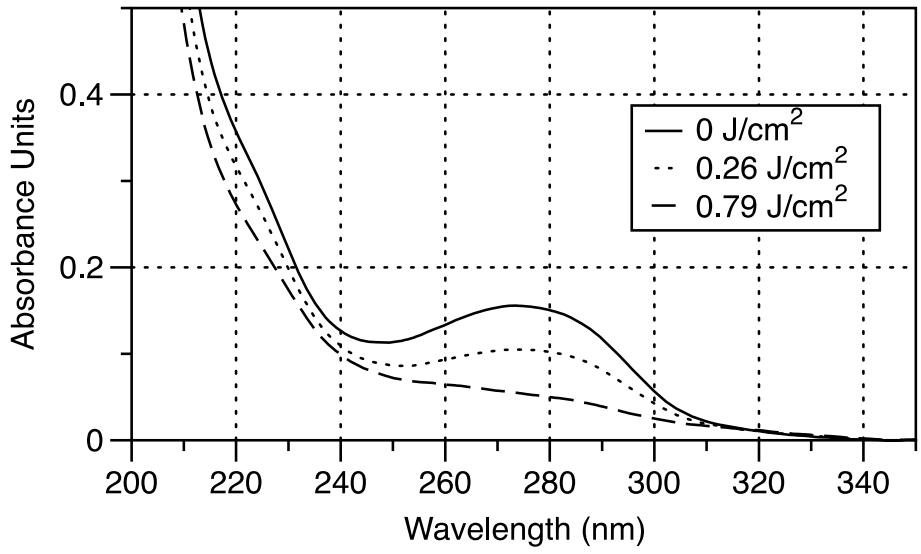

Figure 3.9: Absorbance of poly(NIPAAm-*co*-MaBP-*co*-PHEm) cross-linked coatings as a function of irradiation dose at 254 nm. The PHEm content of the terpolymer is 7.1%.

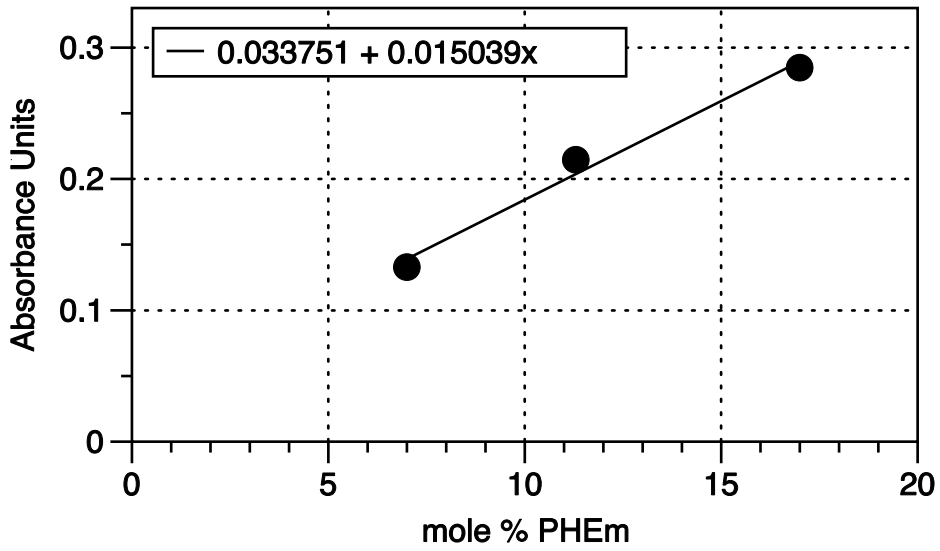

Figure 3.10: Absorbance of poly(NIPAAm-*co*-MaBP-*co*-PHEm) cross-linked coatings for PHEm = 7.1, 11.8, and 17% after irradiation at 365 nm for 30 minutes, but prior to irradiation at 254 nm. The solid line represents a fit to the data.

With the results of the kinetic experiments, the degree of ionization at pH=10.5 was postulated to be

$$f = (1 - A_{normalized}) * x_{PHEm} \tag{3.2}$$

where $A_{normalized}$ is the normalized absorbance and x_{PHEm} is the mole fraction of PHEm as determined by ^{1}H NMR. Based on equation 3.2, the degree of ionization was estimated for both the 7% and 17% samples as a function of radiation dose and plotted against the degree of swelling minus one, or (H/H_o - 1), at pH = 10.5 and 15 °C. Here, H_o is the dry layer thickness. Interestingly, both samples show power-law behavior, with a larger power-law exponent for the higher PHEm content terpolymer. This is somewhat expected as the 17% PHEm terpolymer does not swell without UV deprotection. At a degree of ionization of 0.06, both samples have a similar swelling ratio (2.8 for 17% PHEm versus 3.0 for 7.1% PHEm). At a degree of ionization of 10% for the 17% PHEm sample, the degree of swelling increases further to a value of 3.4.

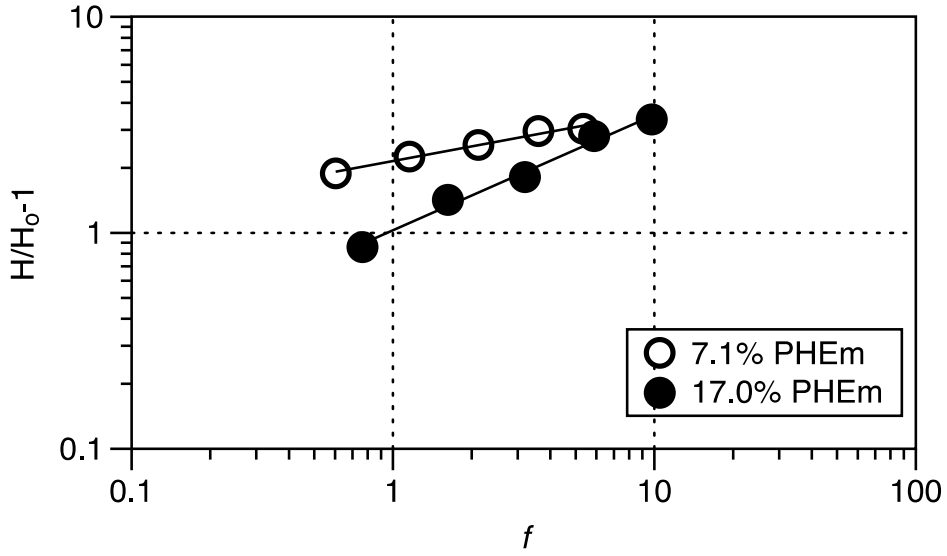

Figure 3.11: Ratio of the dimensionless swelling ration H/H_o-1 versus the calculated degree of ionization at pH = 10.5 and 15 °C.

The photo-deprotection of the PHEm monomer and the poly(NIPAAm-*co*-MaBP-*co*-PHEm) terpolymer were investigated through FTIR spectroscopy. PHEm and poly(NIPAAm-*co*-MaBP-*co*-PHEm) samples were prepared by suspending the powders in dioxane. The solutions were placed in a capped uv vis cell, followed by UV irradiating the samples with a 254nm UVP Pen-Ray for a variety of time frames. This was followed by spreading the solution across the ZnSe crystal. The experiments were performed at room temperature. The solutions were irradiated every hour and verified the results with the FTIR spectrometer. Attractive results were obtained after the solutions were UV irradiated overnight for a total of 19 hours. It is worth noting that the solutions went from a clear to a yellow color transformation after overnight irradiation. It is believed that the color change happened after the COOH acidic groups developed in the solution after the photolytical cleavage.

Figure 3.12(a) shows the FTIR spectrum of the poly(NIPAAm-*co*-MaBP) copolymer before 19 hours of UV irradiation and Figure 3.12(b) shows the FTIR spectrum of the

poly(NIPAAm-*co*-MaBP) copolymer after 19 hours of overnight UV irradiation. There are no significant changes in the spectrum. There was no appearance of newly developed peaks due to the photocleavage. This is expected, since the PHEm functional group is absent in this polymer. On the other hand, the poly(NIPAAm-*co*-MaBP-*co*-PHEm) terpolymer showed significant changes. Figure 3.12(c) shows the FTIR spectrum of poly(NIPAAm-*co*-MaBP-*co*-PHEm) before 19 hours of UV irradiation and Figure 3.12(d) shows the FTIR spectrum of poly(NIPAAm-*co*-MaBP-*co*-PHEm) after 19 hours of UV irradiation. Here we can observe the disappearance of 1600.57 cm^{-1} peak, which is linked to the aromatic signals. We also see the appearance of a large peak at 3307.79 cm^{-1}, linked to the OH group from carboxylic acids. These FTIR results are uniform with the experiments performed by Millaruelo et al. [197].

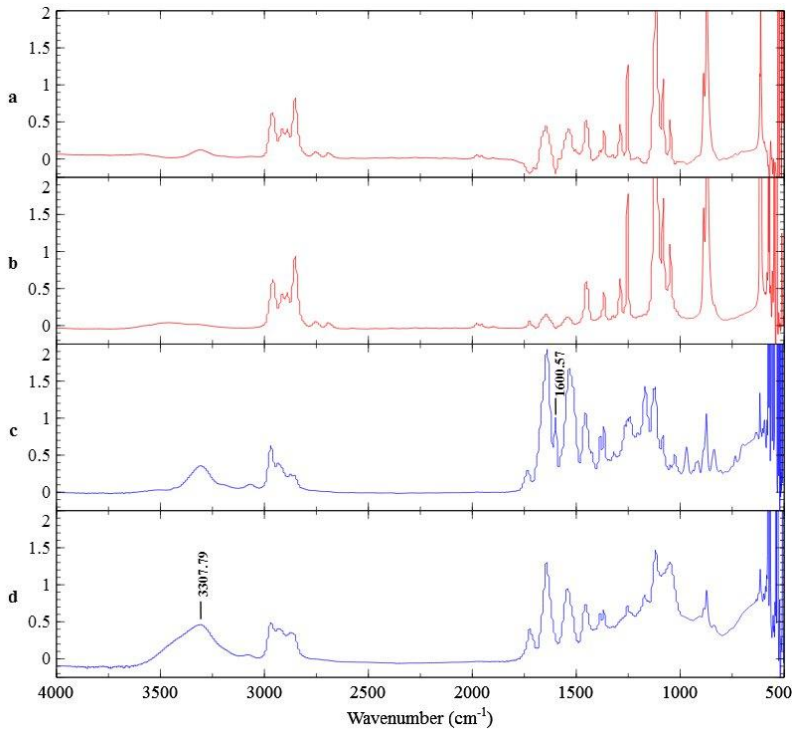

Figure 3.12: IR spectrum of copolymer poly(NIPAAm-*co*-MaBP before (a) and after(b) UV irradiation, and IR spectrum of terpolymer poly(NIPAAm-*co*-MaBP-*co*-PHEm) before (c) and after (d) UV irradiation

A poly(NIPAAm-*co*-MaBP-*co*-PHEm) and a poly(NIPAAm-*co*-MaBP) thin films were prepared to observe changes to their topography after irradiating the samples with a 254 nm wavelength UV light.

The samples were prepared by treating silicon wafer dies with a 50 µl 3-aminopropyltriethoxysilane + 5 ml acetone solution for two minutes. The silicon dies were then rinsed with acetone and dried under a steady nitrogen gas flow. Poly(NIPAAm-*co*-MaBP-*co*-PHEm) and poly(NIPAAm-*co*-MaBP) were both suspended in dioxane. The polymer solutions were spin-casted with a WS-650MZ-23NPP/LITE spin coater from Laurel Technologies Corporation. The polymers were spun with a two-step process; step 1 - 500 rpm for 10 seconds, followed by step2 - 1200 rpm for 30 seconds. The samples were then crosslinked under a 365nm UV light for 30 minutes. The poly(NIPAAm-*co*-MaBP-*co*-PHEm) samples were deprotected by submerging the samples in ethanol and radiating the samples with a 254nm UV light at different time intervals.

Figure 3.13 shows 2D AFM results of irradiated poly(NIPAAm-*co*-MaBP-*co*-PHEm) and poly(NIPAAm-*co*-MaBP) samples. These experiments were run in five minute intervals for up to 20 minutes. Our intention is to observe how the irradiated sample surfaces change over time. As we anticipated, since the poly(NIPAAm-*co*-MaBP) does not contain the photolabile phenacyl group there is no change to the topography of the film after timed irradiation. On the other hand, the poly(NIPAAm-*co*-MaBP-*co*-PHEm) sample exhibited significant topographical changes at different irradiation times. It was concluded that the optimal UV irradiation time was between five and ten minutes. Samples that were irradiated for more than ten minutes showcased a degradation of the polymer film. The root mean square (RMS) capability of the AFM NanoScope software is used to determine the surface roughness of a film sample by

determining the standard deviation of the Z values of a scanned area. The poly(NIPAAm-*co*-MaBP) and poly(NIPAAm-*co*-MaBP-*co*-PHEm) surface roughness change after irradiation time is demonstrated in Figure 3.14. Here the results are consistent with the results obtained from the AFM scans. We can see that poly(NIPAAm-*co*-MaBP-*co*-PHEm) displays a significant surface roughness increase after five and ten minutes. Consistent with our previous observation, the surface roughness for minutes fifteen and twenty decreases due to polymer degradation. The poly(NIPAAm-*co*-MaBP) surface roughness results are also consistent with the AFM scan results, since there is no significant change of surface roughness throughout the irradiation time.

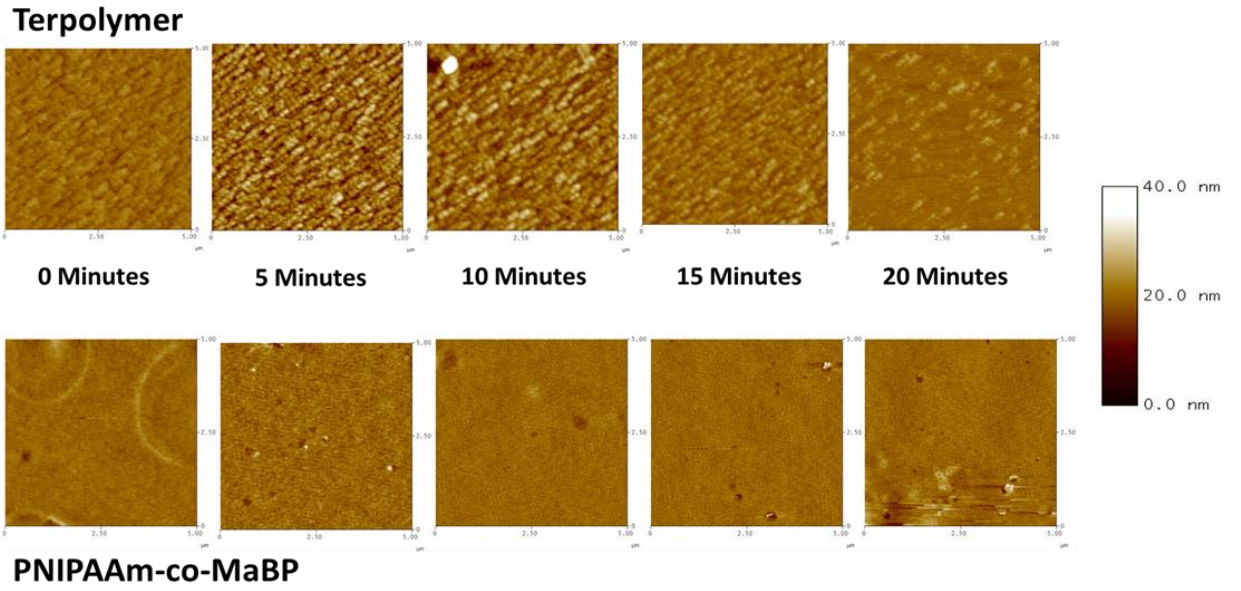

Figure 3.13: AFM 2D images of the terpolymer poly(NIPAAm-*co*-MaBP-*co*-PHEm) irradiated over time

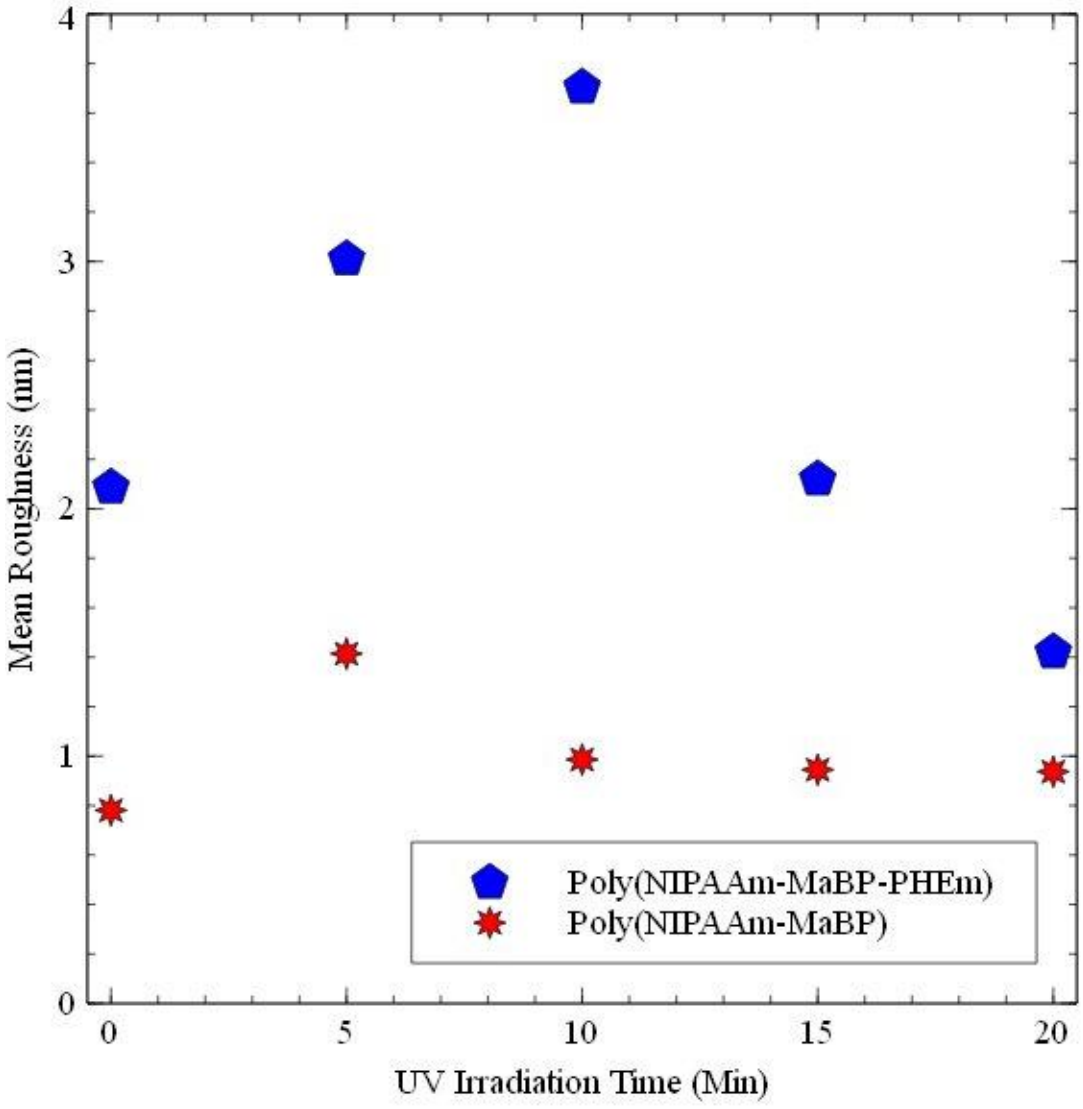

Figure 3.14: Mean roughness of poly(NIPAAm-*co*-MaBP) and poly(NIPAAm-*co*-MaBP-*co*-PHEm) samples after UV irradiation

After irradiating the crosslinked terpolymer at 254 nm, the PHEm groups are switched to anionic acidic groups. These anionic regions can be utilized to conjugate with cationic markers, proteins, or nanoparticles. Here the cationic fluorescent dye YOYO-1 was used as a marker to identify the electrostatic interaction between the cationic dye and the anionic region of the deprotected terpolymer. Figure 3.15 illustrates the developing process.

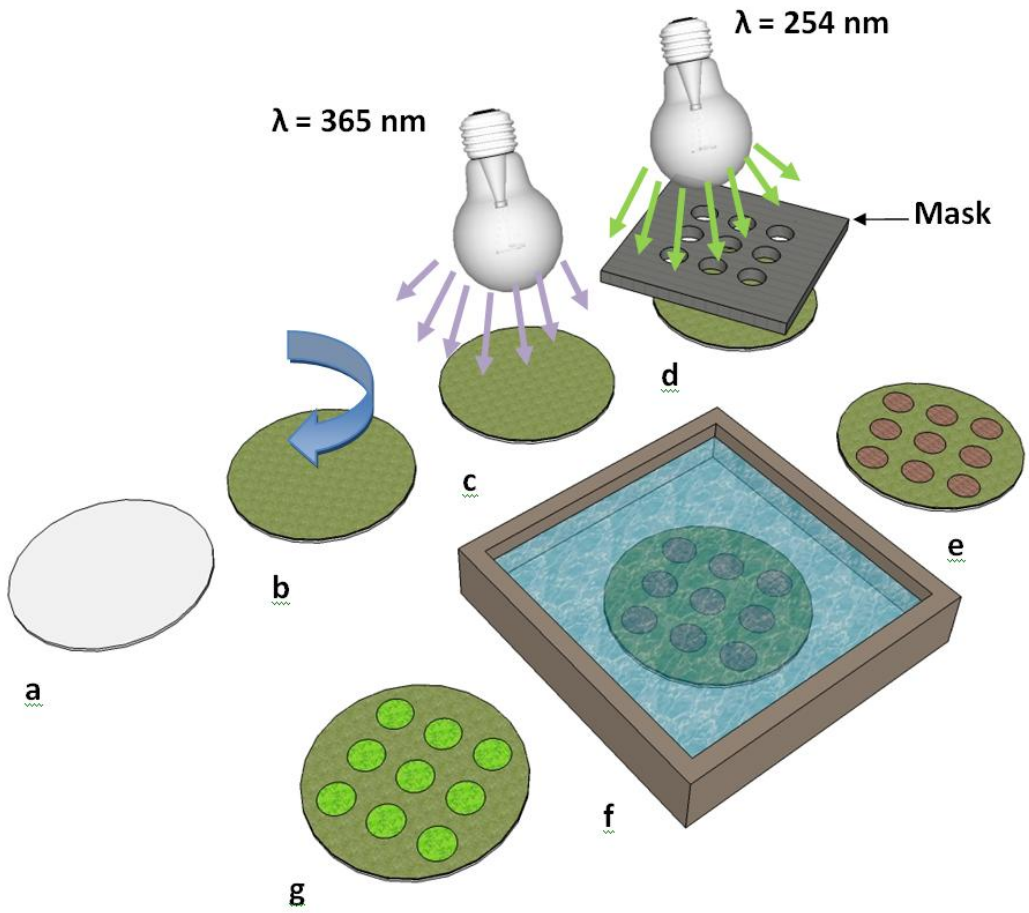

Figure 3.15: Micro patterning development process: (a) plain silicon wafer (b) spin-casting the terpolymer (c) crosslinking the terpolymer with a 365 nm UV light (d) deprotecting the terpolymer with a 254 nm UV light (e) terpolymer with deprotected (acid) pattern (f) exposing the deprotected terpolymer to fluorescent dye (g) attaching the cationic fluorescent dye to the anionic functionalized regions.

Small poly(NIPAAm-*co*-MaBP) and poly(NIPAAm-*co*-MaBP-*co*-PHEm) thin film samples were prepared for this experiment. The sample preparation procedure from the AFM section was followed. A mask was fabricated to allow the 254 nm UV light to penetrate the desired areas in the terpolymer system, in turn, obtaining deprotected patterned areas. This mask was composed of 343 μm through-holes. Once the terpolymer was crossklinked, the sample was rinsed in ethanol and placed under the silicon wafer mask. The samples were then exposed to a 254 nm UV light for deprotection at different time intervals to identify optimal irradiation time.

A flourescent dye solution was prepared following the procedure by Millaruelo et al. [197]. YOYO-1 is a positively charged dye ideal for the cojugation with the deprotected, acidic areas in the poly(NIPAAm-*co*-MaBP-*co*-PHEm) film. A buffer solution was first prepared by dissolving 1.21 g of Trizma base in 100 mL of water and slowly adding HCL to adjust the pH down to 8.8. 10 μL of the YOYO-1 dye was mixed with 300 μL of the prepared buffer solution. The mixture was placed over the deprotected areas for 1 minute. The samples were then rinsed with DI water and dried under a nitrogen gas stream.

Figure 3.16 shows the attachment of the flourescent dye to the areas containing the carboxyl group. When looking at the poly(NIPAAm-*co*-MaBP-*co*-PHEm) results, we can observe that the inside of the circles (irradiated area) is brighter than its surroundings, this means that the cationic flourescent dye conjugated with the anionic deprotected areas of the film. Yet, it is clear to see that the poly(NIPAAm-*co*-MaBP) film did not exhibit any flourescent dye attachment. It is worth noting that when the samples were irradiated with a 254 nm UV light for deprotection, both the poly(NIPAAm-*co*-MaBP) and poly(NIPAAm-*co*-MaBP-*co*-PHEm) films displayed a dark color change on their surface. The results obtained in the AFM experiments lead us to believe that this color change is due to the beginning stage of polymer degradation. Still, we only observe flourescent dye attachment to the poly(NIPAAm-*co*-MaBP-*co*-PHEm) film. Furthermore, according to these results the optimal sample irradaiton time for flourescent dye attachment is around 8 minutes. These results are consistent with the irradiation time results obtained in the AFM experiments.

The flourescent dye attachment intensity was analyzed with the flourescent microscope's NIS – Elements Imaging software. Figure 3.17 (a) shows the flourescent intensity profile and surface plot of the YOYO-1 attachment to the poly(NIPAAm-*co*-MaBP-*co*-PHEm) film. It is

clear to see the flourescent dye is concentrated at the center of the circle, which is the deprotected, carboxylic group area. On the other hand, Figure 3.17(b) shows the flourescent intensity profile and surface plot of the YOYO-1 attachment to the poly(NIPAAm-*co*-MaBP) film. Here we can observe that there is no attachment of the flourescent dye on the poly(NIPAAm-*co*-MaBP) surface.

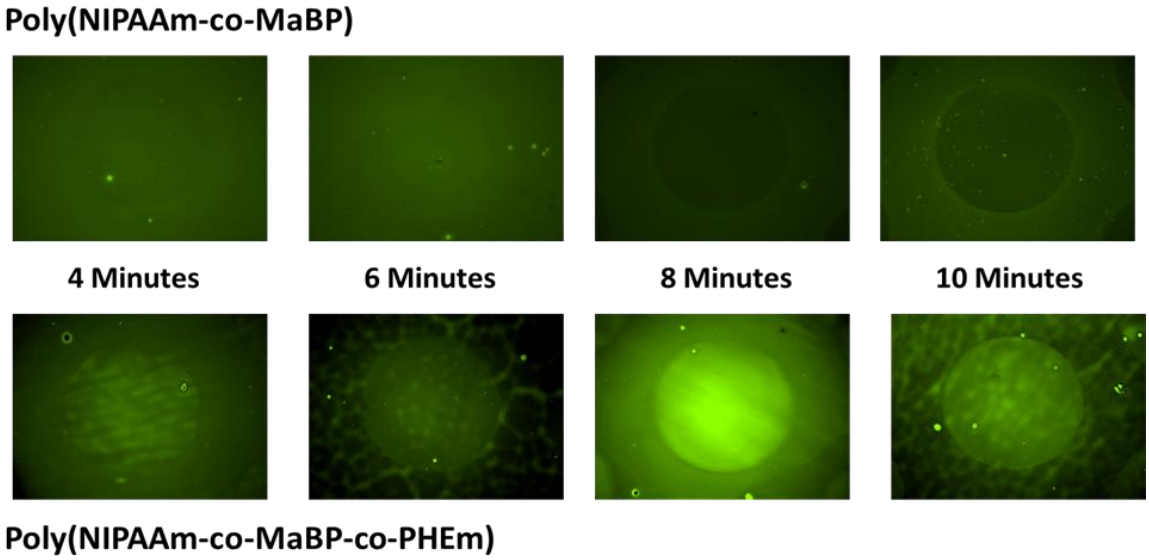

Figure 3.16: Fluorescent dye attachment over various irradiation times

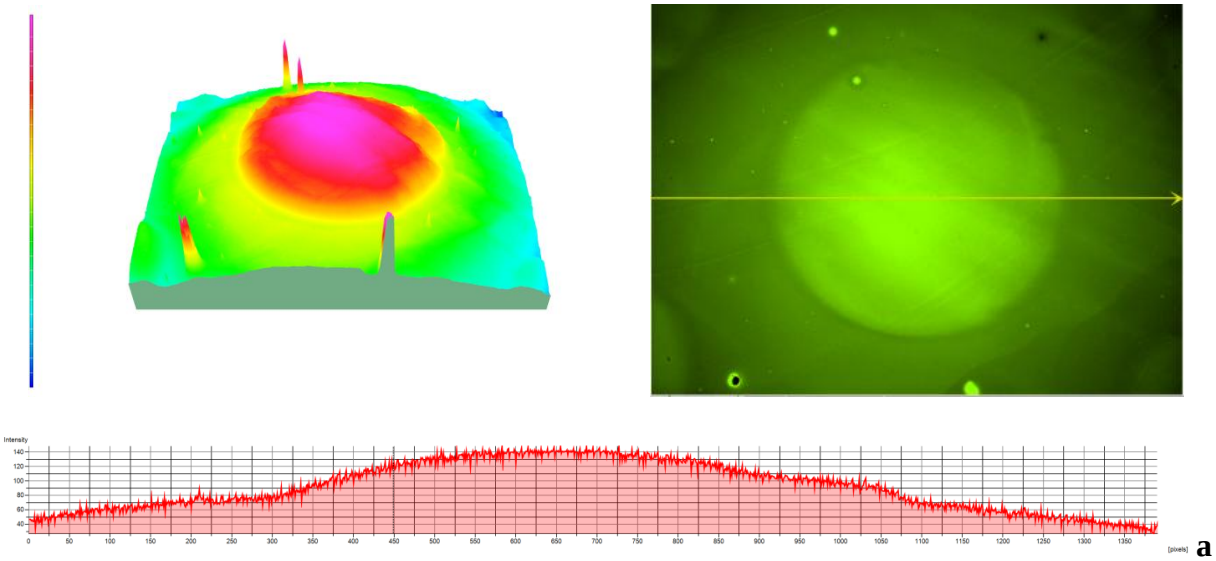

a

Figure 3.17: Fluorescent dye intensity profile of terpolymer poly(NIPAAm-co-MaBP-co-PHEm) (a) and copolymer poly(NIPAAm-co-MaBP) (b)

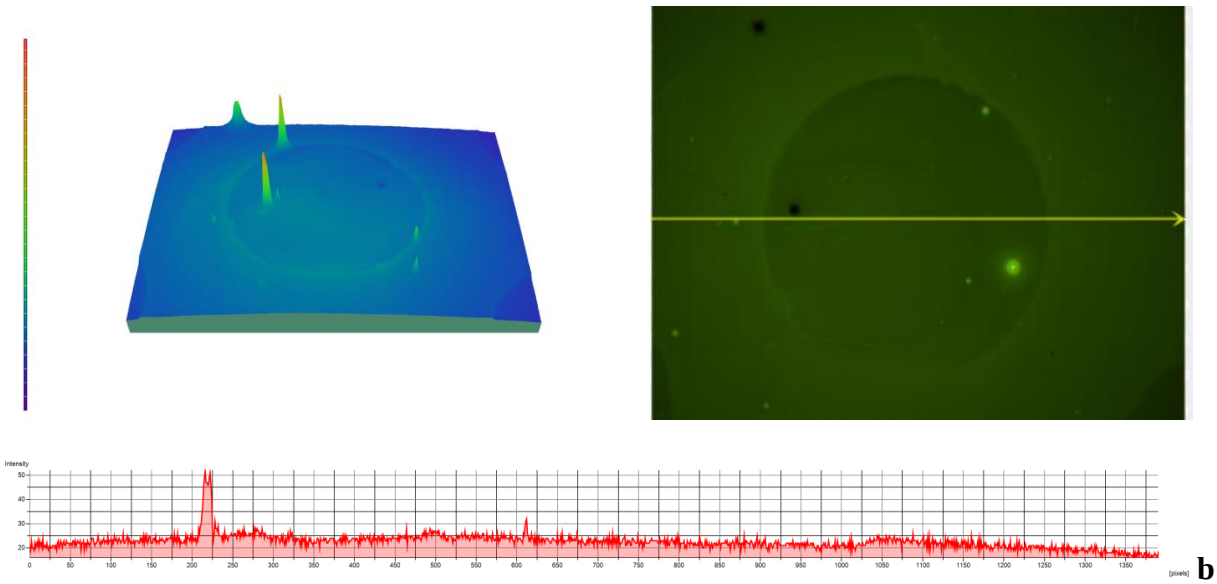

b

Figure 3.17: (Continued)

Figure 3.18 shows the attachment of YOYO-1 to a patterned region in the terpolymer (with 11.8 mole% PHEm) after irradiation at 254 nm for 4 minutes (or 2.0 J/cm^2). For comparison purposes, a control of a patterned diblock (without PHEm) coating is also shown, which shows negligible adsorption after UV exposure. More interesting, however, is the distinct wrinkle pattern observed in the patterned terpolymer coating. The principal reason is that the deprotected section swells by a factor of 4, but the unexposed region swells only by a factor of 1.3. Hence, the deprotected area swells more than the surroundings and is under a state of biaxial stress, which is relieved through wrinkling.[203] This could for example motivate the use of light to modify both chemical and topographical properties, both of which impact surface properties including, friction and adhesion.

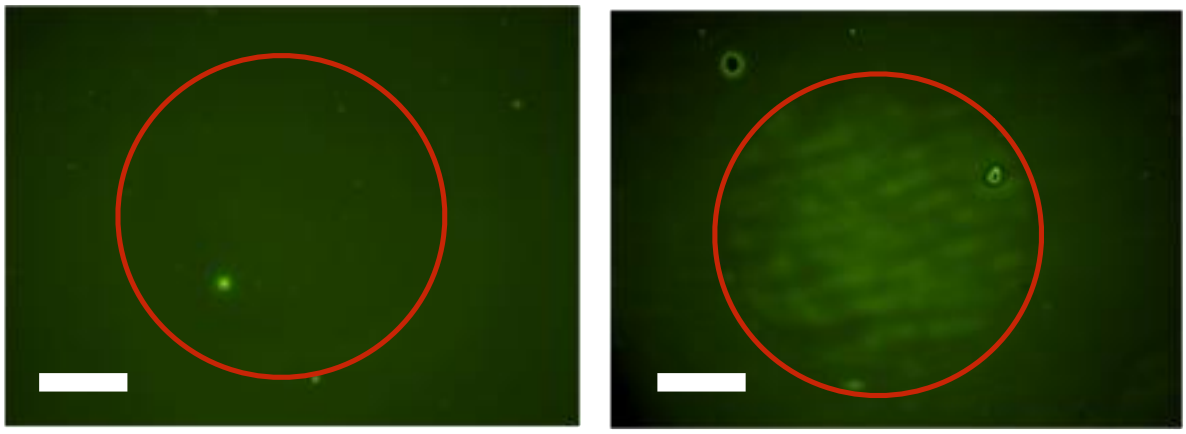

(A) Without PHEm (B) 11.8% PHEm

Figure 3.18: Adsorption of YOYO-1 fluorescent dye to a patterned, cross-linked coating of the copolymer (A) without PHEm and the terpolymer (B) with 11.8% PHEm. The red circle denotes the region of UV irradiation at 254 nm for a total dose of 2.0 J/cm^2. YOYO-1 preferentially absorbs to only the irradiated region of the terpolymer. The scale bar represents 100 μm.

3.6 Conclusions

The synthesis and characterization of photo-crosslinkable, photolabile, and thermally responsive terpolymers have been investigated. Copolymer (without PHEm) and terpolymer thin-films were covalently cross-linked at 365 nm and subsequently deprotected at 254 nm. Changes to swelling and de-swelling of the coatings were monitored by ellipsometry, which shows that the PHEm loading is important in controlling the swelling behavior. Photocleavage properties of the terpolymer were confirmed by UV-Vis, which show that deprotection is consistent with 1st order kinetics. YOYO-1, a positively charged fluorescent dye was used to mimic the attachment of positive charged nanoparticles. The fluorescent microscopy experiments confirmed the electrostatic interaction between the dye and the deprotected terpolymer surfaces compared to the absence of dye attachment to the copolymer. In conclusion, photocleavage of the terpolymer can be used to locally tune the swelling characteristics and transition temperature of the coating, as well as to provide a basis by which to conjugate cationic

markers, proteins, or nanoparticles to the terpolymer coating, which could have important consequences for nano-processing and new methods for designing responsive coatings.

CHAPTER 4: REMOTELY CONTROLLED SMART SURFACES VIA Fe_3O_4 NANO-OCTOPOD EMBEDDED POLY(N-ISOPROPYLACRYLAMIDE)

4.1 Introduction

Biofouling is the unwanted deposition and growth of micro-organisms on surfaces. Therefore, antifouling processes and techniques are desired for removing or preventing these micro-organisms from forming. Antifouling applications can be seen in marine systems [204-206], industrial equipment [207], textiles [208-211], food packaging [212-214], food storage [215], water purification systems [216-218], medical devices [219-221], medical implants [222-224], and biosensors [225-228].

Biofouling continues to be a significant challenge to be addressed. In fact, it is a major reason for biosensor failure [229-231]. Several approaches have been implemented to minimize or eliminate the biofouling issue. Poly(ethylene glycol) (PEG) has been an attractive polymer for surface coatings since water soluble analytes can disperse through the water-soluble polymer gel. PEG has also shown to withstand the non-specific adsorption of proteins [232, 233]. However, PEG-based groups can autoxidate when exposed to oxygen, which may react with proteins [234]. Self-assembled monolayers (SAMs) based on alkane thiolates and polymeric coatings are popular and effective approaches for reducing the non-desired protein and biomolecule adsorption [235-237]. However, it does not avoid protein adsorption on many common surfaces and it is not practical for use in microfluidics due to the difficulty to obtain an evenly coated layer. The grafting of phospholipids or derivatives of phosphorylcholine on

surfaces has also been studied [238, 239]. Additionally, carbohydrate derivatized surfaces have shown to resist adsorption of proteins [240, 241].

The subsequent generation of biomedical devices are micron-scaled systems that will be operated in surgery, biomedical diagnostics and therapeutic management [242]. Investigations are focusing on the area of smart materials, piezoelectric materials, and microfluidic technology, which provides faster screening of diseases, along with painless and effective drug delivery [243].

In order to improve the heating efficiency of the nanoparticles, different strategies have been proposed in the last few years, including tuning their size, saturation magnetization and effective anisotropy [244, 245]. To this respect, it has been shown that by changing the shape of the nanoparticles, for example cubes instead of the typical spheres, the surface anisotropy of the nanoparticles increases and the heating efficiency or specific absorption rate (SAR) also increases [246]. Considering this, Fe_3O_4 nanoparticles were synthesized with enhanced surface anisotropy, octopods, and used to improve the response time of the polymer micro-actuators during the heating experiments, as will be shown later.

The purpose of this work is to present the fabrication technology of surface attached magnetic hydrogel micro-manipulators that undergo surface physical contortions in the presence of AC magnetic fields. This approach can serve as a non-contact mechanical approach for micromanipulation or to mitigate any undesired biofouling on surfaces. Not much work has been done in this type of mechanical lab-on-a-chip (LOC) device approach for biofouling removal. To the best of our knowledge this is the first time that surface attached magnetic hydrogel micro-actuators have been reported. This method makes it appealing for batch-producible microfluidic micro-actuators.

4.2 Experimental Section

4.2.1 Materials

The magnetite nanoparticles (Fe_3O_4, 99.5%, 25 nm) were purchased from Nanostructured & Amorphous Materials, Inc. The 50 μm NIST NT34N traceable polystyrene particles were obtained from Bangs Laboratories, Inc. The polydimethylsiloxane (PDMS) SYLGARD® 184 silicone elastomer kit was acquired from Dow Corning. The SU-8 2035 photoresist and OmniCoat were purchased from MicroChem. N-Isopropylacrylamide (NIPAAm), N, N'-methylenebisacrylamide (MBAm), 2,2-dimethoxy-2-phenylacetophenone (DMPA), 3-(trichlorosilyl)propyl methacrylate (TPM), acetone, heptane, and hexane were all obtained from Sigma-Aldrich.

4.2.2 Instruments

The polymer nanocomposites were mixed by using an ARE-310 planetary centrifugal THINKY mixer. It is important to avoid any solvent evaporation during mixing. Therefore, PARAFILM® was used to cover the disposable mixing cups, and the mixer was used in 'Step' mode in order to avoid losing solvent by degassing. The solution was mixed at 2000 rpm for 2 minutes.

The fabrication of the SU-8 master mold was performed through UV-lithography with the use of a Laurell WS-650MZ-23NPP spin coater, an EVG®620 automated mask aligner system, and a Karl Suss 100S optical power meter.

The sample images were taken with an AmScope SM-4TY-FRL professional trinocular stereo zoom microscope and an AmScope MU1400 14MP microscope digital camera.

X-ray diffraction (XRD) measurements, to determine crystalline structure of the nanoparticles, were carried out in a Bruker ZXS X-ray diffractometer model D8 Focus. The x-

ray radiation is Cu-kα (λ=1.5406 Å) and the detector is a 1D LynxEye Detector with a special resolution of 75 μm.

A FEI Morgagni 268 transmission electron microscope (TEM), operating at 60 kV, was used to characterize the size, crystallinity, and homogeneity of the nanoparticles.

The magnetic properties were measured using a physical property measurement system (PPMS) by Quantum Design, with a vibrating sample magnetometer (VSM) option. Hysteresis loops were measured at 300 K in applied fields up to 50 kOe.

The heating efficiency of the nanoparticles was evaluated under an AC magnetic field (0–800 Oe) at mid-range frequencies 310 kHz, using calorimetric methods with a 4.2 kW EASYHEAT Li3542 precision induction heating system, by Ambrell, UK. The measurements were performed in water with a concentration of nanoparticles of 2 mg/ml. Furthermore, the surface antifouling experiments were performed with an eight-turn helical coil with a diameter of 25 mm and a length of 43 mm. Water circulation in the coil was provided to maintain the coil at ambient temperature. The surface attached magnetic polymer nanocomposite samples were placed at the center of the coil and an alternating magnetic field was applied at 310 kHz with a calculated magnetic field of 800 Oe.

An Agilent U5855A TrueIR Thermal Imager was used to obtain the IR thermal images. The IR images were taken at different zoom modes, including digital zooms of 80x and 160x magnification.

4.2.3 SU-8 Master Mold Fabrication

SU-8 is a widely used epoxy-based negative photoresist ideal for UV lithography defined micro structures. A SU-8 master mold was fabricated to mold the PDMS stamp. In order to get a good adhesion between the SU-8 and the Si wafer needs to be clean. Thus, a 4-inch wafer was

cleaned with a piranha wet etchant using H_2SO_4 and H_2O_2 followed by a deionized water rinse. The wafer was placed on a hot plate at 110°C for 15 minutes for a dehydration bake to remove any water that may reduce adhesion. OmniCoat, an adhesion promoter, was spin coated on the wafer at 3000 rpm for 30 seconds, followed by a bake at 200°C for 1 minute. The SU-8 was then dispensed on the Si wafer and spin coated with the recipe shown in Table 1. As an attempt to remove any edge bead after spin coating, the spin speed was raised to 6000 rpm for 5 seconds. The Si wafer was then placed on a hot plate at 95°C for 6 minutes as a pre-exposure (soft) bake. The SU-8 was exposed to a 365 nm UV light with an intensity of 8 mW/cm^2 for 20 seconds. This was followed by a post-exposure bake at 100°C for 15 minutes. This bake facilitates the polymerization process. Lastly, the wafer is placed in SU-8 developer for 4 minutes to remove any unexposed photoresist, followed by a deionized water rinse and air dried. Figure 4.1 shows an optical image of the fabricated SU-8 master mold with parallel microbeams.

Table 4.1: SU-8 spin coating program

Step	Spin Rate (rpm)	Time (s)	Acceleration (rpm/s)
1	500	10	100
2	4500	30	300
3	6000	5	1200
4	2000	10	300

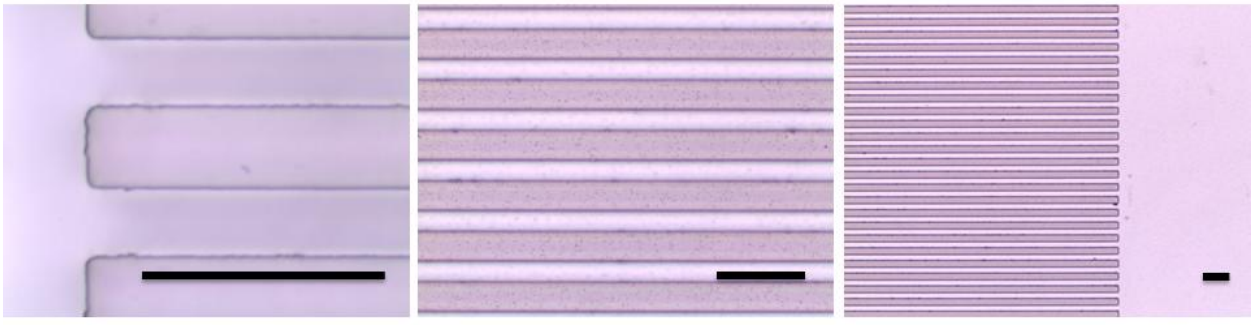

(a) (b) (c)

Figure 4.1: Optical images of the fabricated SU-8 master mold microbeams at (a) 300X, (b) 100X, and (c) 80X magnification. The measurement bar represents a standard length of 20 µm.

4.2.4 Preparation of Magnetic Hydrogel Microstructures

Microfabricated PNIPAAm Fe_3O_4 polymer nanocomposite structures were surface attached on glass coverslips. The microstructures were constructed with microbeams of 20 μm (width) x 25 μm (height) x 5 mm (length) dimensions. Additionally, the structures were surface attached on 25 mm diameter glass coverslips. The microbeams were fabricated as previously described [247-249].

The glass coverslips were surface treated to obtain a covalent bond between the coverslips and PDMS. 3-(Trichlorosilyl)propyl methacrylate (TPM) was used as an adhesion promoter [250]. First, the coverslips were treated by O_2 plasma at 6.8W and 500 mtorr for 15 minutes. Second, the coverslips were immersed in a 1mM TPM solution in 4:1 heptane to tetrachloride. Finally, the coverslips were rinsed in hexane and deionized water. The surface treatment was carried out in a N_2 environment at room temperature.

Soft lithography via micromolding in capillaries (MIMIC) method was employed to fabricate the magnetic hydrogel made microbeams. A PDMS stamp was placed on a TPM treated coverslip with the relief facing towards the substrate. This process forms capillaries. Thereafter, a magnetic NIPAAm acetone solution containing 5 mg ml^{-1} MBAm (crosslinker), 20 mg ml^{-1} DMPA (photo initiator), 25 mg ml^{-1} Fe_3O_4 nanoparticles, and 200 mg ml^{-1} NIPAAm was used to fill the PDMS mold through capillary action. The fill rate behavior is given by the following [251]:

$$t = \frac{4\mu l^2}{r^2(\Delta P + \frac{2\gamma \cos\theta}{r})} \tag{4.1}$$

where t is the fill rate, μ is the fluid viscosity, r is the radius, ΔP is the pressure difference at the capillary openings, γ is the surface tension, θ is the contact angle, and l is the fill length. This equation is valid for horizontal and cylindrical capillaries. Once the capillaries are filled, the

magnetic NIPAAm solution is polymerized with a 365 nm ultraviolet light for 4 minutes. Lastly, the stamp is removed, leaving behind the patterned and surface-attached magnetic hydrogel microstructures.

4.2.5 Nano-Octopod Synthesis

The synthesis process of these Fe_3O_4 nano-octopods has been reported before [96]. Briefly, the particles were synthesized by high temperature reduction of iron-organometallic salt under an inert atmosphere. Oleic acid (OA) and oleylamine (OY) were used to stabilize the nanoparticles in solution and to control particle size and shape. In a typical synthesis, 4 mmol Fe(III) acetylacetonate was dissolved in 31 mmol OA and 30 mmol OY. The mixture was purged with Ar þ 5% H2 at 100° C to eliminate the free oxygen dissolved in the products. The temperature was raised up to 200° C and the mixture was stabilized for 1 h and then the temperature was further raised to 300° C at a rate of 10° C per minute and refluxed at 300° C for 2 hours. The heating source was then removed and the reaction mixture was allowed to cool down to room temperature. The particles were precipitated by adding an excess amount of ethanol followed by centrifuging. The supernatant was discarded and the resultant product was dispersed in hexane.

4.3 Results and Discussion

The surface attached magnetic hydrogel microbeams swell when exposed to water or solvent. Maximum hydrogel swelling occurs when the applied osmotic pressures by the water/solvent inside and outside the hydrogel are equal. Due to the aspect ratio of the structures and the physical constraint to a surface, when swelling, the hydrogel demonstrates physical instabilities that manifest in the form of buckling. The hydrogel microbeams are seeded with magnetite nanomaterials, which showcase magnetic hyperthermia properties in the presence of

AC magnetic fields. When this increase in temperature reaches the LCST, the hydrogel becomes hydrophobic, collapses, and the microbeam returns to its original straight physical shape. Once the magnetic field is removed, the hydrogel system cools down until reaching room temperature, which results in the hydrogel to become hydrophilic, re-swell, and return to its buckling physical shape. This non-contact physical manipulation is reversible with the presence and absence of AC magnetic fields is demonstrated in Figure 4.2.

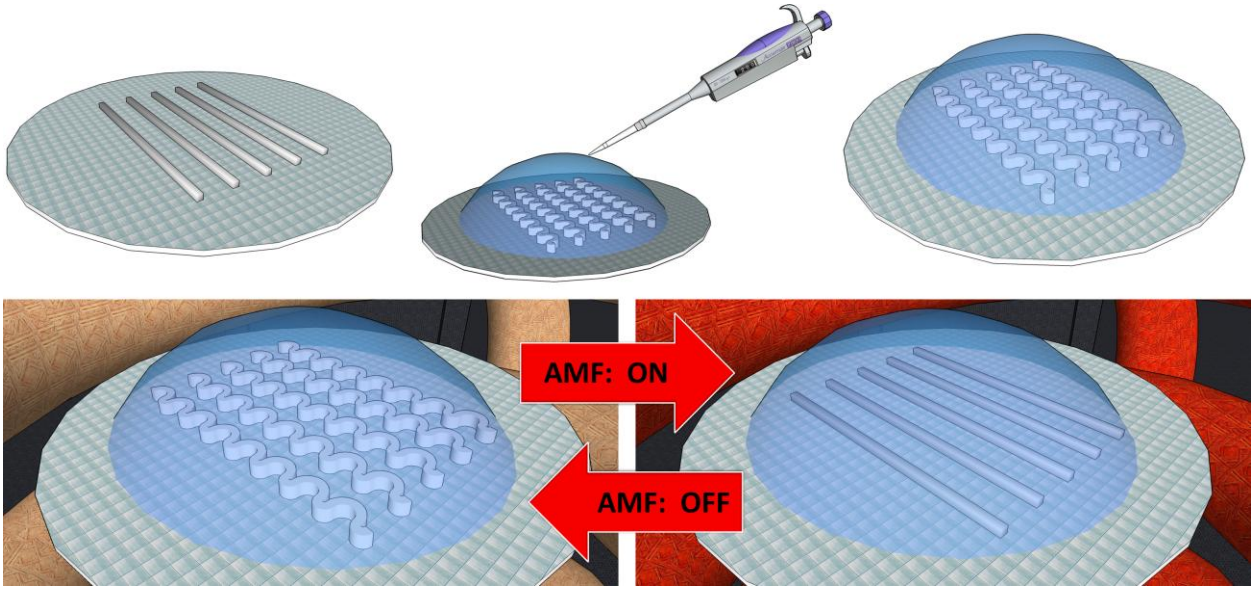

Figure 4.2: Illustration of the magnetic hydrogel buckling when exposed to water and showcasing its volumetric phase transition in the presence and absence of AC magnetic fields

Various experiments were performed to compare the heating efficiency of the commercial Fe_3O_4 nanoparticles and the in-house synthesized nano Fe_3O_4 octopods. This heating efficiency will be instrumental to the overall response of the magnetic hydrogel micro-actuators. The commercial Fe_3O_4 nanoparticles have been known for their good magnetic properties for hyperthermia applications [44]. However, due to their unique surface anisotropy, it is anticipated that synthesized Fe_3O_4 nano octopods will have better heating efficiency and

hyperthermia properties, thus, a superior micromanipulator device performance, e.g., response time.

4.3.1 Structural Characterization

As can be seen in the TEM images (Figure 4.3), the synthesized octopods present a slightly deformed characteristic cubic shape. In addition, as inferred from the inset, they also exhibit a relatively narrow size distribution despite their big dimension (D = 47.4 nm and σ = 4.6 nm), which is an especially important feature for biomedical applications. As compared to the commercial nanoparticles, it is clear that the synthesized octopods size distribution is appreciably better.

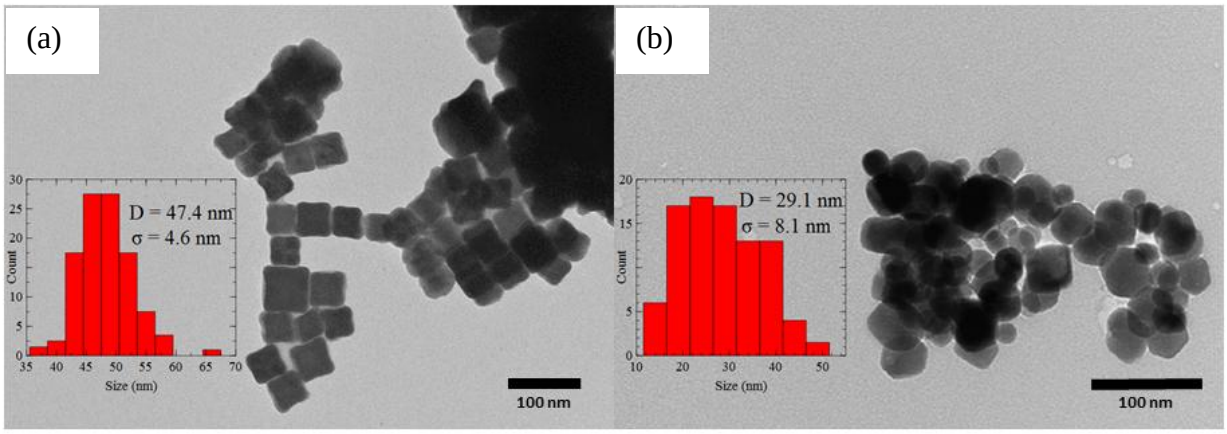

Figure 4.3: TEM image of magnetic octopods (a); and commercially available iron oxide nanoparticles (b).

The nano-octopods and commercial nanoparticles have been characterized by using XRD, as shown in Figure 4.4. Several well defined and narrow peaks have been obtained in the diffractogram, which match well with those from the JCPDS card 75-1609 of magnetite, indicating that the octopods and the commercially available iron oxide nanoparticles are mainly composed of magnetite and/or maghemite.

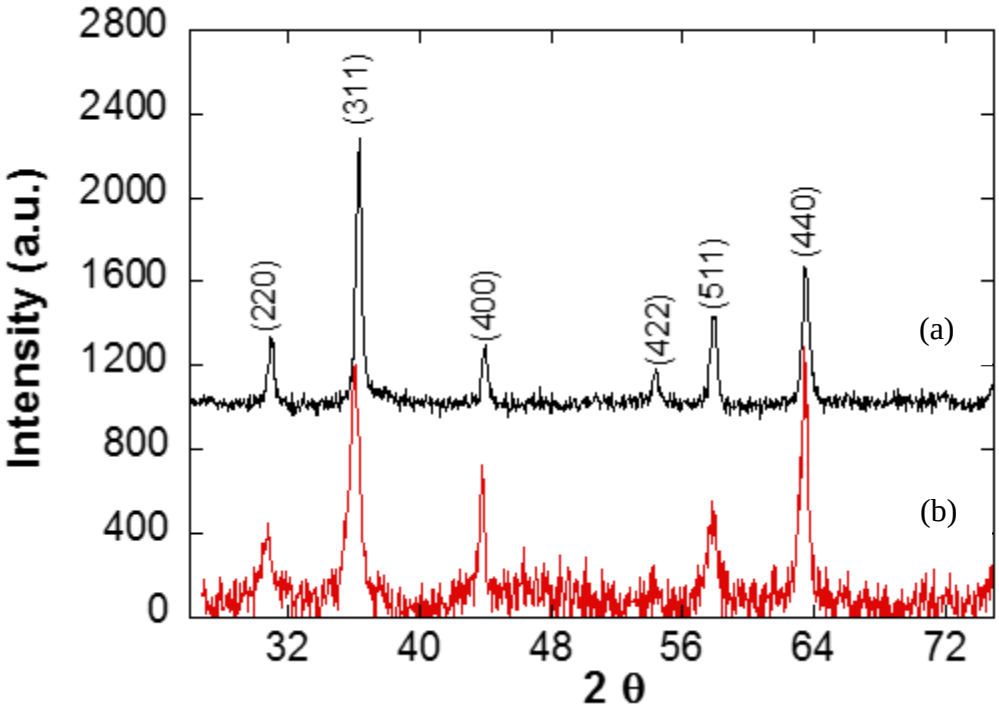

Figure 4.4: XRD of commercially available (a) and octopod (b) iron oxide nanoparticles with Miller indices indicating cubic spinel structure for both nanoparticle systems.

4.3.2 Magnetic Measurements

Figure 4.4 presents the DC hysteresis loops measured at room temperature for the nanoparticles, showing a squared shape in both cases, with saturation values close to the bulk value of magnetite (92 emu/g). This again confirms that the nano-octopods are mainly composed of Fe_3O_4. However, the saturation and coercive field values of the octopods (84 emu/g and 106 Oe) are higher than those of the commercially available nanoparticles (78 emu/g and 85 Oe), suggesting better heating properties for the former ones, since the hysteresis loop area, directly related to the SAR, is larger in this case [252].

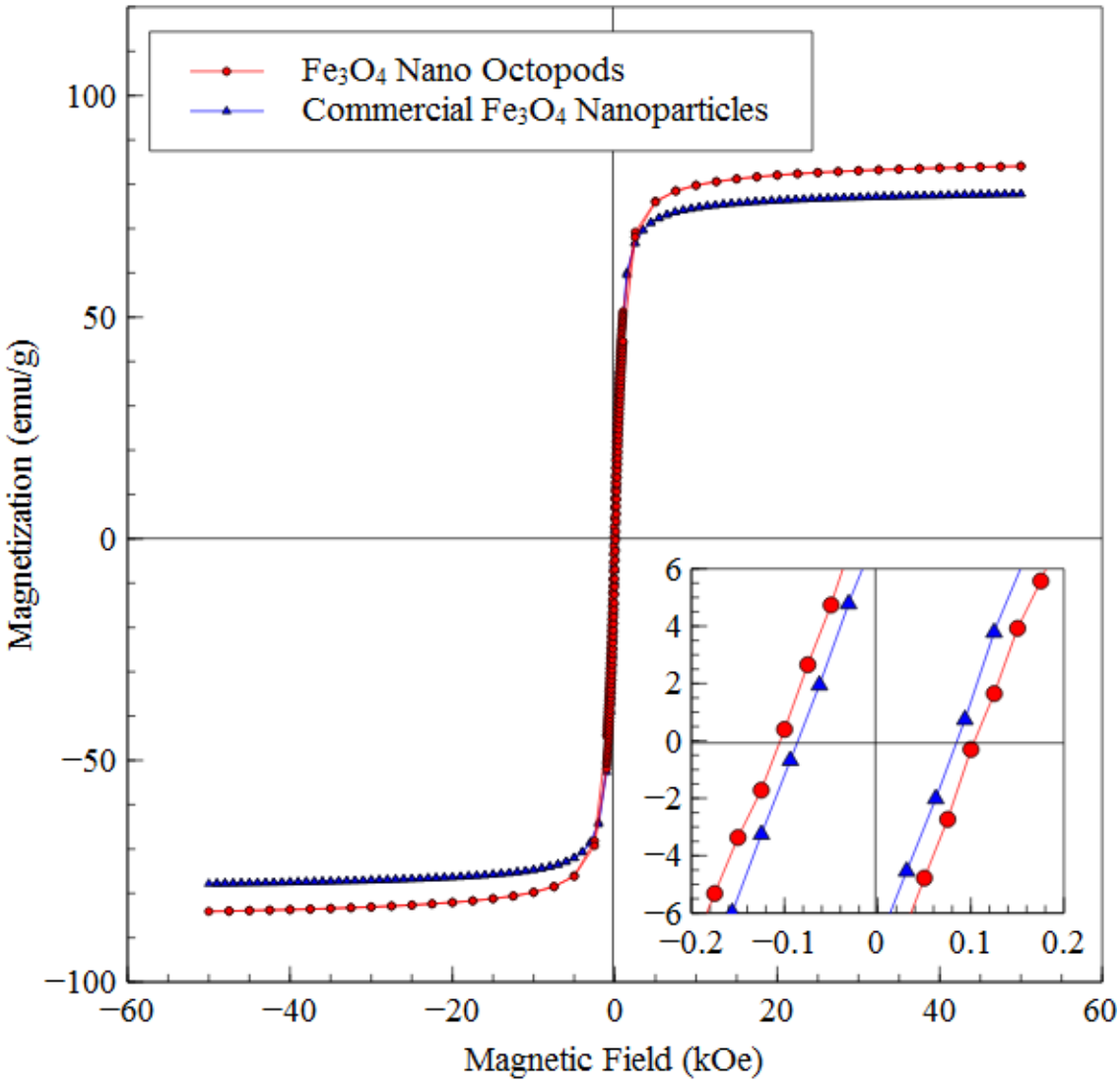

Figure 4.5: Room temperature hysteresis loops measured for both the octopods and commercial nanoparticles

4.3.3 Hyperthermia Measurements

Figure 4.6 (a) presents the heating characteristics for the nanoparticles as a function of the applied field (200-800 Oe). As can be seen, the heating rate is greater for the octopods than that of the commercial particles. This can be more easily derived from the SAR curves. The SAR can be estimated from the initial slope of the heating curves as defined by:

$$SAR = \frac{\Delta T}{\Delta t} \times \frac{C_p}{\varphi} \tag{4.2}$$

where C_p is the heat capacity of the liquid medium (4.186 J/g°C for water), and φ is the mass of magnetic material per the mass of liquid ($2x10^{-3}$). As observed the SAR rapidly increases with increasing field, reaching values up to 550 W/g at 800 Oe. However, it can be seen that the heating efficiency of the octopods is appreciably higher than that of the commercial particles in all the range of fields analyzed.

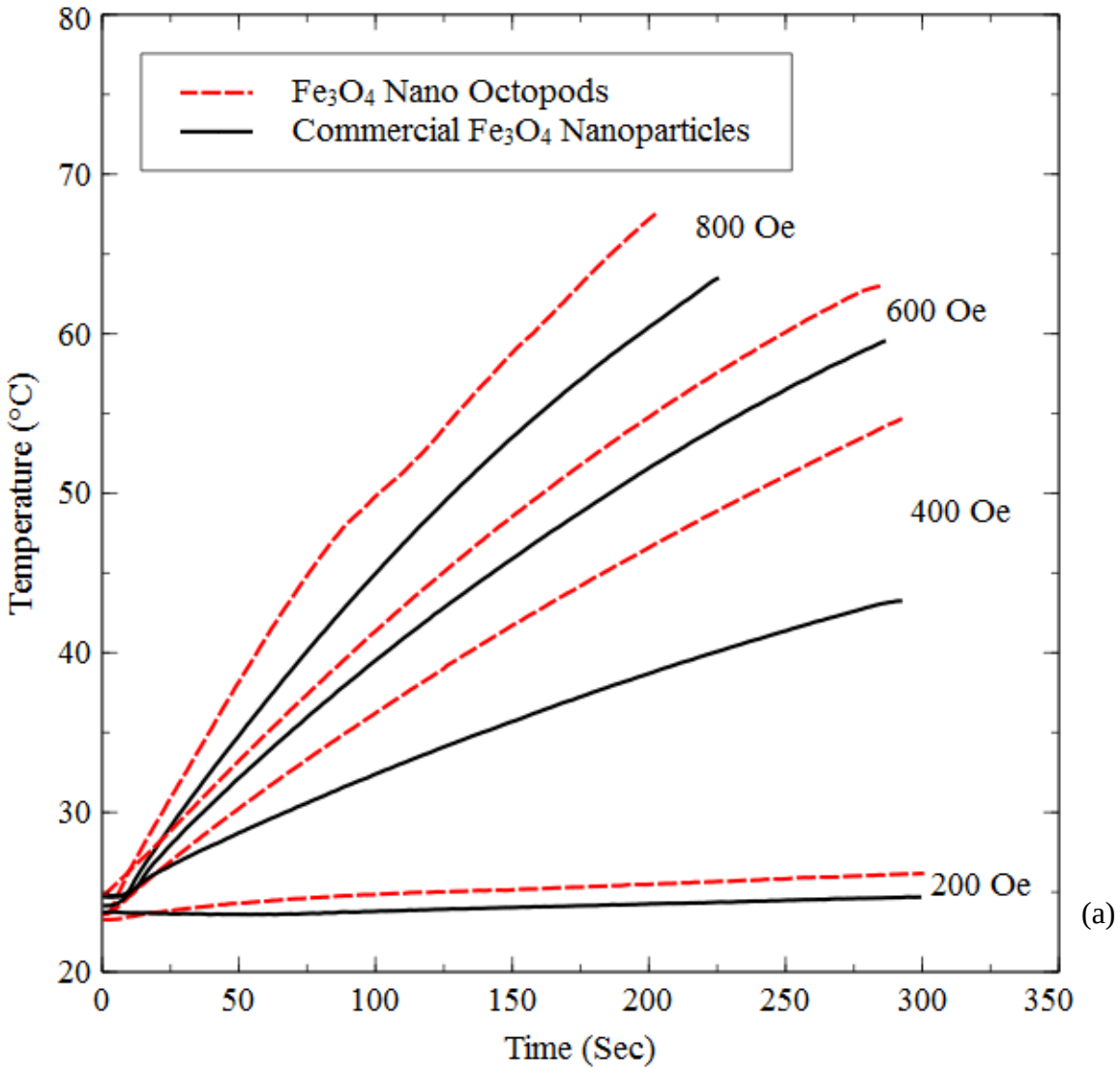

(a)

Figure 4.6: Heating curves measured at 310 kHz and different fields (200-800 Oe) (a), and SAR vs. H curves for both the commercial nanoparticles and the nano-octopods (b)

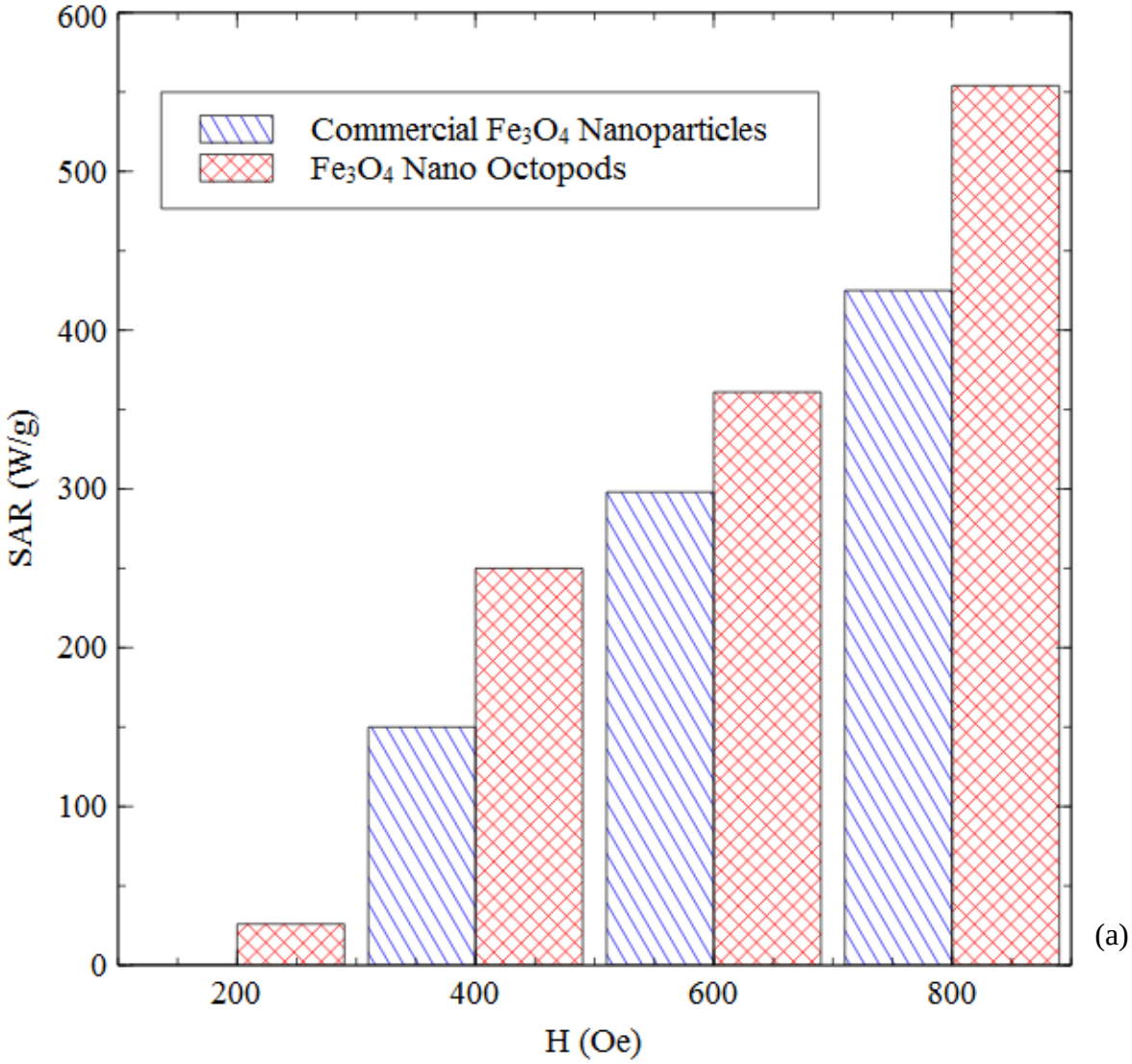

(a)

Figure 4.6: (Continued)

4.3.4 Response Time Characteristics of the Magnetic Hydrogel Microstructures

After looking at the heating response results from the hyperthermia measurements, it is clear to see that the Fe_eO_4 nano-octopods generate heat faster than the commercial Fe_eO_4 nanoparticles. However, it is important to investigate how this translates to the overall response time of the polymeric system.

Single micro-beam magnetic hydrogel samples were fabricated to study their response time under AC magnetic field actuation. Some samples were prepared by embedding the hydrogel with incorporation of 10 wt% commercial Fe_eO_4 nanoparticles, while other samples were prepared with 10 wt% Fe_eO_4 nano-octopods.

Dry hydrogel microbeams swell in volume when exposed to water or solvents. Depending on the aspect ratio of the fabricated micro-beams, the hydrogel will exhibit physical instabilities in the form of buckling due to the constraint from the surface attachment [248, 253]. The PNIPAAm based hydrogel exhibits a lower critical solution temperature (LCST) around 32°C, above which it becomes insoluble and exhibits its hydrophobic behavior. At this point, the hydrogel microbeam transitions from a buckling shape to its original straight geometry as it collapses and expels its internal water. In this system the heat is generated by the hyperthermia effect of the hydrogel magnetic nanocomposite material under an AC magnetic field. Once the AC magnetic field is removed, the system cools down to room temperature, the hydrogel microbeam becomes hydrophilic, swells, and reassumes its buckling physical state. Figure 4.7 (a) shows the magnetic hydrogel micro-beam with embedded commercial Fe_eO_4 nanoparticles gradually collapses once it is exposed to a magnetic field of 800 Oe at a frequency of 310 kHz. It is worthwhile mentioning that it took about 80 seconds for the hydrogel to reach a complete collapse state. Once the magnetic field was turned off, the hydrogel gradually reached room temperature and it went back to a buckling state after 120 seconds, as seen on Figure 4.7 (b). On the other hand, the magnetic hydrogel micro-beam embedded with Fe_eO_4 nano-octopods reached a collapsed (straight geometry) state between 20 and 30 seconds, as seen on Figure 4.8 (a). This response is more than four times faster than the hydrogel micro-beams embedded with commercial Fe_eO_4 nanoparticles. These results are consistent with the hyperthermia heating

characteristics. Figure 4.8 (b) shows that it took about 80 seconds for the hydrogel to reach its swollen and buckled state.

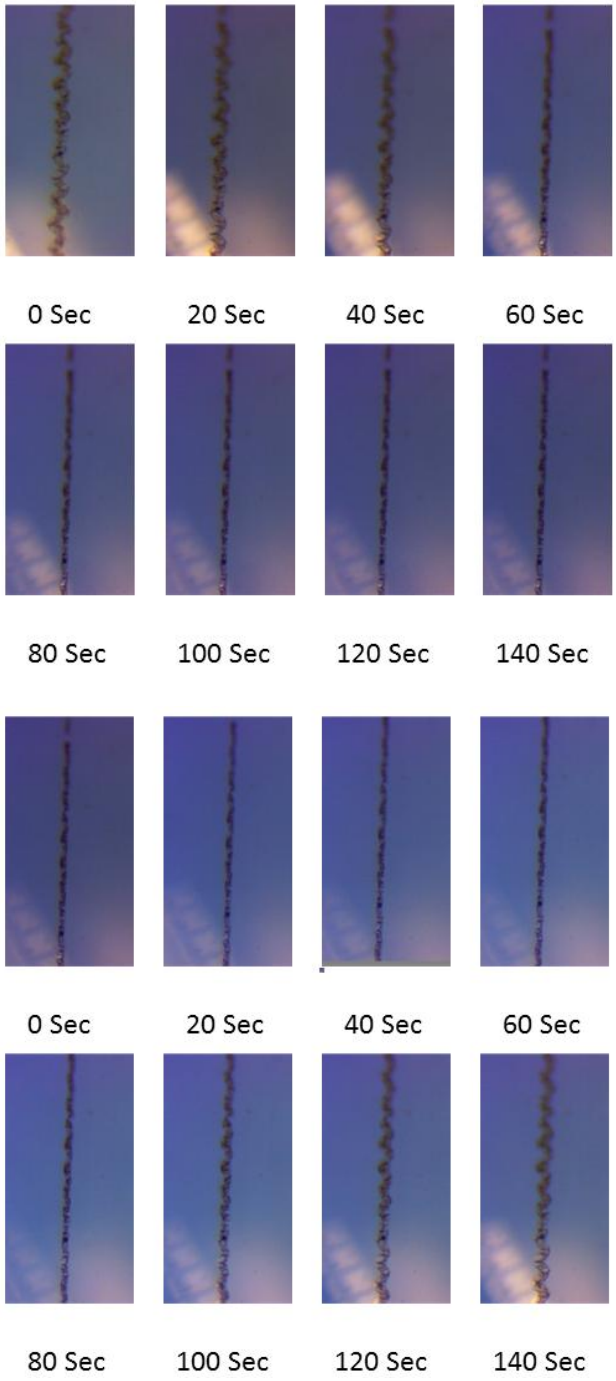

Figure 4.7: Microscopic images of a magnetic hydrogel microbeam with embedded commercial Fe_eO_4 nanoparticles showing its behavior as (a) it gradually collapses under an 800 Oe and 310 kHz magnetic field, and (b) it gradually swells at room temperature

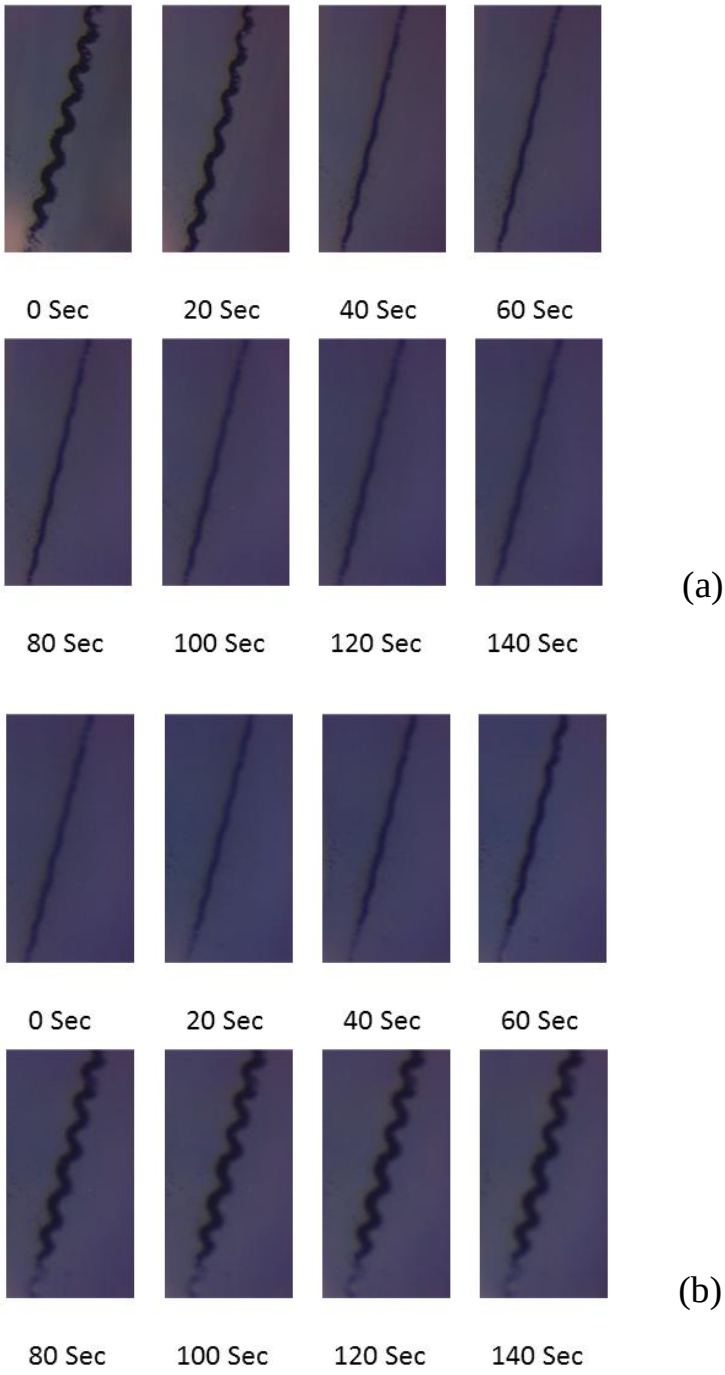

Figure 4.8: Microscopic images of a magnetic hydrogel microbeam with embedded commercial Fe_eO_4 nano-octopods showing its behavior as (a) it gradually collapses under an 800 Oe and 310 kHz magnetic field, and (b) it gradually swells at room temperature

To study the influence of the particle loading, Figure 4.9 shows the response time of different weight percent Fe_3O_4 nano-octopods concentrations (1 wt%, 5 wt%, and 10 wt%) under different magnetic field exposures (32 kA/m, 48 kA/m, and 63 kA/m).

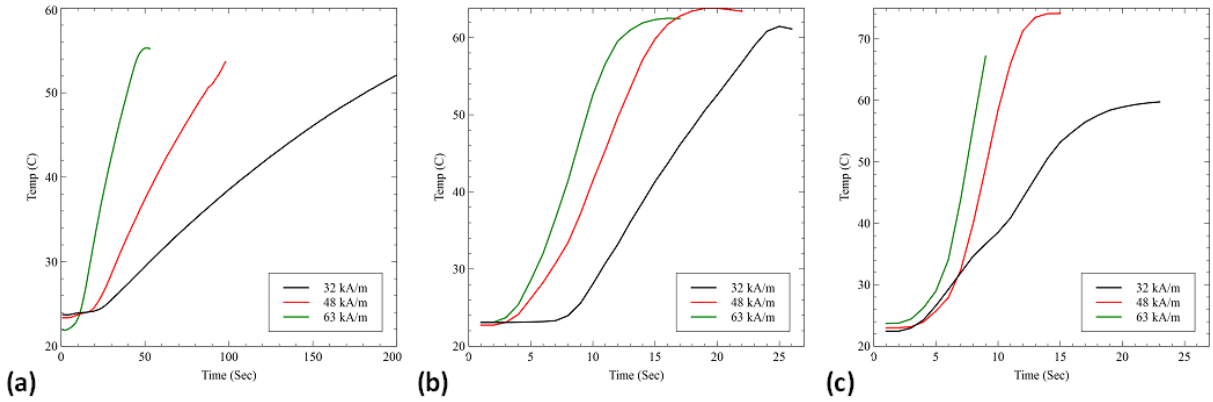

Figure 4.9: Measured response time of Fe_3O_4 nano-octopods at different weight concentration, including (a) 1 wt %, (b) 5 wt %, and (c) 10 wt %.

4.3.5 Thermal Images of the System

To further analyze the heating behavior of the magnetic hydrogel based micro-beam micro-actuators, infrared images were taken to obtain real time temperature measurements. These samples were composed of multiple 20 μm-wide beams, which are 17 μm apart from one another. The samples were placed in the middle of the coil, where they could receive the maximum amount of magnetic field. Both sets of samples were exposed to an AC magnetic field of 800 Oe at a frequency of 310 kHz. A distilled water drop was added to the samples to allow the hydrogel-beams to reach their swollen, buckled state. Figure 4.10 (a) shows the magnetic hydrogel micro-beam with embedded commercial Fe_eO_4 nanoparticles sample at room temperature, when the magnetic field is off. Figure 4.10 (b) shows the amount of heat generated when the magnetic field is turned on. Figure 4.11 (a) shows the magnetic hydrogel micro-beam with embedded Fe_eO_4 nano-octopods at room temperature, when the magnetic field off, while

Figure 4.11 (b) shows the amount of heat generated when the magnetic field is on. Once again, it can be seen that the nano-octopod filled sample generates heat more efficiently. Infrared images were taken every 20 seconds for 600 seconds to observe how the two sets of samples behaved when exposed to magnetic field over an increasing period of time. Figure 4.12 demonstrates that the temperature of the sample containing the commercial Fe_eO_4 nanoparticles saturates at about 39°C after 200 seconds. The Fe_eO_4 nano-octopod containing sample on the other hand, exhibits a continuous increase in temperature for the entire duration of the measurement, until reaching 60°C after 550 seconds.

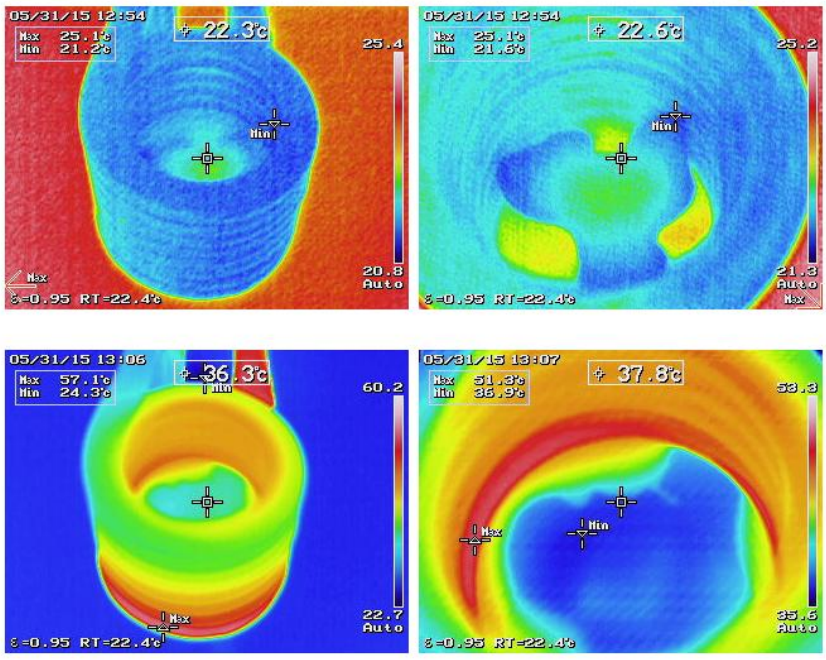

Figure 4.10: IR images of the magnetic hydrogel micro-beam with embedded commercial Fe_eO_4 nanoparticles (a) with magnetic field off and (b) with magnetic field on.

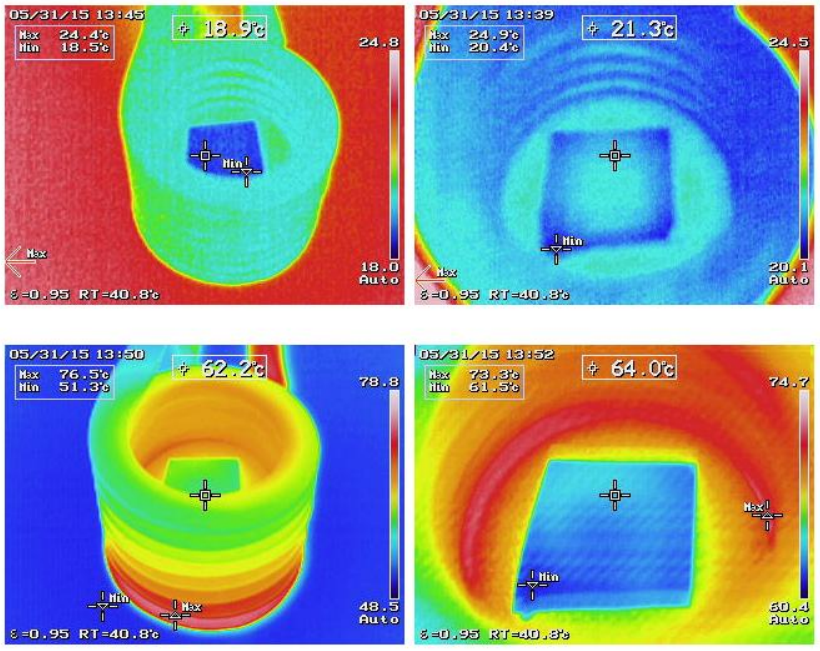

Figure 4.11: IR images of the magnetic hydrogel micro-beam with embedded Fe_eO_4 nano-octopods (a) with magnetic field off and (b) with magnetic field on

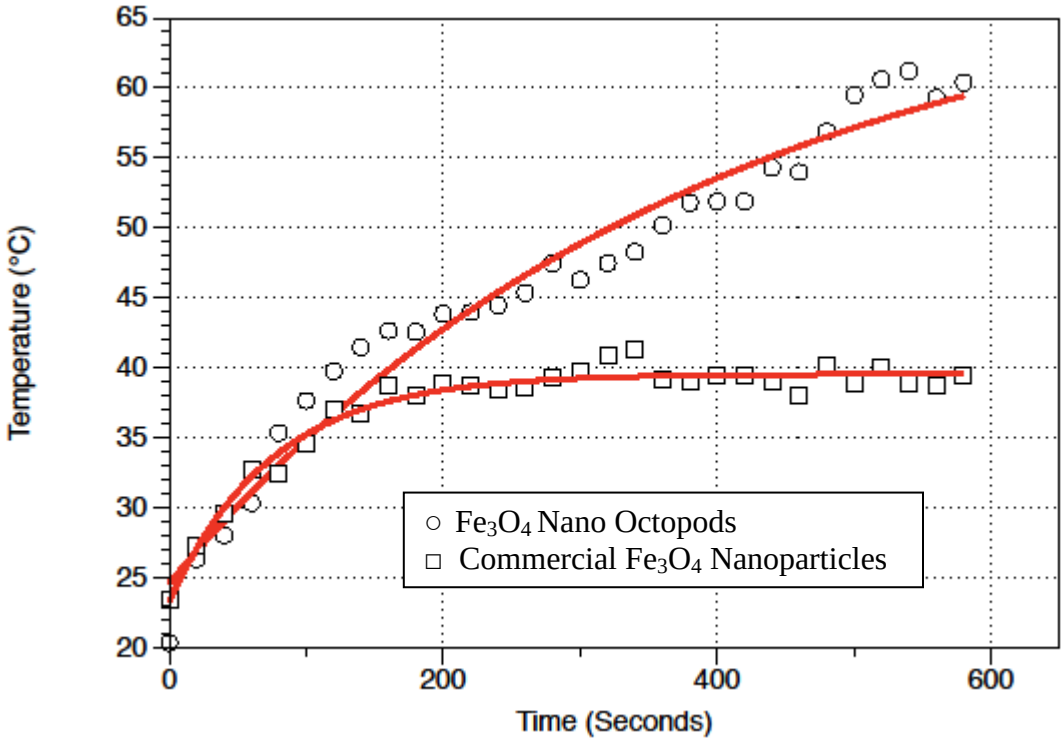

Figure 4.12: Measured sample thermal behavior when exposed to an AC magnetic field of 800 Oe at a frequency of 310 kHz

4.3.6 Buckling Wavelength Model

Mora *et al.* investigated the buckling patterns developed by the swelling of soft gels [254] They applied a linear elastic model to buckling induced on polymer strips and determined that the first stable wavelength is $\lambda = 3.256h$, where h is the height of the structure. The height of the hydrogel micro-beams at their dry state is 25 µm. According to the model, the wavelength of our buckled structures should be 81.4 µm. After measuring the wavelength of the magnetic hydrogel micro-beams, the sample with the commercial Fe_eO_4 nanoparticles fits the model perfectly. On the other hand, the sample with the Fe_eO_4 nano-octopods is slightly off. This may be due to the fact that the nano-octopods are more ferromagnetic and they tend to agglomerate among each other. Figure 4.13 shows images with the measured wavelengths.

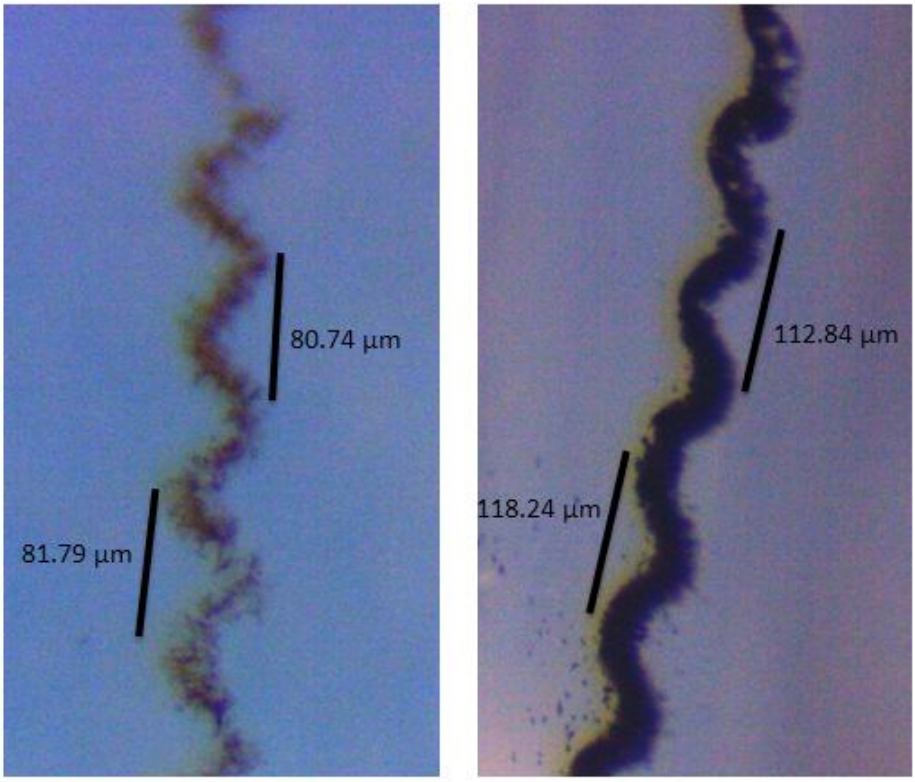

(a) (b)

Figure 4.13: Zoom-in top-view microscopic images of hydrogel micro-beam showing the wavelength for (a) the commercial Fe_eO_4 nanoparticle filled sample and (b) the Fe_eO_4 nano-octopod filled sample

4.3.7 Antifouling Surfaces

In order to demonstrate the antifouling capabilities of this magnetic hydrogel system, 50 μm polystyrene beads were exposed to the sample surfaces to mimic undesired pollutants. Figure 4.14 demonstrate a sequence of the 50 μm particles moving along the magnetic hydrogel micro-beam surface as PNIPAAm collapses when surpassing the LCST of 32°C. Each image was taken 10 seconds apart.

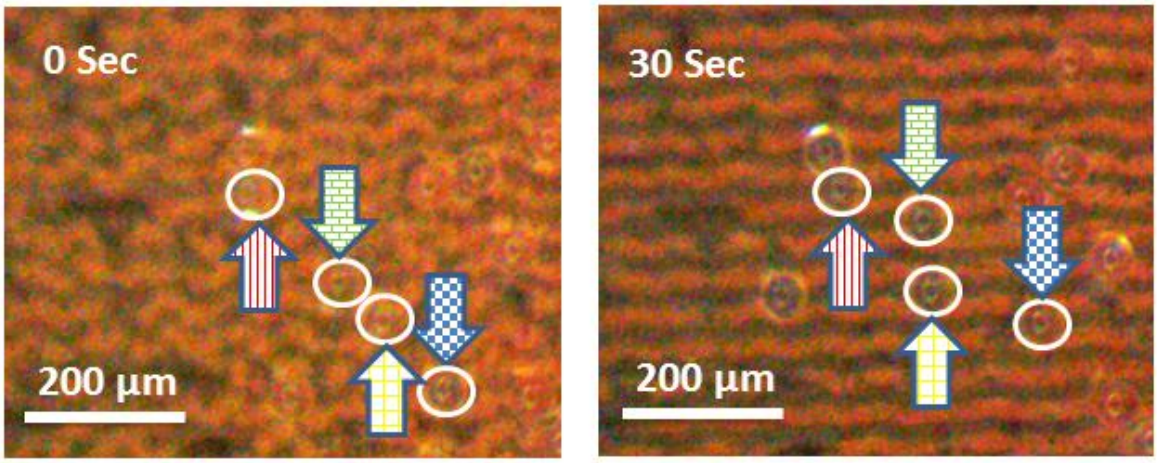

Figure 4.14: Sequential images of 50μm beads moving on magnetic hydrogel antifouling surfaces. Images were taken before AC magnetic field exposure and after 30 seconds of AC magnetic field exposure.

4.4 Conclusions

The miniaturization of medical lab-on-a-chip devices will be the next scientific breakthrough. However, biofouling remains to be a significant hurdle for the commercialization of biosensors and microfluidic devices. It is of outermost importance for medical devices to be reliable by mitigating the biofouling issue. Thus the fouling hindrance needs to be addressed.

A novel approach for fabricating antifouling surfaces has been presented. Furthermore, Fe_eO_4 nano-octopods have been synthesized, which have exhibited better hyperthermia heating efficiency than the commercial Fe_eO_4 nanoparticles largely due to their surface anisotropy.

CHAPTER 5: DEVELOPMENT OF MOLD COMPOUNDS WITH ULTRA-LOW COEFFICIENT OF THERMAL EXPANSION AND HIGH GLASS TRANSITION TEMPERATURE FOR FAN-OUT WAFER LEVEL PACKAGING (FOWLP)

The future of Lab-on-a-Chip (LOC) devices is promising for integration with CMOS technology for development of biomedical hand-held device incorporation [255-258]. Coefficient of thermal expansion (CTE) mismatch is a critical problem for multi-chip interconnecting technology. In order for this promising technology to come to fruition, the matching of CTE between the underfill materials has to be addressed. This chapter will focus on the reduction of CTEs for underfill materials down to ultra-low values.

5.1 Notice to Reader

This chapter was published in IEEE Transactions on Components, Packaging and Manufacturing Technology. Permission is included in Appendix A.

5.2 Abstract

Coefficient of thermal expansion (CTE) mismatch between an underfill encapsulant material and integrated circuit chips mounted on a substrate is the major reason for device failure in a Fan-Out Wafer Level Packaging (FOWLP) assembly. In this study, a variety of moldable polymer composite systems with evenly dispersed dielectric nano- or microparticles and minimal cure shrinkage for FOWLP assemblies have been investigated. Most importantly, a low CTE of 6.6 ppm/˚C and a high glass transition temperature (T_g) above 300 °C were achieved through a processing methodology that exhibits fairly good repeatability. A special surfactant treatment of

the particle surfaces has played a crucial role in further enhancing the thermomechanical properties, yield, and repeatability of the composite material.

5.3 Introduction

Fan-Out Wafer Level Packaging (FOWLP) technology was developed as an advancement of the standard Wafer-Level Packaging (WLP) in order to provide a better solution for semiconductor devices that require higher level of integration and a larger number of external contacts. Infineon introduced the embedded WLP in April 2009, which was the first high volume FOWLP production [259, 260]. FOWLP technology is anticipated to play a crucial role to meet the current and evolving needs of high performance and miniaturization. Commercial applications such as telecommunications require FOWLP to develop high-speed and high-frequency devices by shortening interconnect length, whereas military applications employ FOWLP mainly to develop small size systems with unprecedented performance by allowing IC chips of mixed technologies to be tightly integrated together. FOWLP modules are often comprised of multiple IC dies stacked along the z-axis, resulting in great improvement in compactness, manufacturing yield and integration level of different IC technologies. This allows for shorter interconnects and lower parasitic capacitance thus resulting in up to 3X faster processing speed, a 7X decrease in area [261], a reduction of system power consumption by as much as 30 % [262, 263] and greater signal integrity.

Thermomechanical stability of FOWLP technology has been a key source of reliability issues. Thermally induced stress build-up in electronic packages is mainly due to discrepancies in the coefficient of thermal expansion (CTE) between the packaging materials involved [264]. Failure mechanisms of microelectronic packaging due to CTE mismatch include fractures, delamination, or cracks through the device [265, 266].

The CTE is a physical property that specifies the extent to which a material expands in response to a temperature increase. Moreover, the CTE is an important parameter for encapsulants in electronic packaging systems. For microelectronic applications the reduction of encapsulant CTE to better match that of the carrier substrate is instrumental for obtaining dimensional stability. For that reason, composite materials need to be developed and tailored for different packaging systems. Composite materials are defined in ASTM D 3878-95C as a substance consisting of two or more materials, insoluble in one another, which are combined to form a useful engineering material possessing certain properties not possessed by the constituents. Composite materials fall into four categories, polymer-matrix composites (PMCs), metal-matrix composites (MMCs), ceramic-matrix composites (CMCs), and carbon/carbon composites (CCCs) [267].

Physical properties of polymer materials such as thermal, mechanical, and electrical properties can be greatly improved by the addition of inorganic additives [268, 269]. Prior studies have shown that composite materials reinforced by dispersion of silica particles are known to reduce the overall CTE of the system [270-273]. However, these traditional epoxy molding compounds typically have a CTE higher than 20 ppm/°C, which is significantly higher than the typical CTE of IC chips.

The present work has been focused on the development of thermoset polymer-matrix composites with monodispersed inorganic particles to tailor the effective CTE for compression/transfer molding in low expansion applications. Initially, Duralco^{TM} 4460, a low viscosity epoxy material, was used to demonstrate that loading a polymer resin with SiO_2 nanoparticles can effectively reduce the CTE of the material. However, in order to obtain even lower CTEs, micrometer-sized SiO_2 fillers with reduced surface-to-volume ratio have been

employed. This was demonstrated by using the AI Technology MC7883-UF, a material with a low initial CTE and low cure shrinkage. The obtained CTE results were equal to or slightly better than a commercially available encapsulant material from Hitachi (i.e., CEL-C-2921K1), which has a measured CTE of 11.3 ppm/°C at 25 °C. Finally, a discussion will be presented on how this newly developed composite material can be adopted and utilized through a special compression/transfer molding type process for a pre-existing FOWLP technology developed by Draper Laboratory.

5.4 Experimental Section

5.4.1 Materials

In this work, several types of SiO_2 particles with sizes ranging from 20 nm to 50 μm and different morphology have been employed as reinforcements for the purpose of reducing the effective thermal expansion of the composite materials. 20-30 nm solid SiO_2 nanoparticles were acquired from the Nanomaterial Store. 1 μm uniformly-sized SiO_2 microspheres were obtained from Bangs Laboratories, Inc. In addition, 10 μm dry SiO_2 microparticles, 10 – 50 μm glass beads, and 0.5 – 10 μm hollow glass beads were acquired from Kisker Biotech GmbH & Co. KG. The chemical composition of the glass beads is 72 % SiO_2, 13 % Na_2O, and 9 % CaO.

Similarly, a variety of thermoset polymer materials have been exploited in this work. EPO-TEK 353ND from Epoxy Technology Inc. is a two component, heat curing epoxy suited for high temperature applications, which was mixed by a 10:1 ratio and cured at 150 °C for 1.5 hours during this work. Duralco 4460 is a two-part low viscosity epoxy acquired from Cotronics Corp., which was mixed by a 5:4 ratio and cured at 120 °C for four hours, followed by additional heat treatment at 175 °C for two hours. AIT MC7883-UF is a one part flip-chip underfill and

encapsulation material for microelectronic packaging obtained from AI Technology. This material was cured at 175 °C for three hours.

5.4.2 Instruments

A Retsch MM 400 mixer mill was used to mix and homogenize the polymer composite materials. To avoid contamination and further breakdown in particle size, 10 mm zirconium oxide mixing balls were employed to mix the weighted polymer with particles.

Thermal expansion measurements were performed with the use of a Q400 thermomechanical analyzer (TMA) system from TA Instruments, which precisely determines the CTE and glass transition temperature (T_g) of the materials under study. A flat-tipped standard expansion probe was used for these experiments and a probe force of 0.10 N was applied on all samples. The samples were measured from -25 °C up to 300 °C at a ramp of 10 °C/min. Liquid nitrogen was used with the system to measure the samples at low temperatures.

Particle size distribution and dispersion homogeneity in the composite materials was evaluated by using a Hitachi SU70 ultra high resolution Schottky field-emission scanning electron microscope (FE-SEM).

Thermal diffusivity was measured using a Linseis XFA-500 laser flash analyzer. The material was first homogenized in an agate mortar in a glove box. The homogenized material was then pressed into a cylindrical pellet (13 mm diameter) using a pneumatic press operating at approximately 18,000 lbf. The amount of material was chosen to yield a pellet with thickness of approximately 1.7 mm.

5.4.3 Sample Preparation for CTE Measurement

5.4.3.1 Direct Mixing

In prior works, different methods have been used to disperse inorganic materials into polymers, including chemical modification of the polymer matrix [274], chemical modification of the particle surface[275-277], melt processing [278, 279], solution blending [280], in situ polymerization of nanoparticles within the polymer matrix through sol-gel transformation [281], and in situ polymerization, where nanoparticles are dispersed in the monomer followed by polymerization of the mixture [282]. For the most part, these methods do not show optimal homogeneous dispersion at higher particle loading concentrations. Nevertheless, homogeneity of particle dispersion is very important when considering repeatability and thermomechanical reliability demanded by FOWLP technology. Recent work has shown that a highly homogeneous dispersion of particles can be achieved through high energy ball milling processes [283-286].

All of the polymer composites studied in this work were prepared through direct mixing by high energy ball milling (Retsch MM 400). After determining the desired amount of filler particles and host polymer matrix, the weighed materials were added to the Retsch MM 400 mixing jars. This process has led to reproducible and homogenous polymer composite materials, as evidenced by the measured CTE results and SEM images.

5.4.3.2 Mold for Sample Preparation

In order to measure the CTE of these newly developed composite materials with the Q400 TMA system, the specimens need to be prepared with a specific geometry and dimensions. Therefore, all of the samples were molded into a cylindrical pellet of 6.5 mm in height and 5 mm in diameter. This was made possible by the design and fabrication of a custom-built three-piece

mold system. This mold was constructed out of polytetrafluoroethylene (Teflon) material for trouble-free removal of the polymer composite specimens after curing. Eight 30 mm screws were used to maintain the three-piece mold together during the curing process, four in the horizontal direction and four in the vertical direction. A hydraulic press was employed to compress the mold and ensure that the polymer composites completely filled the mold cavity to facilitate the development of solid pellets after the curing process. In order to obtain an accurate CTE measurement with the TMA system, the top and bottom of the pellet samples must be completely flat. Therefore, a Dremel 4000 rotary tool was used to planarize the ends of the pellet samples. Figure 5.1 shows the mold system used for the sample preparation.

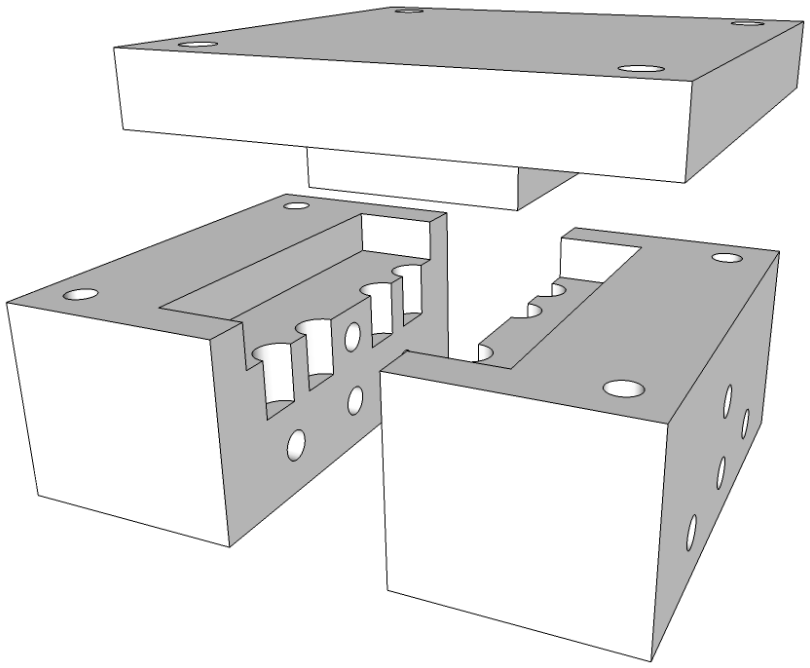

Figure 5.1: Custom-built three-piece mold for hot compression molding of specimen required for testing of the coefficient to thermal expansion using a thermomechanical analyzer.

5.4.3.3 Die Encapsulation (Injection Molding)

Figure 5.2 presents the major steps of the die encapsulation process. As shown, a compression/ transfer molding method has been adapted at the Charles Stark Draper Laboratory

for die encapsulation [287]. This encapsulation process resembles compression molding in that the encapsulant charge is placed in the mold, but it also resembles transfer molding in that the material is injected from the backside cavity to the front side cavity. This method was implemented for the present FOWLP assembly. A mold is formed using a silicon wafer with etched cavities and fill ports. A thermal release film with the active side of the die embedded into the adhesive is aligned and attached to the top side of the silicon cavity wafer. As shown in Figure 5.2(a), a charge of low CTE encapsulant is applied to a Teflon film placed beneath the cavity wafer fill ports. This step is similar to compression molding in that a charge of a specific volume of material is loaded into the fixture. The chamber is sealed and air is evacuated from the system. The ability to mold under a vacuum is a significant differentiator from standard molding operations and enables much lower injection pressures. A pressure plate forces the cavity wafer to deform an o-ring and injects encapsulant into the cavity through fill ports. This feature of the process resembles a transfer molding operation, except that the cavity wafer mold remains integral to the FOWLP. In addition to the pressure plate injection force, a positive pressure is applied behind the Teflon film to improve the ability to fill narrow spaces between die. This is followed by a temperature increase allowing the low CTE encapsulant to be semi-cured as seen in Figure 5.2(b). The encapsulant is cured under pressure and the flash on the backside of the wafer is removed using a thinning operation. The encapsulation process results in a FOWLP of die embedded in a planar wafer. Layers of interconnect are routed on top of the embedded die using alternating layers of spin-on photodielectric and patterned metal as seen in Figure 5.2(c). The entire wafer with integrated IC chips was thinned from the backside to reduce the thickness of the encapsulated wafer to reach the final device structure shown in Figure 5.2 (d).

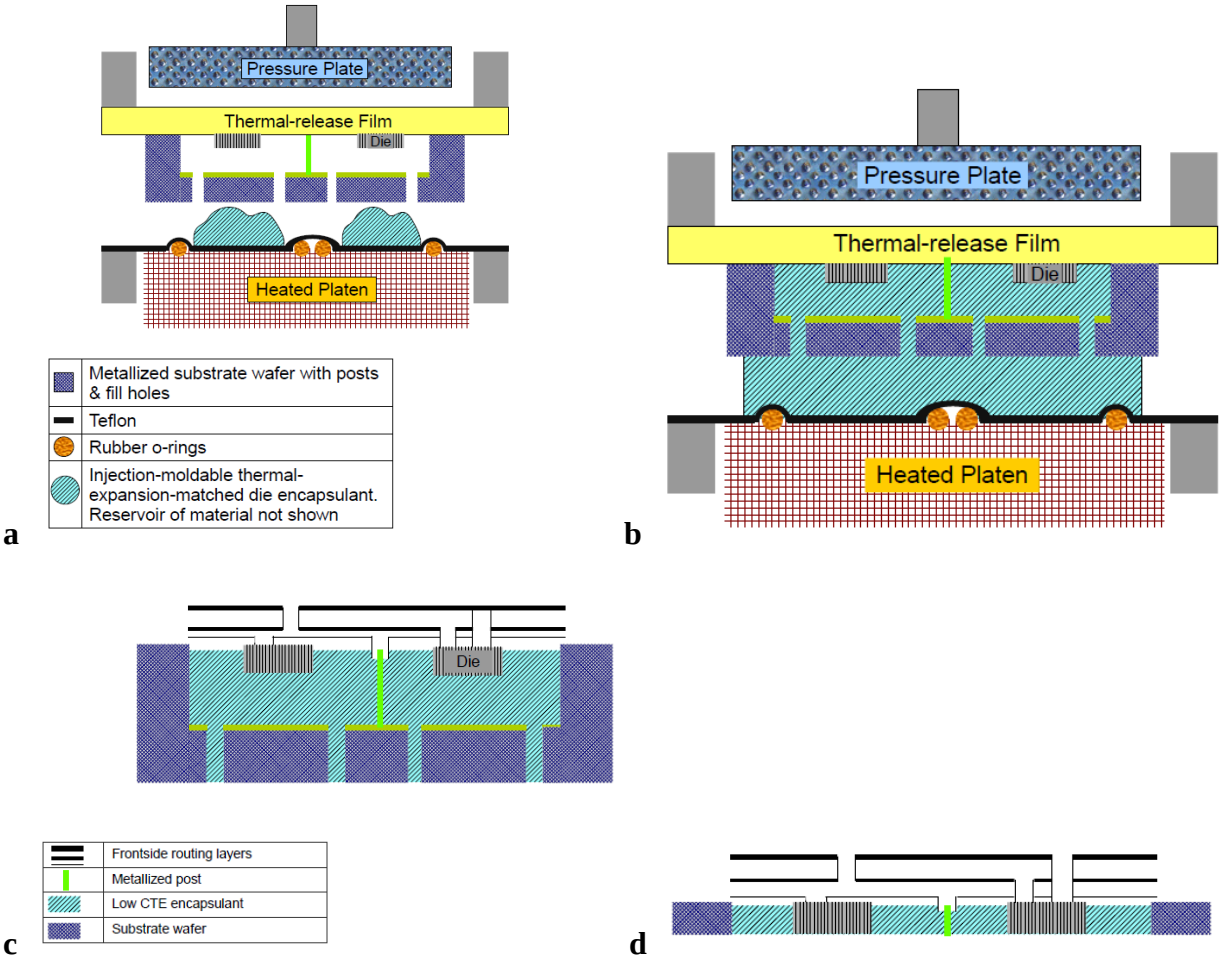

Figure 5.2: Illustration of the key steps of die encapsulation process that enables the FOWLP assemblies. (a) Die encapsulation fixture with wafer ring and deposited low CTE material; (b) Pressure and heat are applied to cure the low CTE material; (c) Fully encapsulated wafer carrier with multiple IC chips embedded underneath a multi-layer interconnects manufactured by standard IC processing techniques with spin-on dielectric layers; (d) Polished FOWLP wafer assembly with reduced thickness. Please note multi-layer interconnects were not drawn to their original scale for the purpose of illustrating the ability to carry out these processes after the die encapsulation.

5.4.3.4 Surfactant Treatment

Surfactants, or surface-active agents, are employed when there is a desire to reduce the surface tension between two liquids or a liquid and a solid. Surfactants are classified as anionic, nonionic, and cationic, this is due to the charge of their head group. Anionic surfactants are the most commonly used. Dispersant chemistry utilizes surfactants to generate stable dispersion of

solids in different media [288-292]. The semiconductor industry is constantly looking for new polymer composite materials with well-tailored thermal and thermomechanical properties for devices applications. Many of these are filler reinforced epoxy materials. The challenge when introducing fillers to epoxy materials is that the overall material viscosity increases as the amount of fillers is increased, making it difficult to apply due to lack of great flowability. The application of surfactants mitigates this issue by reducing the surface tension between the filler and the epoxy material, thus allowing a higher amount of filler to be introduced into the epoxy material to further enhance the physical properties. Lee et al. were able to obtain 57 vol% of AIN particles in epoxy by the combination of a wide particle size distribution of the AIN powder and the use of a two-layer surfactant system [293]. In this study 0.5 ml of the anionic surfactant Stepan POLYSTEP B-1 was used to modify the surface energy of particle fillers, which has shown to enhance the thermomechanical properties of the newly developed polymer composite system.

5.5 Results and Discussions

In this study, a variety of moldable polymer composite systems with evenly dispersed dielectric nano- or microparticles for FOWLP assemblies have been investigated. The Duralco^{TM} 4460 material, a two-component epoxy, was selected as a proof of concept to valid the viability to reduce the CTE by increasing the amount of SiO_2 particle fillers. The EPO-TEK 353ND material was strategically chosen due to its low CTE. Furthermore, by loading the EPO-TEK 353ND material with 64 wt% silica microparticles, a fairly low CTE of 17 ppm/°C was demonstrated. Finally, the AIT MC7883-UF material was selected mainly based on its low cure shrinkage of 0.1% specified by the manufacturer. Hence, the cure shrinkage of the modified AIT MC7883-UF material with 62 wt% loaded hollow glass beads is anticipated to be even lower.

For electronic packaging materials, cure shrinkage below 3% is considered low and ideal for close-tolerance applications [294, 295]. Additionally, the AIT MC7883-UF has a low initial CTE and a high initial glass transition temperature. Aside from an excessively low CTE of 6.6 ppm/°C, a higher glass transition temperature of 300 °C was achieved by loading the material with 62 wt% hollow glass beads.

Table 5.1: Summary of measured CTE values of three different SiO_2 filler-loaded composite materials.

Baseline Material	Max Filler Loading (wt%)	Baseline Material CTE (ppm/°C)	Filler Loaded Material CTE (ppm/°C)
Duralco™ 4460	50	90	36.8
EPO-TEK 353ND	64	54	17.0
AIT MC7883-UF	62	41.3	6.6

The CTE of polymeric materials is reduced by adding fillers that have a lower CTE than that of the organic resin. The presence of the filler lowers the concentration of the higher-CTE organic phase. To predict the overall CTE of the composite material the following governing equation is used [296]:

$$\alpha_c = \alpha_m(1 - \varphi) + \alpha_p\varphi \tag{5.1}$$

where α_c, α_m, and α_p are the CTE of the composite, polymer matrix, and particles (fillers) respectively, and φ is the volume fraction of the particle fillers. The overall composite CTE can be readily reduced by increasing the volume fraction of the fillers with respect to the resin. This effect is illustrated in Figure 5.3, where the AIT MC7883-UF material with an intrinsic CTE of 41.3 ppm/°C has been loaded with 62 wt% of hollow glass microbeads (a CTE filler) to achieve the overall CTE of 6.6 ppm/°C in this work.

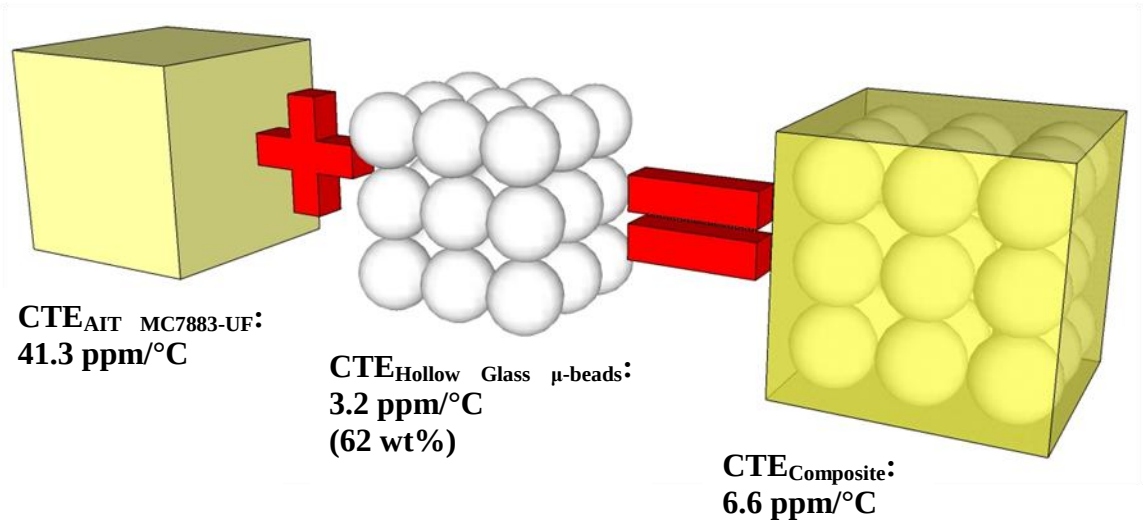

Figure 5.3: Effect of hollow glass bead fillers on the overall effective CTE of AIT MC7883-UF

With the intention to obtain some preliminary results by exploiting different polymer and filler pairs, a combination of the Duralco 4460 material and solid SiO_2 nanoparticles (20-30 nm) were studied. Duralco 4460 has a reported CTE of 54 ppm/°C. However, the temperature at which this CTE measurement was taken was not specified. Therefore, a baseline sample made of Duralco 4460 was prepared and a CTE of 90 ppm/°C was obtained at 25 °C. The material was thereafter loaded with SiO_2 nanoparticles at three different weight concentrations, such as 15, 35, and 50 wt%. It is important to mention that 50 wt% is the maximum plausible loading capacity for this combination of polymer and nanoparticles. Figure 5.4 shows that the CTE of the overall system is significantly reduced by loading the material with SiO_2 nanoparticles. The CTE of the Duralco 4460 material was reduced 59.1 % by loading the host matrix with 50 wt% SiO_2 nanoparticles. This confirms that the CTE of a material can be tailored to obtain a desired property. Although this result was promising, the obtained CTE of the nanocomposites was still too high to be amenable to the target FOWLP technology. Consequently, a different

combination of materials was necessary. Specifically, a thermoset polymer material with a low baseline CTE, a low cure shrinkage, and a high glass transition temperature is desirable

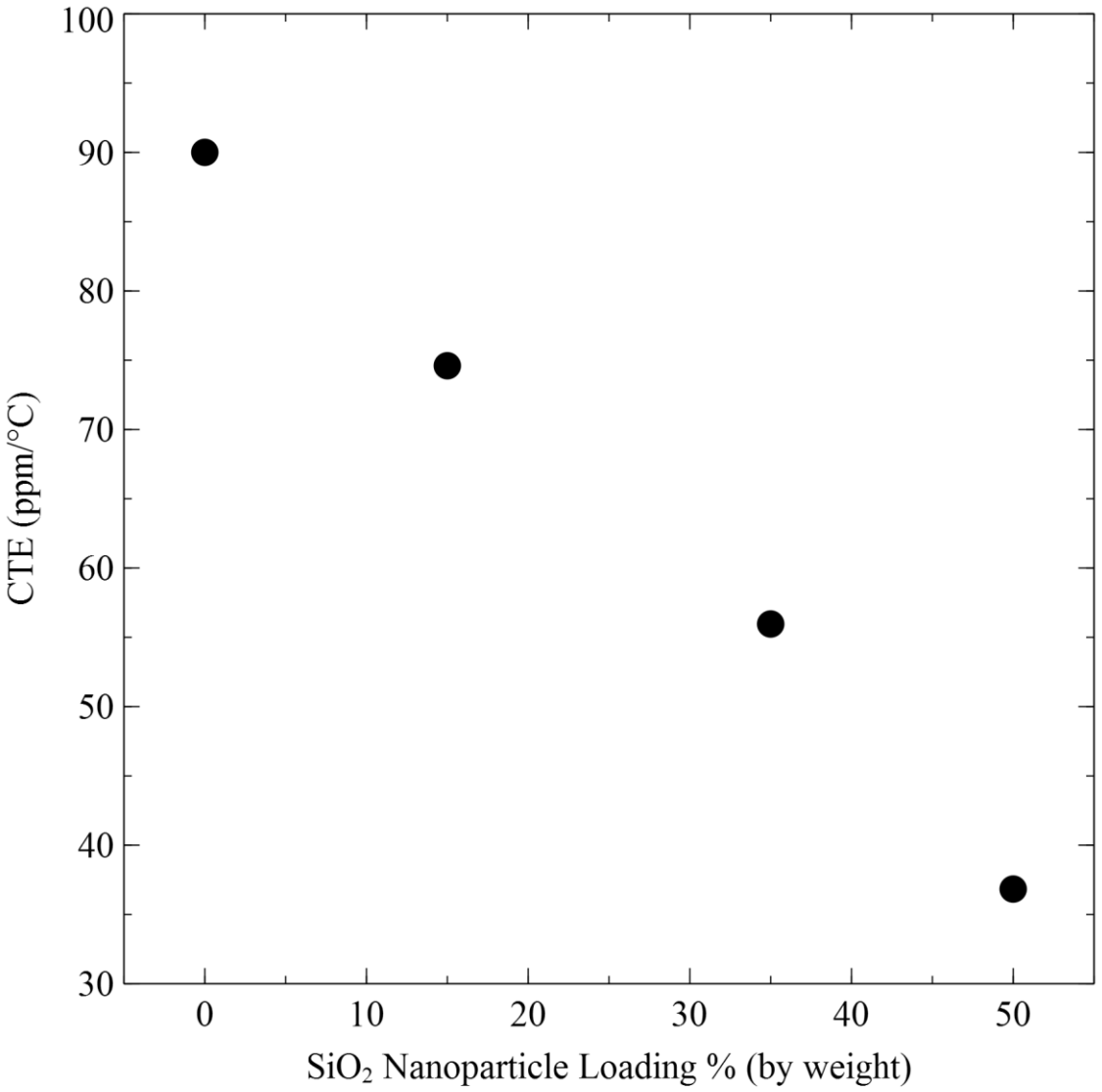

Figure 5.4: CTE reduction of Duralco 4460 through SiO_2 nanoparticle loading between 0 wt% and 50 wt%.

The flow properties of these composite materials are mainly controlled by its inherent viscosity, which are strongly influenced by the addition of fillers. Particularly, the surface area of the fillers used has a significant effect on the viscosity of the material due to the extra particle-resin interface formed. When there is a noticeable increase in the surface area of the fillers, there

is also an increase in the interactions between the particles and polymer resin, which results in a higher viscosity [297]. It was observed that the viscosity of the composite material is drastically increased when SiO_2 nanoparticle fillers are incorporated. However, the loading concentration of SiO_2 nanoparticles reached a limit rather readily where their efficacy for lowering CTE is much less pronounced. As compared to microparticles, C. Buzea et al. reported that nanoparticles have a very large surface area and a high number of particles per unit mass. One 60 μm carbon particle has a mass of 0.3 μg and a surface area of 0.01 mm^2. In order to achieve an equivalent mass, one billion 60 nm diameter carbon nanoparticles would be required, resulting in a total surface area of 11.3 mm^2 [298]. Hence, the surface area to volume ratio for identically weighted 60 nm particles is 1000 times larger than that of a 60 μm particle. For this reason micrometer-sized SiO_2 particles were employed to allow a larger amount of dispersed fillers in the composite system and therefore increasing the loading concentration limit, resulting in a lower overall CTE.

The AI Technology MC7883-UF material has a reported CTE value of 19 ppm/°C. Similar to the Duralco material, the temperature at which this measurement was taken was not reported. A sample of unfilled AI Technology MC7883-UF was prepared and a CTE of 41.3 ppm/°C was obtained at 25 °C. This material was then loaded with 62 wt% of hollow glass beads, following the aforementioned procedure. Figure 5.5 shows how the CTE of the material was reduced by 79.6 % at 25 °C and by 75 % at 150 °C. Furthermore, the glass transition temperature was increased from approximately 180 °C to more than 300 °C. As shown, a fairly low CTE of 8.41 ppm/°C at 25 °C was achieved due to the high loading concentration and strategic choice of polymer resin and fillers. Fairly similar results were also obtained with the 1 μm solid SiO_2 particles and the 10 – 50 μm solid glass beads. However, the 0.5 - 10 μm hollow glass beads were the filler particles of choice due to their small size and low cost.

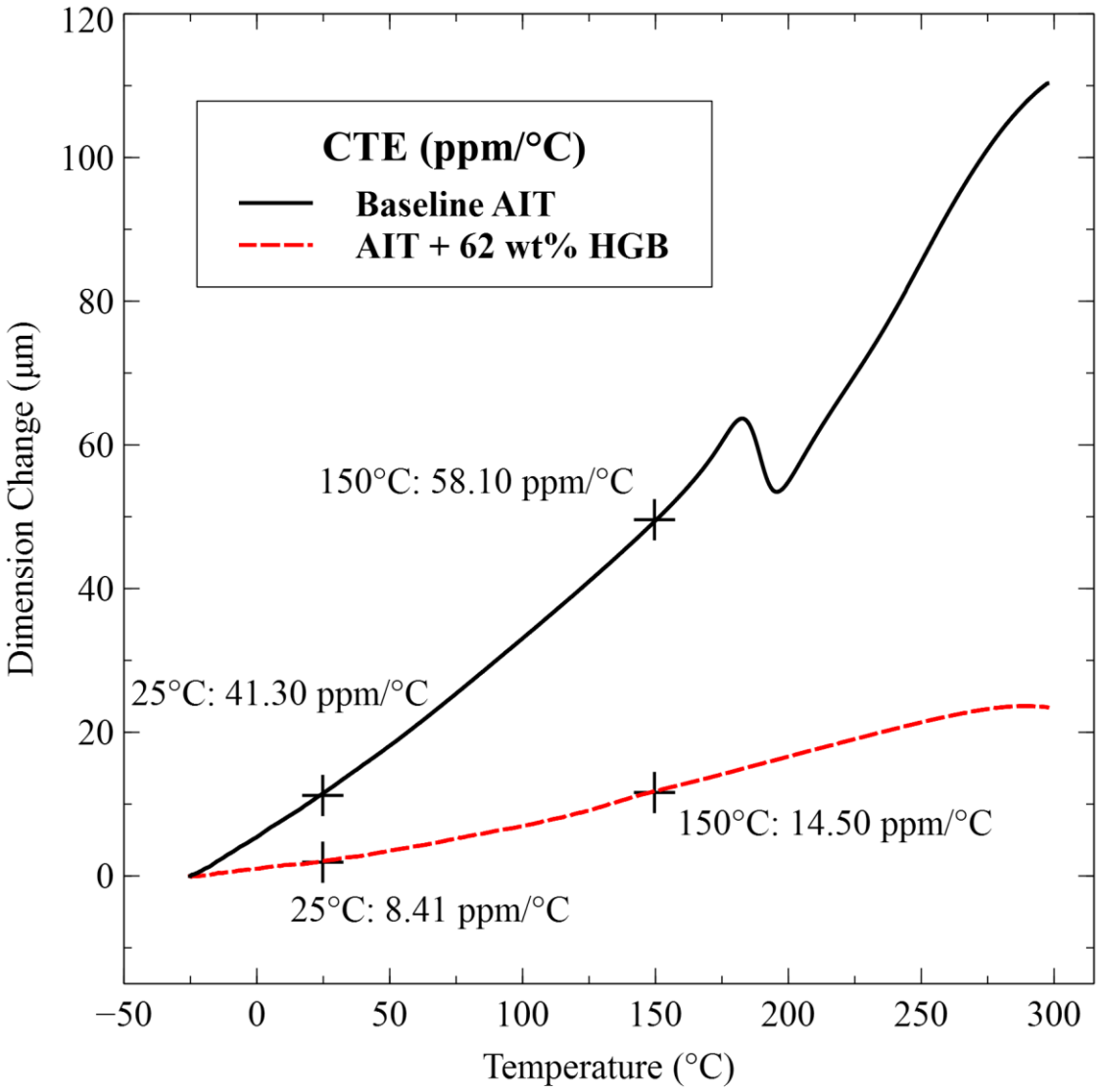

Figure 5.5: CTE reduction of AI Technology MC7883-UF material loaded with 64 wt% of 0.5 - 10 µm hollow glass beads.

The low CTE obtained with the AI Technology polymer matrix loaded with micrometer-sized hollow glass beads are fairly promising. Consequently, these results were compared to the CTE of a liquid encapsulant (i.e., the Hitachi CEL-C-2921K1 material) currently used at Draper Laboratory, which is also a highly filled epoxy material. Figure 5.6 compares the CTEs of the modified AI Technology MC7883-UF and the Hitachi CEL-C-2921K1 material. As shown, the

measured CTEs of the newly developed material based on AI Technology MC7883-UF is lower than those of the Hitachi material by 25.6 % at 25 °C and by 66.7 % at 150 °C. At high temperatures the modified AI Technology material behaves significantly better by exhibiting a much lower thermal expansion. The glass transition temperature of the Hitachi material is around 140 °C. The hollow glass beads reinforced AI Technology composite material on the other hand has a glass transition temperature greater than 300 °C.

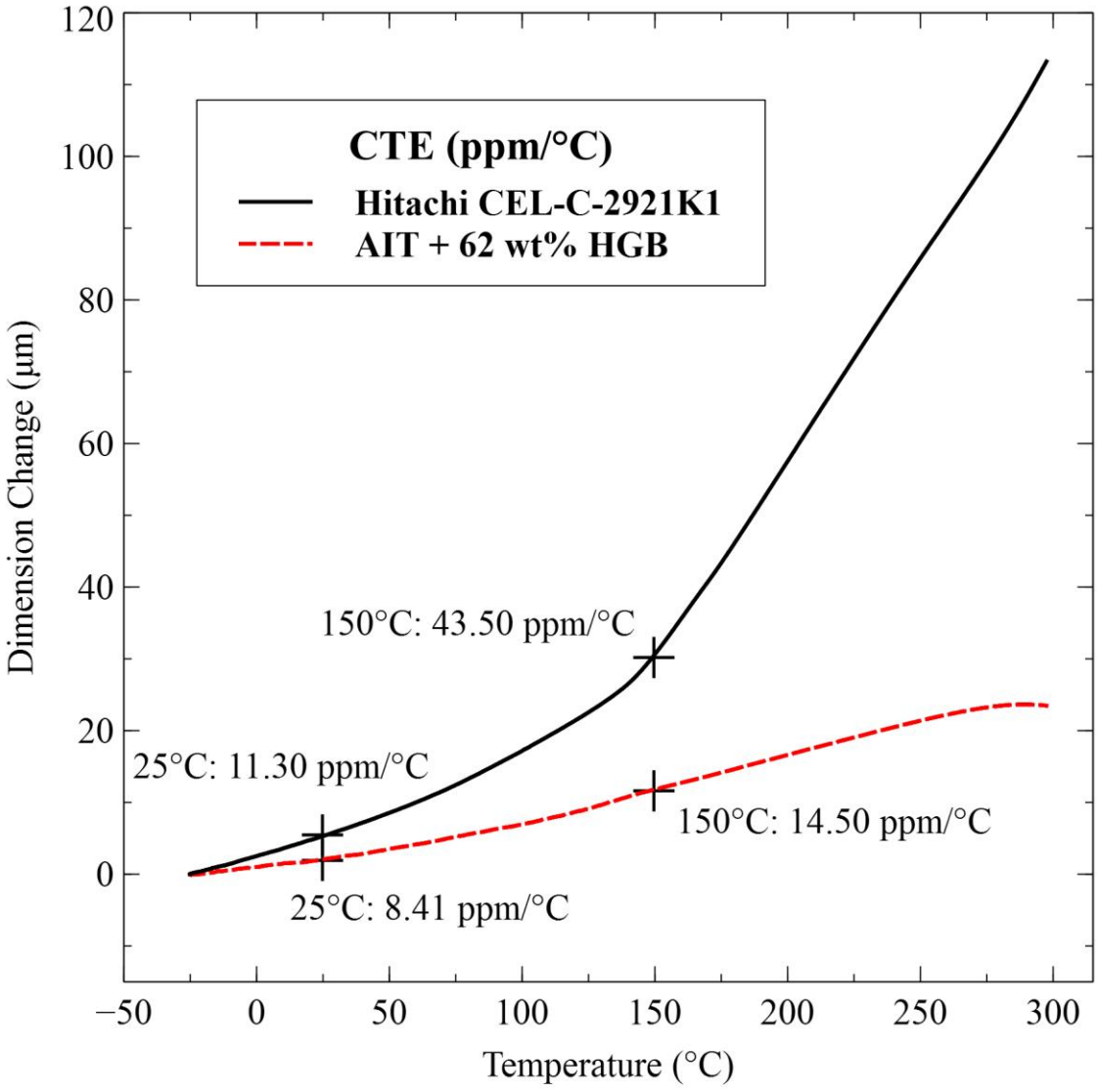

Figure 5.6: Comparison of effective CTEs between the AIT MC7883-UF loaded with 62 wt% hollow glass beads and Hitachi CEL-C-2921K1 material.

Multiple thermal diffusivity measurements were made while increasing the temperature of the sample from room temperature to approximately 100°C as shown in Figure 5.7. The baseline AIT MC7883-UF sample has exhibited a thermal diffusivity that decreases somewhat linearly with temperature, whereas the hollow glass bead filled specimen has shown greater variations and less linear behavior, potentially due to the heterogeneity of the fillers.

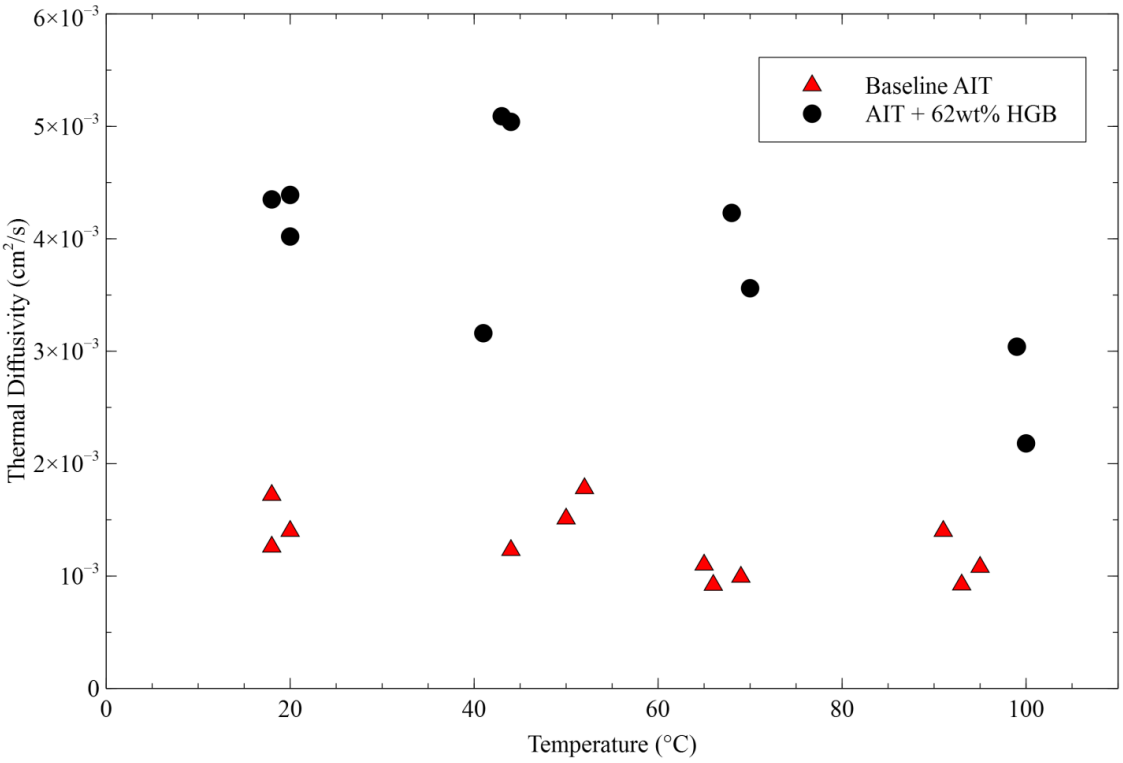

Figure 5.7: Comparison of measured thermal diffusivities between AIT MC7883-UF loaded with 62 wt% hollow glass beads and the baseline AIT MC7883-UF material.

The thermal diffusivity, α, can be related to the thermal conductivity, k, as follows:

$$\alpha = k/(\rho C_p) \tag{5.2}$$

where ρ is the density of the material and C_p is the specific heat capacity. In order to determine the thermal conductivity from the measured thermal diffusivity, it was necessary to know the density and specific heat of the samples. The density was estimated from the weight and

dimension of each cylindrical sample. The specific heat capacity of the baseline material was estimated based on the specific heat capacity of epoxy resin as obtained from the compilation of Jensen [299], while the values for the specific heat capacity and the density of the hollow glass beads was taken from the compilation of Touloukian [300]. Thus, the overall heat capacity of the hollow glass bead filled composites was calculated using a volume-weighted average of the component heat capacities [301]. Figure 5.8 presents the measured thermal conductivities for the baseline and hollow glass bead filled materials from room temperature to 100°C. It is clear that both the baseline AIT MC7883-UF and the hollow glass bead filled composites have shown a fairly consistent thermal conductivity of roughly 0.1 W/m-K over this temperature range, which is largely on par with other underfill materials [302].

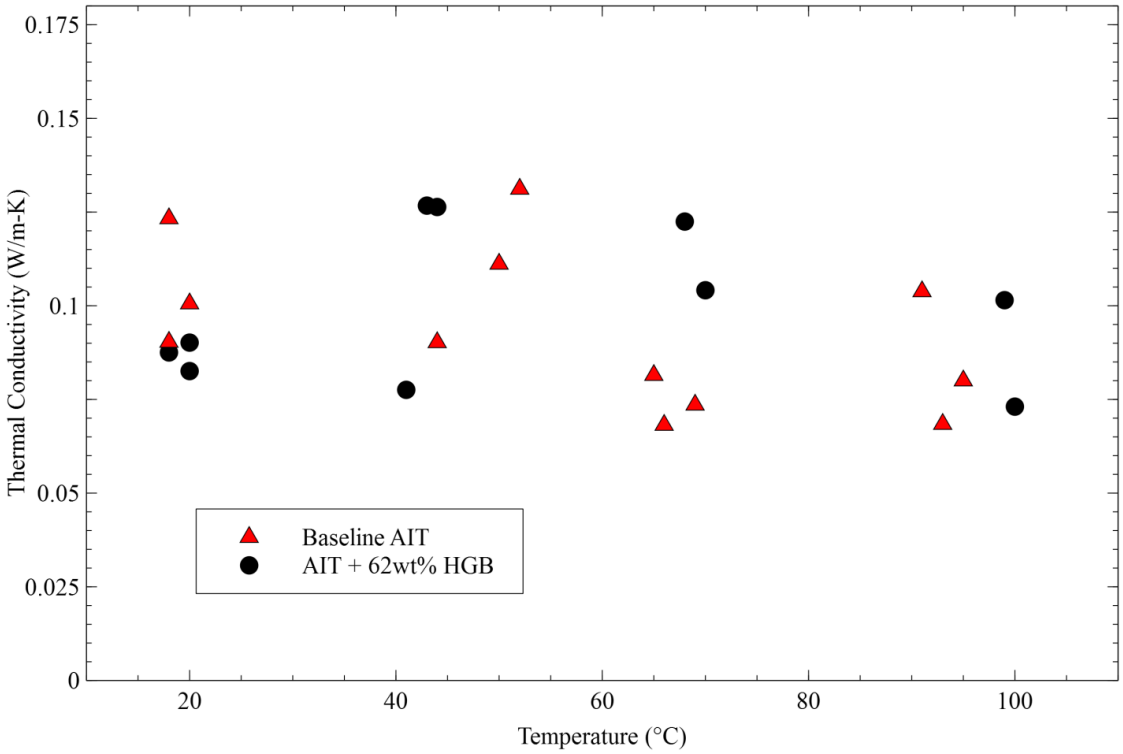

Figure 5.8: Calculated thermal conductivity based on thermal diffusivity measurements.

It is important for the mold compound to have good flow properties. As the filler loading quantity increases, the overall material viscosity also increases. This was observed when reaching the maximum 62 wt% loading concentration of hollow glass beads in the AIT MC7883-UF material. As an attempt to improve the material flow properties, 0.5 ml of Stepan POLYSTEP B-1 surfactant were added to the mixture during dispersion before molding and curing the samples. As can be seen in Figure 5.9, not only was the viscosity improved, but so did the thermomechanical properties. Three different samples were prepared and an average CTE of 6.6 ppm/°C was obtained at 25 °C and an average CTE of 12.4 ppm/°C at 150 °C. A CTE improvement of 21.5% was observed at 25 °C and 14.5% at 150 °C.

Repeatability of sample measurement is imperative to confirm good results. Figure 5.9 also shows that the three independently prepared samples share a very similar thermomechanical response under identical temperature range. In order to show consistency in the sample preparation approach, the three specimens were made from completely different mixture batches. The consistency in the results concludes that the procedure is amenable to reproducible sample preparation.

Particle size, size distribution, and dispersion homogeneity are important parameters for the pre-existing mold compound as well as newly developed materials for their adoption in the FOWLP process developed by Draper Laboratory. Hence, it is necessary to know the composition, filler size distribution and dispersion homogeneity of the composite material after the mixing and curing process. A couple of AI Technology MC7883-UF samples with 62 wt% hollow glass beads were carefully investigated under a scanning electron microscope (SEM). Figure 5.10 shows surface-view and cross-section-view SEM images of the newly developed

moldable composite material. As shown in Figure 5.10, the glass bead particles range from 1.3 µm to 9.7 µm in size.

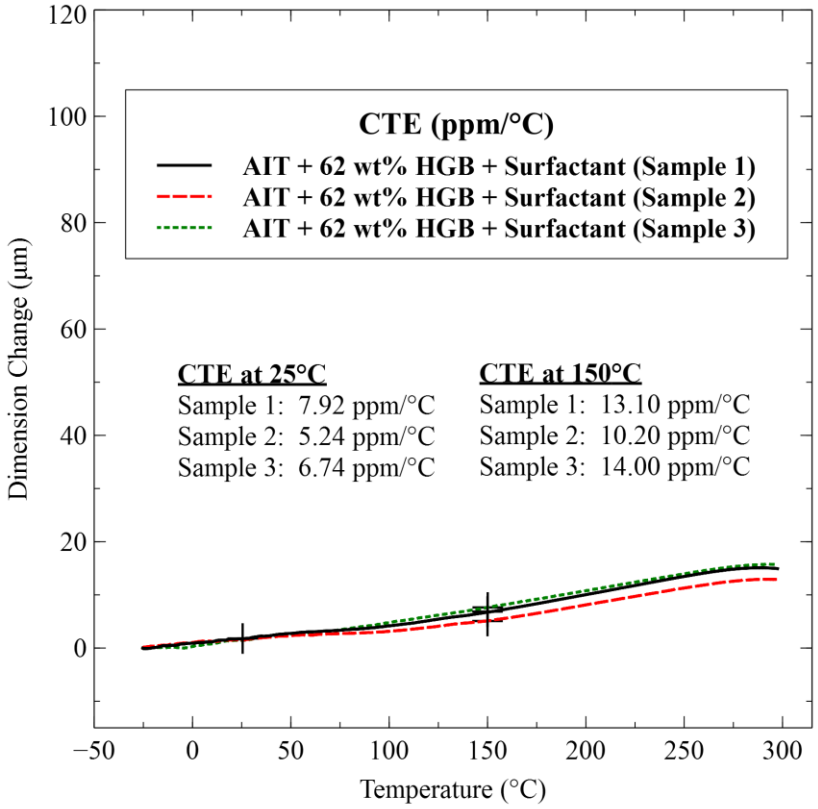

Figure 5.9: Comparison of effective CTEs of three AIT MC7883-UF samples with a 62 wt% hollow glass bead loading and 0.5 ml of Stepan POLYSTEP B-1 surfactant.

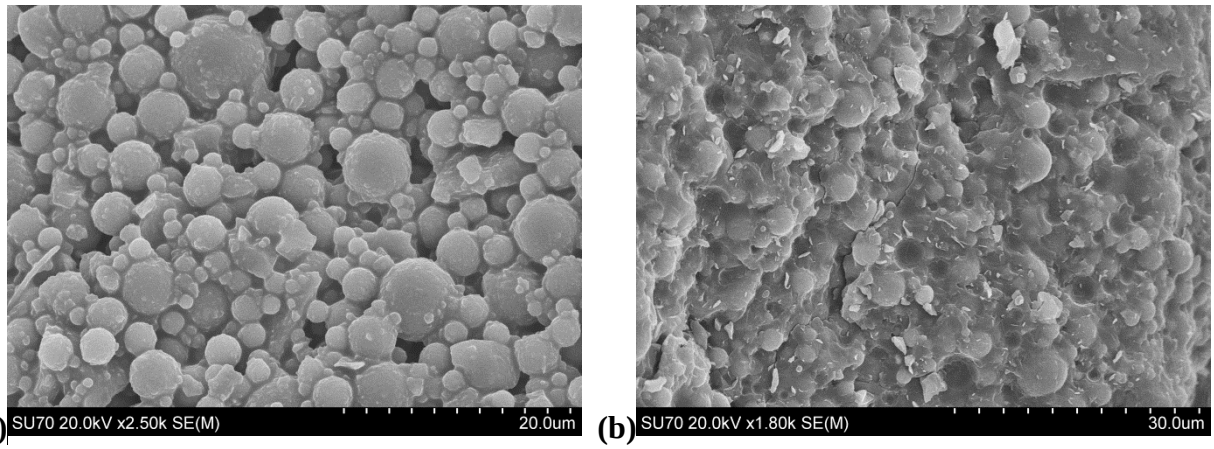

(a) **(b)**

Figure 5.10: (a) Surface-view and (b) Cross-section-view SEM images of AI Technology MC7883-UF filled with 62 wt% hollow glass beads with a particle size distribution of 1.3 µm - 9.7 µm.

The modified AI Technology composite material was molded to form a reconstructed wafer for Draper Laboratory's FOWLP platform. The material was heated in a vacuum chamber, along with a cavity wafer and IC dies. The elevated temperature reduced viscosity and enabled material flow around the embedded IC components when an injection pressure was applied. A planar surface was created on the front side of the wafer as shown in Figure 5.11(a). The backside of the wafer, as seen in Figure 5.11(b), contained excess material which was removed with a polishing process. The modified AI Technology composite material was fully cured to create a FOWLP platform core that is dimensionally stable during subsequent temperature excursions.

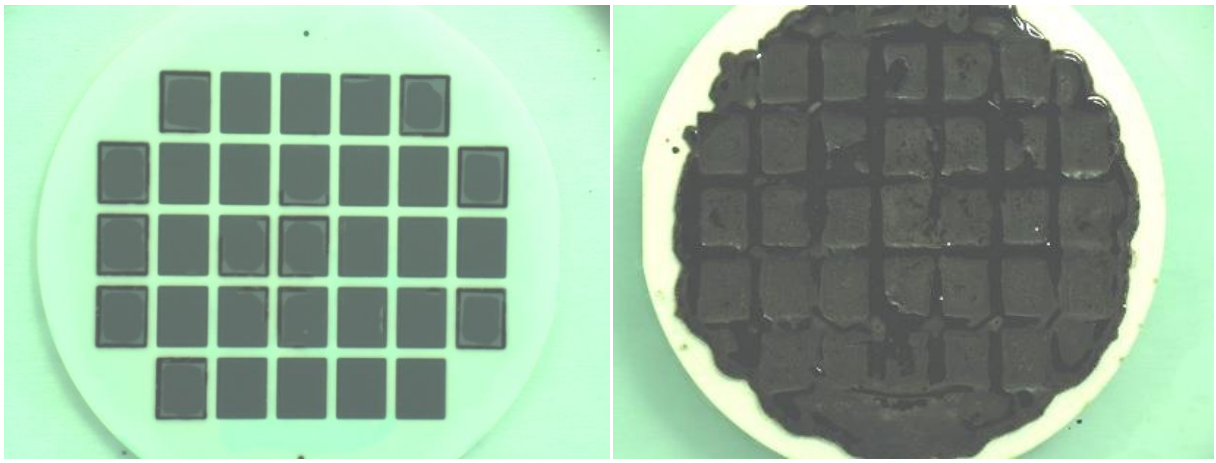

(a) **(b)**

Figure 5.11: Compression/transfer molding enabled FOWLP substrate assembly obtained with the newly developed composite material including (a) a front view image; and (b) a rear view image of the substrate with completely filled cavities. This FOWLP technology allows multiple IC chips to be encapsulated alongside of each other situated inside these refilled cavities.

5.6 Conclusions

The development of a mold compound with evenly dispersed dielectric particles was studied to obtain a low CTE, and minimal cure shrinkage for FOWLP. There is a close relationship between the filler loading quantity and resultant low overall CTE. It is observed that the higher the silica filler amount in a composite system, the lower the effective CTE is.

Through the incorporation of surfactant, the maximum amount of loaded hollow glass beads in AIT MC7883-UF host polymer at 62% weight was achieved. Three different pellet samples were prepared with the surfactant coating and the average CTE of the samples was found to be 6.6 ppm/°C at 25°C. This result was compared to the commercially available Hitachi CEL-C-2921K1 encapsulant and a 41.33 % lower CTE was achieved at 25 °C. Furthermore, this newly developed composite material exhibits outstanding thermomechanical stability at high temperatures beyond 150 °C by holding a 3X lower CTE and a higher glass transition temperature (T_g). Aside from enhancing the thermomechanical properties, the addition of surfactant also played a crucial role in improving the flow properties of the heavily loaded composite material. As shown by the SEM image, the hollow glass beads were homogeneously dispersed in the composite samples with a size distribution ranging from 1.3 μm to 9.7 μm. To validate process compatibility, the newly developed composite material was successfully adopted as a mold compound in the place of the Hitachi CEL-C-2921K1 encapsulant material for a pre-existing FOWLP process at Draper Laboratory. The enhancement of physical and thermal properties of a mold compound through excessive particle loading may cause some side effects such as relatively poor flowability and moldability. However, the only negative impact observed in our material was an increase in viscosity. Even though, the 62 wt% hollow glass beads loaded AIT MC7883-UF material was able to be molded to form a reconstructed wafer by following the process procedures detailed herein for Draper Laboratory's FOWLP platform. Additional applications for this material may include compression, transfer, or injection molding.

CHAPTER 6: CONCLUSIONS AND FUTURE WORK

6.1 Summary and Contributions to the Lab-on-a-Chip Technology

The lab-on-a-Chip (LOC) technology is anticipated to revolutionize the field of clinical diagnostics. This technology is situated to bridge the gap between the current need of affordable, rapid laboratory tests that may be performed by individuals with little to no experience in biological methods. The focus of this dissertation has been on the development of magnetic hydrogel based enabling technologies for implementation of LOC microfluidic devices.

In this work, multi-functional poly(NIPAAm-*co*-MaBP-*co*-PHEm) terpolymer systems were synthesized and characterized. These polymer systems, which are cross-linkable to a silicon substrate by exposure to UV light at λ = 365 nm, swell and collapse in response to temperature changes and they generate localized free carboxyl groups in response to UV deprotection at λ = 254 nm. This photocleavage is consistent with first-order kinetics. The generated free carboxyl groups can be used two-fold: they can be used to locally tune the swelling characteristics and transition temperature of the polymer; and they can also be used to chemically pattern cationic markers, proteins, or nanoparticles to the deprotected regions of the coating. The terpolymer system has been characterized through UV spectroscopy, Fourier transform infrared (FTIR) spectroscopy, ellipsometry, atomic force microscopy (AFM), and fluorescent microscopy. All of these methods agree and confirm that the terpolymer system has been locally deprotected. Fluorescent microscopy experiments confirmed that the positively

charged dye, YOYO-1, is specifically attached to the negatively charged deprotected areas in the terpolymer system.

The attachment of positive charged dye to negatively charged deprotected areas of a poly(NIPAAm-*co*-MaBP-*co*-PHEm) film has been achieved successfully. Magnetic nanoparticles have shown to carry a high positive charge density (σ = 0.3 $C.m^{-2}$) [303]. This allows the magnetic nanoparticles to be dispersable in water and create cationic solids free from agglomeration. Selective attachment of cationic magnetic nanoparticles to poly(NIPAAm) functional terpolymer is appealing. The exposure to AC magnetic fields can lead to localized swelling and collapsing characteristics of the poly(NIPPAm-*co*-MaBP-*co*-PHEm) system.

A novel approach for fabricating micromanipulators or antifouling surfaces has also been presented. The surfaces were generated by fabricating a series of magnetic hydrogel micro-beams that undergo a de-buckling/buckling effect in the presence and absence of AC magnetic fields. Furthermore, newly synthesized Fe_3O_4 nano-octopods were embedded in the polymer system. Due to their surface anisotropy these nano-octopods exhibited a superior heating efficiency compared to commercially available Fe_3O_4 nanoparticles. Photolithography techniques were employed to develop the SU-8 master mold and soft lithography methods were used to fabricate the hydrogel magnetite composite micro-actuators, such as micro-beam arrays.

Random movement of 50 μm polystyrene beads was achieved by remote activation of the microfabricated surface-attached micromanipulators. It would be interesting to investigate the controlled movement of these beads. By using different types of magnetic nanomaterials, one would obtain different response times and physical-chemical reactions in the polymer under the same magnetic field and frequency. Additionally, the response time of nanoparticle heating efficiency can be improved by increasing the magnetic field and/or the frequency, which would

result in faster response time for the PNIPAAm-Fe_3O_4 nanocomposite based micro-manipulators. To the best of our knowledge, this is the first time that surface attached magnetic hydrogels have been demonstrated. Furthermore, the smart surfaces have exhibited a fast response time of 25 seconds for collapsing and 75 seconds for swelling, which is a much faster response time than similar polymer nanocomposites in prior reports.

Finally, a mold compound with an ultra-low CTE of 6.6 ppm/°C was developed. The silica and glass bead loading of underfill epoxy materials was investigated. A thermomechanical analyzer was used to characterize the developed composite materials. This new material is now implemented in the Draper Laboratory's FOWLP platform.

6.2 Recommendation for Future Work

Wirebonded microcoils have been demonstrated to generate highly concentrated magnetic fields and used implemented in microfluidic devices for on-chip nuclear magnetic resonance (NMR) [304]. As seen in Figure 6.1, these microcoils have 17 windings, with a coil diameter of 700 μm, and a wire diameter of 25 μm. The microcoil, when operated at 393 kHz, has a calculated magnetic field of 300 Oe (24 kA/m) at its center and 190 Oe (15 kA/m) at the top.

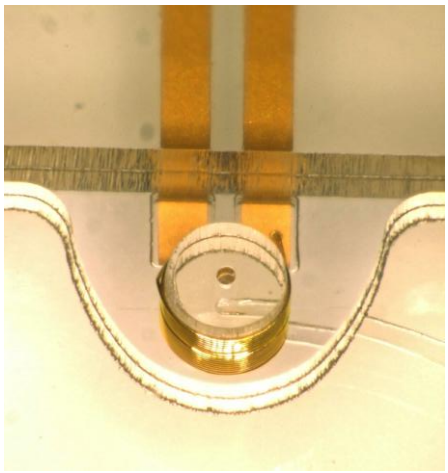

Figure 6.1: Image of a 17 turn microcoil that is capable of generating strong magnetic field

A PNIPAAm hydrogel was prepared with 10 wt% commercial Fe_3O_4 nanoparticles and placed at the surface of the coil. Figure 6.2 shows an optical image of the response of the magnetic hydrogel to the magnetic field provided by the microcoil. After 10 seconds of exposure the hydrogelis for the most part collapsed.

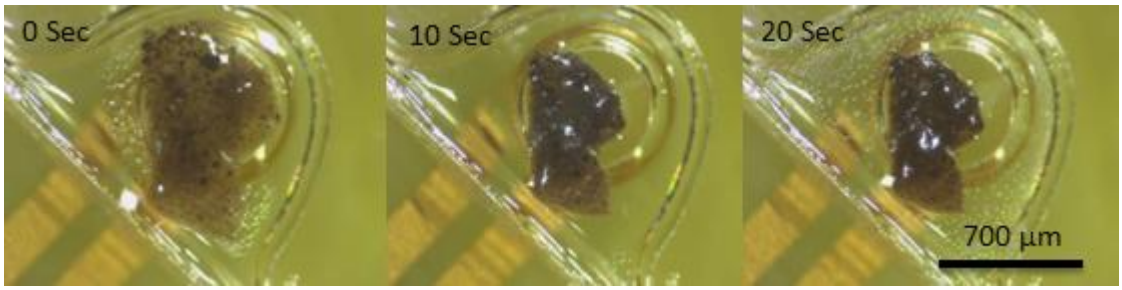

Figure 6.2: Top-view image showing the magnetic PNIPAAm hydrogel responding to the AC magnetic field generated by the microcoil

It is worth noting that the power consumption of the microcoil for the swift actuation is merely 0.25 W. In order to achieve a similar response with an induction heating system, the instrument would be operated at 197 A. An array of microcoils could be used for localized actuation. This way, only the chosen magnetic PNIPAAm hydrogel device would be actuated, which is impossible to do with current induction heating systems. In addition, strategic design of actuator geometries can lead to controlled manipulation when working with the smart surfaces.

REFERENCES

1. Feynman, R.P., *There's plenty of room at the bottom.* Engineering and science, 1960. **23**(5): p. 22-36.

2. Petersen, K.E., *Silicon as a mechanical material.* Proceedings of the IEEE, 1982. **70**(5): p. 420-457.

3. Manz, A., N. Graber, and H.M. Widmer, *Miniaturized total chemical analysis systems: A novel concept for chemical sensing.* Sensors and Actuators B: Chemical, 1990. **1**(1â€“6): p. 244-248.

4. Nastruzzi, C., et al., *Applications of Dielectrophoresis-based Lab-on-a-chip Devices in Pharmaceutical Sciences and Biomedicine*, in *CMOS Biotechnology*, H. Lee, R. Westervelt, and D. Ham, Editors. 2007, Springer US. p. 145-178.

5. Shi, J., et al., *Highly parallel mix-and-match fabrication of nanopillar arrays integrated in microfluidic channels for long DNA molecule separation.* Applied Physics Letters, 2007. **91**(15): p. 153114.

6. Demello, A.J., *Control and detection of chemical reactions in microfluidic systems.* Nature, 2006. **442**(7101): p. 394-402.

7. Mehling, M. and S. Tay, *Microfluidic cell culture.* Current opinion in Biotechnology, 2014. **25**: p. 95-102.

8. Yoon, J.-Y., *Lab-on-a-Chip Biosensors*, in *Introduction to Biosensors*2013, Springer. p. 225-256.

9. Mitchell, P., *Microfluidics[mdash]downsizing large-scale biology.* Nat Biotech, 2001. **19**(8): p. 717-721.

10. Meldrum, D.R. and M.R. Holl, *Microscale Bioanalytical Systems.* Science, 2002. **297**(5584): p. 1197-1198.

11. Burns, M.A., *Everyone's a (Future) Chemist.* Science, 2002. **296**(5574): p. 1818-1819.

12. Bélanger, M.C. and Y. Marois, *Hemocompatibility, biocompatibility, inflammatory and in vivo studies of primary reference materials low-density polyethylene and polydimethylsiloxane: A review.* Journal of Biomedical Materials Research, 2001. **58**(5): p. 467-477.

13. Duffy, D.C., et al., *Rapid Prototyping of Microfluidic Systems in Poly(dimethylsiloxane).* Analytical Chemistry, 1998. **70**(23): p. 4974-4984.

14. Jo, B.H., et al., *Three-dimensional micro-channel fabrication in polydimethylsiloxane (PDMS) elastomer.* Microelectromechanical Systems, Journal of, 2000. **9**(1): p. 76-81.

15. Xing, Y., C. Grosjean, and T. Yu-Chong, *Design, fabrication, and testing of micromachined silicone rubber membrane valves.* Microelectromechanical Systems, Journal of, 1999. **8**(4): p. 393-402.

16. Khoo, M. and C. Liu, *Micro magnetic silicone elastomer membrane actuator.* Sensors and Actuators A: Physical, 2001. **89**(3): p. 259-266.

17. Laser, D. and J. Santiago, *A review of micropumps.* Journal of Micromechanics and Microengineering, 2004. **14**(6): p. R35.

18. Weibel, D.B., et al., *Torque-actuated valves for microfluidics.* Analytical Chemistry, 2005. **77**(15): p. 4726-4733.

19. Thorsen, T., S.J. Maerkl, and S.R. Quake, *Microfluidic Large-Scale Integration.* Science, 2002. **298**(5593): p. 580-584.

20. Hong, J.W. and S.R. Quake, *Integrated nanoliter systems.* Nat Biotech, 2003. **21**(10): p. 1179-1183.

21. Ganther, A., et al., *Micromixing of miscible liquids in segmented gas-liquid flow.* Langmuir, 2005. **21**(4): p. 1547-1555.

22. Unger, M.A., et al., *Monolithic Microfabricated Valves and Pumps by Multilayer Soft Lithography*. Science, 2000. **288**(5463): p. 113-116.

23. Nguyen, N.-T. and Z. Wu, *Micromixers - a review*. Journal of Micromechanics and Microengineering, 2005. **15**(2): p. R1.

24. Garstecki, P., M.A. Fischbach, and G.M. Whitesides, *Design for mixing using bubbles in branched microfluidic channels.* Applied Physics Letters, 2005. **86**(24): p. 244108.

25. SCHILD, #160, and H. G., *Poly (N-isopropylacrylamide) : experiment, theory and application*. Vol. 17. 1992, Kidlington, ROYAUME-UNI: Elsevier.

26. Kippelen, B., et al., *Infrared Photorefractive Polymers and Their Applications for Imaging.* Science, 1998. **279**(5347): p. 54-57.

27. Lowe, A.B. and C.L. McCormick, *Synthesis and Solution Properties of Zwitterionic Polymers* Chemical Reviews, 2002. **102**(11): p. 4177-4190.

28. Torres-Lugo, M. and N.A. Peppas, *Molecular Design and in Vitro Studies of Novel pH-Sensitive Hydrogels for the Oral Delivery of Calcitonin.* Macromolecules, 1999. **32**(20): p. 6646-6651.

29. Shiga, T., *Deformation and Viscoelastic Behavior of Polymer Gels in Electric Fields*, in *Neutron Spin Echo Spectroscopy Viscoelasticity Rheology*1997, Springer Berlin Heidelberg. p. 131-163.

30. Xulu, P.M., G.v. Filipcsei, and M.s. ZrÃ-nyi, *Preparation and Responsive Properties of Magnetically Soft Poly(N-isopropylacrylamide) Gels.* Macromolecules, 2000. **33**(5): p. 1716-1719.

31. da Silva, R.M.P., J.o.F. Mano, and R.L. Reis, *Smart thermoresponsive coatings and surfaces for tissue engineering: switching cell-material boundaries.* Trends in Biotechnology, 2007. **25**(12): p. 577-583.

32. Wong, V.N., et al., *Separation of Peptides with Polyionic Nanosponges for MALDI-MS Analysis.* Langmuir, 2009. **25**(3): p. 1459-1465.

33. Kobayashi, J. and T. Okano, *Fabrication of a thermoresponsive cell culture dish: a key technology for cell sheet tissue engineering.* Science and Technology of Advanced Materials. **11**(1): p. 014111.

34. Hu, J. and S. Liu, *Responsive Polymers for Detection and Sensing Applications: Current Status and Future Developments.* Macromolecules. **43**(20): p. 8315-8330.

35. Kim, B. and A. Chilkoti, *Allosteric Actuation of Inverse Phase Transition of a Stimulus-Responsive Fusion Polypeptide by Ligand Binding.* Journal of the American Chemical Society, 2008. **130**(52): p. 17867-17873.

36. Bajpai, A.K., et al., *Responsive polymers in controlled drug delivery.* Progress in Polymer Science, 2008. **33**(11): p. 1088-1118.

37. Heskins, M. and J.E. Guillet, *Solution Properties of Poly(N-isopropylacrylamide).* Journal of Macromolecular Science: Part A - Chemistry, 1968. **2**(8): p. 1441-1455.

38. Klouda, L. and A.G. Mikos, *Thermoresponsive hydrogels in biomedical applications.* European Journal of Pharmaceutics and Biopharmaceutics, 2008. **68**(1): p. 34-45.

39. Shibayama, M. and T. Tanaka, *Volume phase transition and related phenomena of polymer gels*, in *Responsive Gels: Volume Transitions I*, K. Dušek, Editor 1993, Springer Berlin Heidelberg. p. 1-62.

40. Kujawa, P. and F.o.M. Winnik, *Volumetric Studies of Aqueous Polymer Solutions Using Pressure Perturbation Calorimetry: A New Look at the Temperature-Induced Phase Transition of Poly(N-isopropylacrylamide) in Water and D2O.* Macromolecules, 2001. **34**(12): p. 4130-4135.

41. Erbil, C., Y. Yıldız, and N. Uyanık, *N-Isopropylacrylamide/monoalkyl itaconate copolymers and N-isopropylacrylamide/itaconic acid/dimethyl itaconate terpolymers.* Polymers for Advanced Technologies, 2009. **20**(12): p. 926-933.

42. Carias, V., J. Wang, and R. Toomey, *Poly(N-isopropylacrylamide) Cross-Linked Coatings with Phototunable Swelling.* Langmuir, 2014. **30**(14): p. 4105-4110.

43. Zrínyi, M., *Intelligent polymer gels controlled by magnetic fields.* Colloid & Polymer Science, 2000. **278**(2): p. 98-103.

44. Satarkar, N.S. and J.Z. Hilt, *Magnetic hydrogel nanocomposites for remote controlled pulsatile drug release.* Journal of Controlled Release, 2008. **130**(3): p. 246-251.

45. Bhardwaj, R. and J. Blanchard, *Controlled-release delivery system for the α-MSH analog Melanotan-I using poloxamer 407.* Journal of Pharmaceutical Sciences, 1996. **85**(9): p. 915-919.

46. Jeong, B., et al., *Biodegradable block copolymers as injectable drug-delivery systems.* Nature, 1997. **388**(6645): p. 860-862.

47. Jeong, B., Y.H. Bae, and S.W. Kim, *Thermoreversible Gelation of PEG-PLGA-PEG Triblock Copolymer Aqueous Solutions.* Macromolecules, 1999. **32**(21): p. 7064-7069.

48. Chenite, A., et al., *Novel injectable neutral solutions of chitosan form biodegradable gels in situ.* Biomaterials, 2000. **21**(21): p. 2155-2161.

49. Schmaljohann, D., *Thermo- and pH-responsive polymers in drug delivery.* Advanced Drug Delivery Reviews, 2006. **58**(15): p. 1655-1670.

50. Dai, S., P. Ravi, and K.C. Tam, *pH-Responsive polymers: synthesis, properties and applications.* Soft Matter, 2008. **4**(3): p. 435-449.

51. Zhang, J. and N.A. Peppas, *Morphology of poly(methacrylic acid)/poly(N-isopropyl acrylamide) interpenetrating polymeric networks.* Journal of Biomaterials Science, Polymer Edition, 2002. **13**(5): p. 511-525.

52. Godbey, W.T., K.K. Wu, and A.G. Mikos, *Poly(ethylenimine) and its role in gene delivery.* Journal of Controlled Release, 1999. **60**(2–3): p. 149-160.

53. Lackey, C.A., et al., *Hemolytic Activity of pH-Responsive Polymer-Streptavidin Bioconjugates†.* Bioconjugate Chemistry, 1999. **10**(3): p. 401-405.

54. Gan, L.H., Y.Y. Gan, and G.R. Deen, *Poly(N-acryloyl-N'-propylpiperazine): A New Stimuli-Responsive Polymer.* Macromolecules, 2000. **33**(21): p. 7893-7897.

55. Cappello, J., et al., *In-situ self-assembling protein polymer gel systems for administration, delivery, and release of drugs.* Journal of Controlled Release, 1998. **53**(1–3): p. 105-117.

56. Wang, C., R.J. Stewart, and J. Kopecek, *Hybrid hydrogels assembled from synthetic polymers and coiled-coil protein domains.* Nature, 1999. **397**(6718): p. 417-420.

57. Schumers, J.-M., C.-A. Fustin, and J.-F. Gohy, *Light-Responsive Block Copolymers.* Macromolecular Rapid Communications, 2010. **31**(18): p. 1588-1607.

58. Wang, G., X. Tong, and Y. Zhao, *Preparation of Azobenzene-Containing Amphiphilic Diblock Copolymers for Light-Responsive Micellar Aggregates.* Macromolecules, 2004. **37**(24): p. 8911-8917.

59. Wang, Y., et al., *Block copolymer aggregates with photo-responsive switches: Towards a controllable supramolecular container.* Polymer, 2009. **50**(20): p. 4821-4828.

60. Jochum, F.D. and P. Theato, *Thermo- and light responsive micellation of azobenzene containing block copolymers.* Chemical Communications, 2010. **46**(36): p. 6717-6719.

61. Yesodha, S.K., C.K. Sadashiva Pillai, and N. Tsutsumi, *Stable polymeric materials for nonlinear optics: a review based on azobenzene systems.* Progress in Polymer Science, 2004. **29**(1): p. 45-74.

62. Zhao, Y., L. Tremblay, and Y. Zhao, *Doubly photoresponsive and water-soluble block copolymers: Synthesis and thermosensitivity.* Journal of Polymer Science Part A: Polymer Chemistry, 2010. **48**(18): p. 4055-4066.

63. Babin, J., M. Lepage, and Y. Zhao, *"Decoration" of Shell Cross-Linked Reverse Polymer Micelles Using ATRP: A New Route to Stimuli-Responsive Nanoparticles.* Macromolecules, 2008. **41**(4): p. 1246-1253.

64. Jiang, J., et al., *Polymer Micelles Stabilization on Demand through Reversible Photo-Cross-Linking.* Macromolecules, 2007. **40**(4): p. 790-792.

65. Jiang, J., et al., *Toward Photocontrolled Release Using Light-Dissociable Block Copolymer Micelles.* Macromolecules, 2006. **39**(13): p. 4633-4640.

66. Jiang, X., et al., *Multiple Micellization and Dissociation Transitions of Thermo- and Light-Sensitive Poly(ethylene oxide)-b-poly(ethoxytri(ethylene glycol) acrylate-co-o-nitrobenzyl acrylate) in Water.* Macromolecules, 2008. **41**(7): p. 2632-2643.

67. Jiang, J., X. Tong, and Y. Zhao, *A New Design for Light-Breakable Polymer Micelles.* Journal of the American Chemical Society, 2005. **127**(23): p. 8290-8291.

68. Lee, H.-i., et al., *Light-Induced Reversible Formation of Polymeric Micelles.* Angewandte Chemie International Edition, 2007. **46**(14): p. 2453-2457.

69. Gilchrist, R., et al., *Selective inductive heating of lymph nodes.* Annals of surgery, 1957. **146**(4): p. 596.

70. MEDAL, R., et al., *Controlled radio-frequency generator for production of localized heat in intact animal: Mechanism and construction.* AMA Archives of Surgery, 1959. **79**(3): p. 427-431.

71. Gilchrist, R., et al., *Effects of electromagnetic heating on internal viscera a preliminary to the treatment of human tumors.* Annals of surgery, 1965. **161**(6): p. 890.

72. Jordan, A., et al., *Endocytosis of dextran and silan-coated magnetite nanoparticles and the effect of intracellular hyperthermia on human mammary carcinoma cells in vitro.* Journal of Magnetism and Magnetic Materials, 1999. **194**(1): p. 185-196.

73. Moroz, P., S. Jones, and B. Gray, *Magnetically mediated hyperthermia: current status and future directions.* International Journal of Hyperthermia, 2002. **18**(4): p. 267-284.

74. Ge, Y., et al., *Fluorescence modified chitosan-coated magnetic nanoparticles for high-efficient cellular imaging.* Nanoscale research letters, 2009. **4**(4): p. 287-295.

75. Whitesides, G.M., R.J. Kazlauskas, and L. Josephson, *Magnetic separations in biotechnology.* Trends in Biotechnology, 1983. **1**(5): p. 144-148.

76. Chemla, Y.R., et al., *Ultrasensitive magnetic biosensor for homogeneous immunoassay.* Proceedings of the National Academy of Sciences, 2000. **97**(26): p. 14268-14272.

77. Akbarzadeh, A., M. Samiei, and S. Davaran, *Magnetic nanoparticles: preparation, physical properties, and applications in biomedicine.* Nanoscale research letters, 2012. **7**(1): p. 1-13.

78. Wahajuddin, S.A., *Superparamagnetic iron oxide nanoparticles: magnetic nanoplatforms as drug carriers.* International journal of nanomedicine, 2012. **7**: p. 3445.

79. Babes, L., et al., *Synthesis of Iron Oxide Nanoparticles Used as MRI Contrast Agents: A Parametric Study.* Journal of Colloid and Interface Science, 1999. **212**(2): p. 474-482.

80. Ahmed, N., et al., *New oil-in-water magnetic emulsion as contrast agent for in vivo magnetic resonance imaging (MRI).* Journal of biomedical nanotechnology, 2013. **9**(9): p. 1579-1585.

81. Wang, C., R. Xu, and L. Tang, *The local heating effect by magnetic nanoparticles aggregate on support lipid bilayers.* Journal of biomedical nanotechnology, 2013. **9**(7): p. 1210-1215.

82. Samanta, B., et al., *Protein-passivated Fe 3 O 4 nanoparticles: low toxicity and rapid heating for thermal therapy.* Journal of Materials Chemistry, 2008. **18**(11): p. 1204-1208.

83. Fukushima, T., et al., *Effects of beta-adrenergic receptor activation on alveolar macrophage cytoplasmic motility.* American Journal of Physiology - Lung Cellular and Molecular Physiology, 1993. **265**(1): p. L67-L72.

84. Hergt, R., et al., *Maghemite nanoparticles with very high AC-losses for application in RF-magnetic hyperthermia.* Journal of Magnetism and Magnetic Materials, 2004. **270**(3): p. 345-357.

85. Andrä, W. and H. Nowak, *Magnetism in medicine: a handbook*2007: John Wiley & Sons.

86. Néel, L., *Théorie du traînage magnétique des ferromagnétiques en grains fins avec applications aux terres cuites.* Ann. géophys, 1949. **5**(2): p. 99-136.

87. Brown Jr, W.F., *Thermal fluctuations of a single-domain particle.* Journal of Applied Physics, 1963. **34**(4): p. 1319-1320.

88. Suto, M., et al., *Heat dissipation mechanism of magnetite nanoparticles in magnetic fluid hyperthermia.* Journal of Magnetism and Magnetic Materials, 2009. **321**(10): p. 1493-1496.

89. Pankhurst, Q.A., et al., *Applications of magnetic nanoparticles in biomedicine.* Journal of Physics D: Applied Physics, 2003. **36**(13): p. R167.

90. Mason, P., et al., *Effects of frequency, permittivity, and voxel size on predicted specific absorption rate values in biological tissue during electromagnetic-field exposure.* Microwave Theory and Techniques, IEEE Transactions on, 2000. **48**(11): p. 2050-2058.

91. Yan, M., J. Fresnais, and J.-F. Berret, *Growth mechanism of nanostructured superparamagnetic rods obtained by electrostatic co-assembly.* Soft Matter, 2010. **6**(9): p. 1997-2005.

92. Roca, A., et al., *Progress in the preparation of magnetic nanoparticles for applications in biomedicine.* Journal of Physics D: Applied Physics, 2009. **42**(22): p. 224002.

93. Schladt, T.D., et al., *Au@ MnO nanoflowers: hybrid nanocomposites for selective dual functionalization and imaging.* Angewandte Chemie International Edition, 2010. **49**(23): p. 3976-3980.

94. Gao, G., et al., *Shape-controlled synthesis and magnetic properties of monodisperse Fe3O4 nanocubes.* Crystal Growth & Design, 2010. **10**(7): p. 2888-2894.

95. Comesaña-Hermo, M., et al., *Stable single domain Co nanodisks: Synthesis, structure and magnetism.* Journal of Materials Chemistry, 2012. **22**(16): p. 8043-8047.

96. Khurshid, H., et al., *Synthesis and magnetic properties of core/shell FeO/Fe3O4 nano-octopods.* Journal of Applied Physics, 2013. **113**(17): p. 17B508.

97. Huygens, C., *Treatise on light, 1690*, 1962, Dover Publications.

98. Drude, P., C. Riborg, and R.A. Millikan, *The Theory of Optics... Translated from the German by CR Mann and RA Millikan*1902: London; New York [printed].

99. Tronstad, L., *The investigation of thin surface films on metals by means of reflected polarized light.* Transactions of the Faraday Society, 1933. **29**(140): p. 502-514.

100. Rothen, A., *The ellipsometer, an apparatus to measure thicknesses of thin surface films.* Review of Scientific Instruments, 1945. **16**(2): p. 26-30.

101. Newton, I., *A Letter of Mr. Isaac Newton, Professor of the Mathematicks in the University of Cambridge; Containing His New Theory about Light and Colors: Sent by the Author to the Publisher from Cambridge, Febr. 6. 1671/72; In Order to be Communicated to the R. Society.* Philosophical Transactions, 1671. **6**(69-80): p. 3075-3087.

102. Kirchhoff, G., *Ueber das Verhältniss zwischen dem Emissionsvermögen und dem Absorptionsvermögen der Körper für Wärme und Licht.* Annalen der Physik, 1860. **185**(2): p. 275-301.

103. Simoni, R.D., et al., *A Classic Instrument: The Beckman DU Spectrophotometer and Its Inventor, Arnold O. Beckman.* Journal of Biological Chemistry, 2003. **278**(49): p. e1.

104. Atkins, P., *Julio de, Paula Atkin's Physical Chemistry*, 2006, Oxford University Press.

105. Binnig, G., et al., *Surface studies by scanning tunneling microscopy.* Physical review letters, 1982. **49**(1): p. 57.

106. Young, R., J. Ward, and F. Scire, *The topografiner: an instrument for measuring surface microtopography.* Review of Scientific Instruments, 1972. **43**(7): p. 999-1011.

107. Binnig, G., C.F. Quate, and C. Gerber, *Atomic Force Microscope.* Physical review letters, 1986. **56**(9): p. 930-933.

108. Martin, Y., C. Williams, and H.K. Wickramasinghe, *Atomic force microscope–force mapping and profiling on a sub 100-Å scale.* Journal of Applied Physics, 1987. **61**(10): p. 4723-4729.

109. VanLandingham, M., et al., *Nanoscale indentation of polymer systems using the atomic force microscope.* The Journal of adhesion, 1997. **64**(1-4): p. 31-59.

110. Revenko, I. *Probing the life sciences with atomic force microscopy*. in *Micro-and Nanostructures of Biological Systems, Proceedings of 1st Symposium held at the Martin Luther University Halle-Wittenberg at Halle*. 2000.

111. Shakesheff, K.M., et al., *The Role of Scanning Probe Microscopy in Drug Delivery Research.* 1996. **13**(3-4): p. 225-256.

112. Magonov, S., *Visualization of polymers at surfaces and interfaces with atomic force microscopy.* Handbook of Surfaces and Interfaces of Materials, 2001. **2**: p. 393-429.

113. Takano, H., et al., *Chemical and biochemical analysis using scanning force microscopy.* Chemical Reviews, 1999. **99**(10): p. 2845-2890.

114. Giessibl, F.J. and S. Morita, *Non-contact AFM.* Journal of Physics: Condensed Matter, 2012. **24**(8): p. 080301.

115. van den Berg, R., et al., *Atomic force microscopy of thin triblock copolymer films.* Polymer, 1994. **35**(26): p. 5778-5781.

116. Lozinskiĭ, M.G.e., *Industrial applications of induction heating*1969: Pergamon.

117. Cable, J.W., *Induction and dielectric heating*1954: Reinhold.

118. Esteve, V., et al., *Improving the efficiency of IGBT series-resonant inverters using pulse density modulation.* Industrial Electronics, IEEE Transactions on, 2011. **58**(3): p. 979-987.

119. Yilmaz, I., M. Ermiş, and I. Çadırcı, *Medium-frequency induction melting furnace as a load on the power system.* Industry Applications, IEEE Transactions on, 2012. **48**(4): p. 1203-1214.

120. Chudjuarjeen, S., A. Sangswang, and C. Koompai. *An improved LLC resonant inverter for induction heating with asymmetrical control*. in *Industrial Electronics, 2009. ISIE 2009. IEEE International Symposium on*. 2009. IEEE.

121. Ahmed, N., *High-frequency soft-switching ac conversion circuit with dual-mode PWM/PDM control strategy for high-power IH applications.* Industrial Electronics, IEEE Transactions on, 2011. **58**(4): p. 1440-1448.

122. Rodriguez, J. and S.B. Lee, *A multilevel inverter topology for inductively coupled power transfer.* Power Electronics, IEEE Transactions on, 2006. **21**(6): p. 1607-1617.

123. Dawson, F.P. and P. Jain, *A comparison of load commutated inverter systems for induction heating and melting applications.* Power Electronics, IEEE Transactions on, 1991. **6**(3): p. 430-441.

124. Koertzen, H.W., J.D. Van Wyk, and J. Ferreira. *Design of the half-bridge, series resonant converter for induction cooking*. in *Power Electronics Specialists Conference, 1995. PESC'95 Record., 26th Annual IEEE*. 1995. IEEE.

125. Dede, E.J., et al., *25-kW/50-kHz generator for induction heating.* Industrial Electronics, IEEE Transactions on, 1991. **38**(3): p. 203-209.

126. Esteve, V., et al. *Induction heating inverter with simultaneous dual-frequency output*. in *Applied Power Electronics Conference and Exposition, 2006. APEC'06. Twenty-First Annual IEEE*. 2006. IEEE.

127. Kazimerczuk, M. and D. Czarkowski. *Resonant power converters*. in *Fuel and Energy Abstracts*. 1995.

128. Steigerwald, R.L., *A comparison of half-bridge resonant converter topologies.* Power Electronics, IEEE Transactions on, 1988. **3**(2): p. 174-182.

129. Ngoc, H.P., et al., *Phase angle control of high-frequency resonant currents in a multiple inverter system for zone-control induction heating.* Power Electronics, IEEE Transactions on, 2011. **26**(11): p. 3357-3366.

130. Pham, H.N., et al., *Dynamic analysis and control for resonant currents in a zone-control induction heating system.* Power Electronics, IEEE Transactions on, 2013. **28**(3): p. 1297-1307.

131. Fujita, H. and H. Akagi, *Pulse-density-modulated power control of a 4 kW, 450 kHz voltage-source inverter for induction melting applications.* Industry Applications, IEEE Transactions on, 1996. **32**(2): p. 279-286.

132. Fujita, H. and H. Akagi, *Control and performance of a pulse-density-modulated series-resonant inverter for corona discharge processes.* Industry Applications, IEEE Transactions on, 1999. **35**(3): p. 621-627.

133. Egalon, J., et al., *Multiphase system for metal disc induction heating: Modeling and RMS current control.* Industry Applications, IEEE Transactions on, 2012. **48**(5): p. 1692-1699.

134. Park, N.-J., D.-Y. Lee, and D.-S. Hyun, *A power-control scheme with constant switching frequency in class-D inverter for induction-heating jar application.* Industrial Electronics, IEEE Transactions on, 2007. **54**(3): p. 1252-1260.

135. Long, N.K., et al. *Resonant control of multi-phase induction heating systems*. in *IECON 2012-38th Annual Conference on IEEE Industrial Electronics Society*. 2012. IEEE.

136. Navarro, D., et al., *High-level synthesis for accelerating the FPGA implementation of computationally demanding control algorithms for power converters.* Industrial Informatics, IEEE Transactions on, 2013. **9**(3): p. 1371-1379.

137. Moreland, W., *The induction range: Its performance and its development problems.* IEEE Transactions on Industry Applications, 1973. **1**(IA-9): p. 81-85.

138. Forest, F., et al., *Frequency-synchronized resonant converters for the supply of multiwinding coils in induction cooking appliances.* Industrial Electronics, IEEE Transactions on, 2007. **54**(1): p. 441-452.

139. Forest, F., et al., *Principle of a multi-load/single converter system for low power induction heating.* Power Electronics, IEEE Transactions on, 2000. **15**(2): p. 223-230.

140. Lucía, Ó., et al., *A versatile power electronics test-bench architecture applied to domestic induction heating.* Industrial Electronics, IEEE Transactions on, 2011. **58**(3): p. 998-1007.

141. Burdio, J.M., et al., *A two-output series-resonant inverter for induction-heating cooking appliances.* Power Electronics, IEEE Transactions on, 2005. **20**(4): p. 815-822.

142. Lucía, O.s., et al., *Series-resonant multiinverter for multiple induction heaters.* Power Electronics, IEEE Transactions on, 2010. **25**(11): p. 2860-2868.

143. Lucia, O., et al., *Multiple-output resonant matrix converter for multiple induction heaters.* Industry Applications, IEEE Transactions on, 2012. **48**(4): p. 1387-1396.

144. Sarnago, H., et al., *Class-D/DE dual-mode-operation resonant converter for improved-efficiency domestic induction heating system.* Power Electronics, IEEE Transactions on, 2013. **28**(3): p. 1274-1285.

145. Sarnago, H., A. Mediano, and O. Lucia, *High efficiency AC–AC power electronic converter applied to domestic induction heating.* Power Electronics, IEEE Transactions on, 2012. **27**(8): p. 3676-3684.

146. Fujita, A., et al. *Latest developments of high-frequency series load resonant inverter type built-in cooktops for induction heated all metallic appliances*. in *Power Electronics and Motion Control Conference, 2009. IPEMC'09. IEEE 6th International*. 2009. IEEE.

147. Ahmed, N.A. and M. Nakaoka, *Boost-half-bridge edge resonant soft switching PWM high-frequency inverter for consumer induction heating appliances.* IEE Proceedings-Electric Power Applications, 2006. **153**(6): p. 932-938.

148. Ogura, K., et al., *Performance evaluation of edge-resonant ZVS-PWM high-frequency inverter using trench-gate IGBTs for consumer induction cooking heater.* IEE Proceedings-Electric Power Applications, 2004. **151**(5): p. 563-568.

149. Wang, S., et al., *Induction-heated cooking appliance using new quasi-resonant ZVS-PWM inverter with power factor correction.* Industry Applications, IEEE Transactions on, 1998. **34**(4): p. 705-712.

150. Jung, Y.-C., *Dual half bridge series resonant inverter for induction heating appliance with two loads.* Electronics letters, 1999. **35**(16): p. 1345-1346.

151. Acero, J., et al., *Domestic induction appliances.* IEEE Industry Applications Magazine, 2010. **2**(16): p. 39-47.

152. Primiani, V.M., S. Kovyryalov, and G. Cerri, *Rigorous electromagnetic model of an induction cooking system.* IET Science, Measurement & Technology, 2012. **6**(4): p. 238-246.

153. Acero, J., et al., *Simple resistance calculation in litz-wire planar windings for induction cooking appliances.* Magnetics, IEEE Transactions on, 2005. **41**(4): p. 1280-1288.

154. Carretero, C., et al., *Computational modeling of two partly coupled coils supplied by a double half-bridge resonant inverter for induction heating appliances.* Industrial Electronics, IEEE Transactions on, 2013. **60**(8): p. 3092-3105.

155. Acero, J., et al., *Mutual impedance of small ring-type coils for multiwinding induction heating appliances.* Power Electronics, IEEE Transactions on, 2013. **28**(2): p. 1025-1035.

156. Acero, J., et al., *Analysis and modeling of planar concentric windings forming adaptable-diameter burners for induction heating appliances.* Power Electronics, IEEE Transactions on, 2011. **26**(5): p. 1546-1558.

157. Carretero, C., et al., *Frequency-dependent modelling of domestic induction heating systems using numerical methods for accurate time-domain simulation.* IET Power Electronics, 2012. **5**(8): p. 1291-1297.

158. Lucia, O., et al., *Load-adaptive control algorithm of half-bridge series resonant inverter for domestic induction heating.* Industrial Electronics, IEEE Transactions on, 2009. **56**(8): p. 3106-3116.

159. Sarnago, H., et al., *Modulation scheme for improved operation of an RB-IGBT-based resonant inverter applied to domestic induction heating.* Industrial Electronics, IEEE Transactions on, 2013. **60**(5): p. 2066-2073.

160. Paesa, D., et al., *Adaptive simmering control for domestic induction cookers.* Industry Applications, IEEE Transactions on, 2011. **47**(5): p. 2257-2267.

161. Jimenez, O., et al., *An FPGA-based gain-scheduled controller for resonant converters applied to induction cooktops.* Power Electronics, IEEE Transactions on, 2014. **29**(4): p. 2143-2152.

162. Stauffer, P.R., T.C. Cetas, and R.C. Jones, *Magnetic induction heating of ferromagnetic implants for inducing localized hyperthermia in deep-seated tumors.* Biomedical Engineering, IEEE Transactions on, 1984(2): p. 235-251.

163. Landi, G. and A. Bakuzis, *On the energy conversion efficiency in magnetic hyperthermia applications: A new perspective to analyze the departure from the linear regime.* Journal of Applied Physics, 2012. **111**(8): p. 083915.

164. Tai, C.-C. and M.-K. Chen, *A compact half-bridge induction heating system for magnetic nanoparticle thermotherapy applications.* Biomedical Engineering: Applications, Basis and Communications, 2007. **19**(01): p. 27-35.

165. Tai, C.-C. and M. Chen, *The design of a half-bridge series-resonant type heating system for magnetic nanoparticle thermotherapy.* PIERS Online, 2007. **4**(2): p. 276-280.

166. Gómez-Polo, C., et al., *Analysis of heating effects (magnetic hyperthermia) in FeCrSiBCuNb amorphous and nanocrystalline wires.* Journal of Applied Physics, 2012. **111**(7): p. 07A314.

167. Cano, M., et al., *An induction heater device for studies of magnetic hyperthermia and specific absorption ratio measurements.* Review of Scientific Instruments, 2011. **82**(11): p. 114904.

168. Candeo, A. and F. Dughiero, *Numerical FEM models for the planning of magnetic induction hyperthermia treatments with nanoparticles.* Magnetics, IEEE Transactions on, 2009. **45**(3): p. 1658-1661.

169. Di Barba, P., F. Dughiero, and E. Sieni, *Synthesizing distributions of magnetic nanoparticles for clinical hyperthermia.* IEEE transactions on magnetics, 2012. **48**(2): p. 263-266.

170. Di Barba, P., et al., *Coupled field synthesis in magnetic fluid hyperthermia.* IEEE transactions on magnetics, 2011. **47**(5): p. 914-917.

171. Stauffer, P., et al., *Practical induction heating coil designs for clinical hyperthermia with ferromagnetic implants.* Biomedical Engineering, IEEE Transactions on, 1994. **41**(1): p. 17-28.

172. Di Barba, P., F. Dughiero, and E. Sieni, *Magnetic field synthesis in the design of inductors for magnetic fluid hyperthermia.* IEEE transactions on magnetics, 2010. **46**(8): p. 2931-2934.

173. Wen, D., *Intracellular hyperthermia: Nanobubbles and their biomedical applications.* International Journal of Hyperthermia, 2009. **25**(7): p. 533-541.

174. Gupta, A.K. and M. Gupta, *Synthesis and surface engineering of iron oxide nanoparticles for biomedical applications.* Biomaterials, 2005. **26**(18): p. 3995-4021.

175. Kim, D.-H., et al., *Heat generation of aqueously dispersed CoFe 2 O 4 nanoparticles as heating agents for magnetically activated drug delivery and hyperthermia.* Journal of Magnetism and Magnetic Materials, 2008. **320**(19): p. 2390-2396.

176. Zinn, S. and S. Semiatin, *Coil design and fabrication: basic design and modifications.* Heat Treating, 1988. **12**(3): p. 32-36.

177. Satarkar, N.S., et al., *Magnetic hydrogel nanocomposites as remote controlled microfluidic valves.* Lab on a Chip, 2009. **9**(12): p. 1773-1779.

178. Maier-Hauff, K., et al., *Intracranial thermotherapy using magnetic nanoparticles combined with external beam radiotherapy: results of a feasibility study on patients with glioblastoma multiforme.* Journal of neuro-oncology, 2007. **81**(1): p. 53-60.

179. Park, C.-H., et al., *Inductive heating of electrospun Fe 2 O 3/polyurethane composite mat under high-frequency magnetic field.* Ceramics International, 2013. **39**(8): p. 9785-9790.

180. Lee, J.-H., et al., *Exchange-coupled magnetic nanoparticles for efficient heat induction.* Nature nanotechnology, 2011. **6**(7): p. 418-422.

181. Ghosh, S. and T. Cai, *Controlled actuation of alternating magnetic field-sensitive tunable hydrogels.* Journal of Physics D: Applied Physics, 2010. **43**(41): p. 415504.

182. Hiergeist, R., et al., *Application of magnetite ferrofluids for hyperthermia.* Journal of Magnetism and Magnetic Materials, 1999. **201**(1): p. 420-422.

183. Khot, V., et al., *Induction heating studies of dextran coated MgFe 2 O 4 nanoparticles for magnetic hyperthermia.* Dalton Transactions, 2013. **42**(4): p. 1249-1258.

184. Ghosh, R., et al., *Induction heating studies of Fe3O4 magnetic nanoparticles capped with oleic acid and polyethylene glycol for hyperthermia.* Journal of Materials Chemistry, 2011. **21**(35): p. 13388-13398.

185. Liu, X.L., et al., *Optimization of surface coating on Fe 3 O 4 nanoparticles for high performance magnetic hyperthermia agents.* Journal of Materials Chemistry, 2012. **22**(17): p. 8235-8244.

186. Pérez-Camacho, M.N., et al., *Biogas reforming using renewable wind energy and induction heating.* Catalysis Today, 2015. **242**: p. 129-138.

187. Choy, T., et al., *8: 16 AM Abstract No. 187-■ Dr. Constantin Cope Medical Student Research Award Alginate microspheres with magnetically triggered gemcitabine release.* Journal of Vascular and Interventional Radiology, 2013. **24**(4): p. S88-S89.

188. Serantes, D., et al., *Multiplying magnetic hyperthermia response by nanoparticle assembling.* The Journal of Physical Chemistry C, 2014. **118**(11): p. 5927-5934.

189. Barthélémy, B., et al., *Induction heating for surface triggering styrene polymerization on titanium modified with ATRP initiator.* Journal of Colloid and Interface Science, 2011. **354**(2): p. 873-879.

190. Kargin, V. and G. Slonimskii, *DAN, 62, 239, 1948.* ZhFKh, 1949. **23**: p. 569.

191. Carias, V., J. Wang, and R. Toomey, *Poly(N-isopropylacrylamide) Cross-Linked Coatings with Phototunable Swelling.* Langmuir. **30**(14): p. 4105-4110.

192. Schenderlein, H., et al., *Preparation and Characterization of Light-Switchable Polymer Networks Attached to Solid Substrates.* Langmuir, 2013. **29**(14): p. 4525-4534.

193. Schild, H.G., *Poly (N-Isopropylacrylamide) - Experiment, Theory and Application.* Progress in Polymer Science, 1992. **17**(2): p. 163-249.

194. Habicht, J., et al., *Swelling of Thick Polymer Brushes Investigated with Ellipsometry.* Langmuir, 1999. **15**(7): p. 2460-2465.

195. Patra, L., J.M. Messman, and R. Toomey, *On the nature of volume-phase transitions in photo-cross-linked poly(cyclopropylacrylamide) and poly(N-vinylisobutyramide) coatings.* Soft Matter, 2013. **9**(16): p. 4349-4356.

196. Millaruelo, M., et al., *Photolabile Carboxylic Acid Protected Terpolymers for Surface Patterning. Part 1: Polymer Synthesis and Film Characterization.* Langmuir, 2006. **22**(22): p. 9436-9445.

197. Millaruelo, M., et al., *Photolabile Carboxylic Acid Protected Terpolymers for Surface Patterning. Part 2: Photocleavage and Film Patterning.* Langmuir, 2006. **22**(22): p. 9446-9452.

198. Prucker, O., et al., *Photochemical Attachment of Polymer Films to Solid Surfaces via Monolayers of Benzophenone Derivatives.* Journal of the American Chemical Society, 1999. **121**(38): p. 8766-8770.

199. Banerjee, A. and D.E. Falvey, *Protecting Groups That Can Be Removed through Photochemical Electron Transfer: Mechanistic and Product Studies on Photosensitized Release of Carboxylates from Phenacyl Esters.* The Journal of Organic Chemistry, 1997. **62**(18): p. 6245-6251.

200. Falvey, D.E. and C. Sundararajan, *Photoremovable protecting groups based on electron transfer chemistry.* Photochemical & Photobiological Sciences, 2004. **3**(9): p. 831-838.

201. Sheehan, J.C. and K. Umezawa, *Phenacyl photosensitive blocking groups.* The Journal of Organic Chemistry, 1973. **38**(21): p. 3771-3774.

202. Inomata, K., et al., *Synthesis of photo-functional polymers with both pendant phenacyl ester and spiro ortho ester groups and photochemical properties of the resulting polymers.* Reactive and Functional Polymers, 2000. **45**(1): p. 1-9.

203. Tanaka, T., et al., *Mechanical Instability of Gels at the Phase-Transition.* Nature, 1987. **325**(6107): p. 796-798.

204. Olsen, S.M., et al., *Enzyme-based antifouling coatings: a review.* Biofouling, 2007. **23**(5): p. 369-383.

205. Kristensen, J.B., et al., *Antifouling enzymes and the biochemistry of marine settlement.* Biotechnology advances, 2008. **26**(5): p. 471-481.

206. Yebra, D.M., S. Kiil, and K. Dam-Johansen, *Antifouling technology—past, present and future steps towards efficient and environmentally friendly antifouling coatings.* Progress in organic coatings, 2004. **50**(2): p. 75-104.

207. Flemming, H.-C., *Biofouling in water systems–cases, causes and countermeasures.* Applied microbiology and biotechnology, 2002. **59**(6): p. 629-640.

208. Yang, C., et al., *Bactericidal functionalization of wrinkle-free fabrics via covalently bonding TiO2@ Ag nanoconjugates.* Journal of materials science, 2009. **44**(7): p. 1894-1901.

209. Liu, Y., et al., *Functionalization of cotton with carbon nanotubes.* Journal of Materials Chemistry, 2008. **18**(29): p. 3454-3460.

210. Meilert, K., D. Laub, and J. Kiwi, *Photocatalytic self-cleaning of modified cotton textiles by TiO 2 clusters attached by chemical spacers.* Journal of molecular catalysis A: chemical, 2005. **237**(1): p. 101-108.

211. Bozja, J., et al., *Porphyrin-based, light-activated antimicrobial materials.* Journal of Polymer Science Part A: Polymer Chemistry, 2003. **41**(15): p. 2297-2303.

212. Meyer, B., *Approaches to prevention, removal and killing of biofilms.* International Biodeterioration & Biodegradation, 2003. **51**(4): p. 249-253.

213. Li, X., et al., *Antimicrobial activities of ZnO powder-coated PVC film to inactivate food pathogens.* International journal of food science & technology, 2009. **44**(11): p. 2161-2168.

214. Conte, A., et al., *Immobilization of lysozyme on polyvinylalcohol films for active packaging applications.* Journal of Food Protection®, 2006. **69**(4): p. 866-870.

215. Kenawy, E.-R., S. Worley, and R. Broughton, *The chemistry and applications of antimicrobial polymers: a state-of-the-art review.* Biomacromolecules, 2007. **8**(5): p. 1359-1384.

216. Asuri, P., et al., *Polymer–nanotube–enzyme composites as active antifouling films.* Small, 2007. **3**(1): p. 50-53.

217. Mueller, J. and R.H. Davis, *Protein fouling of surface-modified polymeric microfiltration membranes.* Journal of Membrane Science, 1996. **116**(1): p. 47-60.

218. Ho, C.-C. and A.L. Zydney, *Protein fouling of asymmetric and composite microfiltration membranes.* Industrial & engineering chemistry research, 2001. **40**(5): p. 1412-1421.

219. Donlan, R.M., *Biofilm formation: a clinically relevant microbiological process.* Clinical Infectious Diseases, 2001. **33**(8): p. 1387-1392.

220. Pavithra, D. and M. Doble, *Biofilm formation, bacterial adhesion and host response on polymeric implants—issues and prevention.* Biomedical Materials, 2008. **3**(3): p. 034003.

221. Kilian, K.A., et al., *Forming Antifouling Organic Multilayers on Porous Silicon Rugate Filters Towards In Vivo/Ex Vivo Biophotonic Devices.* Advanced Functional Materials, 2007. **17**(15): p. 2884-2890.

222. Ohko, Y., et al., *Self-sterilizing and self-cleaning of silicone catheters coated with TiO2 photocatalyst thin films: A preclinical work.* Journal of Biomedical Materials Research, 2001. **58**(1): p. 97-101.

223. Vasilev, K., J. Cook, and H.J. Griesser, *Antibacterial surfaces for biomedical devices.* Expert review of medical devices, 2009. **6**(5): p. 553-567.

224. Willcox, M., et al., *A novel cationic-peptide coating for the prevention of microbial colonization on contact lenses.* Journal of applied microbiology, 2008. **105**(6): p. 1817-1825.

225. Wisniewski, N. and M. Reichert, *Methods for reducing biosensor membrane biofouling.* Colloids and Surfaces B: Biointerfaces, 2000. **18**(3): p. 197-219.

226. Sharma, S., R.W. Johnson, and T.A. Desai, *XPS and AFM analysis of antifouling PEG interfaces for microfabricated silicon biosensors.* Biosensors and Bioelectronics, 2004. **20**(2): p. 227-239.

227. Desai, T.A., et al., *Nanoporous anti-fouling silicon membranes for biosensor applications.* Biosensors and Bioelectronics, 2000. **15**(9): p. 453-462.

228. Chae, K.H., et al., *Anti-fouling epoxy coatings for optical biosensor application based on phosphorylcholine.* Sensors and Actuators B: Chemical, 2007. **124**(1): p. 153-160.

229. Silber, A., N. Hampp, and W. Schuhmann, *Poly (methylene blue)-modified thick-film gold electrodes for the electrocatalytic oxidation of NADH and their application in glucose biosensors.* Biosensors and Bioelectronics, 1996. **11**(3): p. 215-223.

230. Labat-Allietta, N. and D.R. Thévenot, *Influence of calcium on glucose biosensor response and on hydrogen peroxide detection.* Biosensors and Bioelectronics, 1998. **13**(1): p. 19-29.

231. Reddy, S.M. and P.M. Vagama, *Surfactant-modified poly (vinyl chloride) membranes as biocompatible interfaces for amperometric enzyme electrodes.* Analytica chimica acta, 1997. **350**(1): p. 77-89.

232. Kingshott, P., H. Thissen, and H.J. Griesser, *Effects of cloud-point grafting, chain length, and density of PEG layers on competitive adsorption of ocular proteins.* Biomaterials, 2002. **23**(9): p. 2043-2056.

233. Zhang, F., et al., *Modification of Si (100) surface by the grafting of poly (ethylene glycol) for reduction in protein adsorption and platelet adhesion.* Journal of Biomedical Materials Research, 2001. **56**(3): p. 324-332.

234. Hamburger, R., E. Azaz, and M. Donbrow, *Autoxidation of polyoxyethylenic non-ionic surfactants and of polyethylene glycols.* Pharmaceutica Acta Helvetiae, 1974. **50**(1-2): p. 10-17.

235. Luk, Y.-Y., M. Kato, and M. Mrksich, *Self-assembled monolayers of alkanethiolates presenting mannitol groups are inert to protein adsorption and cell attachment.* Langmuir, 2000. **16**(24): p. 9604-9608.

236. Chapman, R.G., et al., *Surveying for surfaces that resist the adsorption of proteins.* Journal of the American Chemical Society, 2000. **122**(34): p. 8303-8304.

237. Kane, R.S., P. Deschatelets, and G.M. Whitesides, *Kosmotropes form the basis of protein-resistant surfaces.* Langmuir, 2003. **19**(6): p. 2388-2391.

238. Tegoulia, V.A., et al., *Surface properties, fibrinogen adsorption, and cellular interactions of a novel phosphorylcholine-containing self-assembled monolayer on gold.* Langmuir, 2001. **17**(14): p. 4396-4404.

239. Van der Heiden, A., et al., *Adsorption of proteins onto poly (ether urethane) with a phosphorylcholine moiety and influence of preadsorbed phospholipid.* Journal of Biomedical Materials Research, 1998. **40**(2): p. 195-203.

240. Österberg, E., et al., *Comparison of polysaccharide and poly (ethylene glycol) coatings for reduction of protein adsorption on polystyrene surfaces.* Colloids and Surfaces A: Physicochemical and Engineering Aspects, 1993. **77**(2): p. 159-169.

241. Brink, C., et al., *Using poly (ethylene imine) to graft poly (ethylene glycol) or polysaccharide to polystyrene.* Colloids and surfaces, 1992. **66**(2): p. 149-156.

242. Nguyen, N.-T., *5 Fabrication Issues of Biomedical Micro Devices*, in *BioMEMS and Biomedical Nanotechnology*, M. Ferrari, R. Bashir, and S. Wereley, Editors. 2007, Springer US. p. 93-115.

243. Szycher, M., J. Qiu, and M. Tanaka, *Biomaterials, Prosthetics, and Biomedical Devices*, in *Kirk-Othmer Encyclopedia of Chemical Technology*2000, John Wiley & Sons, Inc.

244. Ortega, D. and Q.A. Pankhurstb, *3 Magnetic hyperthermia.* 2013.

245. Binns, C., *Magnetic Nanoparticle Hyperthermia Treatment of Tumours*, in *Nanostructured Materials for Magnetoelectronics*, B. Aktaş and F. Mikailzade, Editors. 2013, Springer Berlin Heidelberg. p. 197-215.

246. Martinez-Boubeta, C., et al., *Learning from Nature to Improve the Heat Generation of Iron-Oxide Nanoparticles for Magnetic Hyperthermia Applications.* Sci. Rep., 2013. **3**.

247. Castellanos, A., et al., *Size-Exclusion "Capture and Release" Separations Using Surface-Patterned Poly(N-isopropylacrylamide) Hydrogels.* Langmuir, 2007. **23**(11): p. 6391-6395.

248. DuPont Jr, S.J., et al., *Swelling-induced instabilities in microscale, surface-confined poly (N-isopropylacryamide) hydrogels.* Soft Matter, 2010. **6**(16): p. 3876-3882.

249. Akintewe, O.O., et al., *Shape-changing hydrogel surfaces trigger rapid release of patterned tissue modules.* Acta biomaterialia, 2015. **11**: p. 96-103.

250. Brzoska, J.B., I.B. Azouz, and F. Rondelez, *Silanization of Solid Substrates: A Step Toward Reproducibility*. Langmuir, 1994. **10**(11): p. 4367-4373.

251. Washburn, E.W., *The Dynamics of Capillary Flow.* Physical Review, 1921. **17**(3): p. 273-283.

252. Simeonidis, K., et al., *Fe-based nanoparticles as tunable magnetic particle hyperthermia agents.* Journal of Applied Physics, 2013. **114**(10): p. 103904.

253. Tirumala, V.R., et al., *Direct-write e-beam patterning of stimuli-responsive hydrogel nanostructures.* Journal of Vacuum Science & Technology B, 2005. **23**(6): p. 3124-3128.

254. Mora, T. and A. Boudaoud, *Buckling of swelling gels.* The European Physical Journal E, 2006. **20**(2): p. 119-124.

255. Ghafar-Zadeh, E., et al., *A direct-write microfluidic fabrication process for CMOS-based Lab-on-Chip applications.* Microelectronic Engineering, 2009. **86**(10): p. 2104-2109.

256. Ghafar-Zadeh, E., M. Sawan, and D. Therriault, *Novel direct-write CMOS-based laboratory-on-chip: Design, assembly and experimental results.* Sensors and Actuators A: Physical, 2007. **134**(1): p. 27-36.

257. Norian, H., et al., *An integrated CMOS quantitative-polymerase-chain-reaction lab-on-chip for point-of-care diagnostics.* Lab on a Chip, 2014. **14**(20): p. 4076-4084.

258. Datta-Chaudhuri, T., P. Abshire, and E. Smela, *Packaging commercial CMOS chips for lab on a chip integration.* Lab on a Chip, 2014. **14**(10): p. 1753-1766.

259. Hunt, J., et al. *Synergy between 2.5/3D development and hybrid 3D Wafer Level Fanout*. in *Electronic System-Integration Technology Conference (ESTC), 2012 4th*. 2012.

260. Hunt, J., et al. *A hybrid panel embedding process for fanout*. in *Electronics Packaging Technology Conference (EPTC), 2012 IEEE 14th*. 2012.

261. Kahng, A.B., G. Robins, and E.A. Walkup, *Optimal algorithms for substrate testing in multi-chip modules.* World Scientific Publishing Co, 1996: p. 181-198.

262. Sheng, S., A. Chandrakasan, and R.W. Brodersen, *A portable multimedia terminal.* IEEE Communications Magazine, 1992. **30**(12): p. 64-75.

263. Al-Sarawi, S.F., D. Abbott, and P.D. Franzon, *A review of 3-D packaging technology*. Components, Packaging, and Manufacturing Technology, Part B: Advanced Packaging, IEEE Transactions on, 1998. **21**(1): p. 2-14.

264. Kwon, W.-S., S.-J. Ham, and K.-W. Paik, *Deformation mechanism and its effect on electrical conductivity of ACF flip chip package under thermal cycling condition: An experimental study.* Microelectronics Reliability, 2006. **46**(2–4): p. 589-599.

265. Pavio, J. and D. Hyde. *Effects of coefficient of thermal expansion mismatch on solder attached GaAs MMICs*. in *Microwave Symposium Digest, 1991., IEEE MTT-S International*. 1991.

266. Lu, T., et al., *Matrix cracking in intermetallic composites caused by thermal expansion mismatch.* Acta metallurgica et materialia, 1991. **39**(8): p. 1883-1890.

267. Zweben, C., *Advances in composite materials for thermal management in electronic packaging.* JOM, 1998. **50**(6): p. 47-51.

268. Agag, T., T. Koga, and T. Takeichi, *Studies on thermal and mechanical properties of polyimide–clay nanocomposites.* Polymer, 2001. **42**(8): p. 3399-3408.

269. Bose, S. and P. Mahanwar, *Effect of particle size of filler on properties of nylon-6.* Journal of Minerals & Materials Characterization & Engineering, 2004. **3**(1): p. 23-31.

270. Olmos, D., et al., *Effect of the presence of silica nanoparticles in the coefficient of thermal expansion of LDPE.* European Polymer Journal, 2011. **47**(8): p. 1495-1502.

271. Mascia, L. and A. Kioul, *Polyimide-silica hybrid materials by sol-gel processing.* Journal of materials science letters, 1994. **13**(9): p. 641-643.

272. Wooster, T.J., et al., *Thermal, mechanical, and conductivity properties of cyanate ester composites.* Composites Part A: Applied Science and Manufacturing, 2004. **35**(1): p. 75-82.

273. Wong, C.P. and R.S. Bollampally, *Thermal conductivity, elastic modulus, and coefficient of thermal expansion of polymer composites filled with ceramic particles for electronic packaging.* Journal of Applied Polymer Science, 1999. **74**(14): p. 3396-3403.

274. Bikiaris, D.N., et al., *Compatibilisation effect of PP-g-MA copolymer on iPP/SiO2 nanocomposites prepared by melt mixing.* European Polymer Journal, 2005. **41**(9): p. 1965-1978.

275. Yang, M. and Y. Dan, *Preparation and characterization of poly(methyl methacrylate)/titanium oxide composite particles.* Colloid and Polymer Science, 2005. **284**(3): p. 243-250.

276. Rong, M.Z., et al., *Structure–property relationships of irradiation grafted nano-inorganic particle filled polypropylene composites.* Polymer, 2001. **42**(1): p. 167-183.

277. Ash, B.J., R.W. Siegel, and L.S. Schadler, *Mechanical Behavior of Alumina/Poly(methyl methacrylate) Nanocomposites.* Macromolecules, 2004. **37**(4): p. 1358-1369.

278. Chandra, A., et al., *Study of utilizing thin polymer surface coating on the nanoparticles for melt compounding of polycarbonate/alumina nanocomposites and their optical properties.* Composites Science and Technology, 2008. **68**(3–4): p. 768-776.

279. Chandra, A., et al., *Study of polystyrene/titanium dioxide nanocomposites via melt compounding for optical applications.* Polymer Composites, 2007. **28**(2): p. 241-250.

280. Jeon, H.S., et al., *Characterization of polyisopreneâ€"clay nanocomposites prepared by solution blending.* Polymer, 2003. **44**(19): p. 5749-5758.

281. He, J.-P., et al., *In situ preparation of poly(ethylene terephthalate)–SiO2 nanocomposites.* European Polymer Journal, 2006. **42**(5): p. 1128-1134.

282. Reynaud, E., et al., *Nanofillers in polymeric matrix: a study on silica reinforced PA6.* Polymer, 2001. **42**(21): p. 8759-8768.

283. Castrillo, P.D., et al., *Real dispersion of isolated fumed silica nanoparticles in highly filled PMMA prepared by high energy ball milling.* Journal of Colloid and Interface Science, 2007. **308**(2): p. 318-324.

284. González-Benito, J. and G. González-Gaitano, *Interfacial Conformations and Molecular Structure of PMMA in PMMA/Silica Nanocomposites. Effect of High-Energy Ball Milling.* Macromolecules, 2008. **41**(13): p. 4777-4785.

285. Olmos, D., et al., *Crystallization and final morphology of HDPE: Effect of the high energy ball milling and the presence of TiO2 nanoparticles.* Polymer, 2009. **50**(7): p. 1732-1742.

286. Pantaleón, R. and J. González-Benito, *Structure and thermostability of PMMA in PMMA/silica nanocomposites: Effect of high-energy ball milling and the amount of the nanofiller*. Polymer Composites, 2010. **31**(9): p. 1585-1592.

287. Thompson, J., *Integrated Ultra High Density Multi-chip Module Packaging Design*2008: ProQuest.

288. Lee, B. and J. Rives, *Dispersion of alumina powders in nonaqueous media.* Colloids and surfaces, 1991. **56**: p. 25-43.

289. Seelenmeyer, S. and M. Ballauff, *Analysis of surfactants adsorbed onto the surface of latex particles by small-angle X-ray scattering.* Langmuir, 2000. **16**(9): p. 4094-4099.

290. Clarke, J.G., S.R. Wicks, and S.J. Farr, *Surfactant mediated effects in pressurized metered dose inhalers formulated as suspensions. I. Drug/surfactant interactions in a model propellant system.* International journal of pharmaceutics, 1993. **93**(1): p. 221-231.

291. Green, J. and G. Parfitt, *Stability of non-aqueous dispersions. Paper 7. Electrostatic stabilization of concentrated colloidal dispersions.* Colloids and surfaces, 1988. **29**(4): p. 391-402.

292. Singh, B.P., et al., *Stability of dispersions of colloidal alumina particles in aqueous suspensions.* Journal of Colloid and Interface Science, 2005. **291**(1): p. 181-186.

293. Lee, E.S., et al., *Enhanced thermal conductivity of polymer matrix composite via high solids loading of aluminum nitride in epoxy resin.* Journal of the American Ceramic Society, 2008. **91**(4): p. 1169-1174.

294. Pecht, M., et al., *Electronic Packaging Materials and Their Properties*1998: Taylor & Francis.

295. D, X.C.T.P., *Advanced Materials for Thermal Management of Electronic Packaging*2011: Springer New York.

296. Orrhede, M., R. Tolani, and K. Salama, *Elastic constants and thermal expansion of aluminum-SiC metal-matrix composites.* Research in Nondestructive Evaluation, 1996. **8**(1): p. 23-37.

297. McNeilly, K., E. Jost, and P. Sexton. *Effect of Lubricant Solvent System on the Electrical Properties of Silver Filled Polymers*. in *PROCEEDINGS OF THE INTERNATIONAL MICROELECTRONICS CONFERENCE*. 1994. SOCIETY FOR HYBRID MICROELECTRONICS.

298. Buzea, C., I. Pacheco, and K. Robbie, *Nanomaterials and nanoparticles: Sources and toxicity.* Biointerphases, 2007. **2**(4): p. MR17-MR71.

299. Jensen, J., et al., *Brookhaven National Laboratory Selected Cryogenic Data Notebook: Sections I-IX*. Vol. 1. 1980: Brookhaven National Laboratory.

300. Touloukian, Y. and E. Buyco, *Thermophysical Properties of Matter—the TPRC Data Series. Volume 5. Specific Heat-Nonmetallic Solids*, 1970, DTIC Document.

301. Jäckel, M., *Thermal properties of polymer/particle composites at low temperatures.* Cryogenics, 1995. **35**(11): p. 713-716.

302. Haiying, L., K. Jacob, and C.P. Wong. *Improvement of thermal conductivity of underfill materials for electronic packaging*. in *Electronic Components and Technology Conference, 2002. Proceedings. 52nd*. 2002.

303. Jolivet, J.-P., C. Chaneac, and E. Tronc, *Iron oxide chemistry. From molecular clusters to extended solid networks.* Chemical Communications, 2004. **0**(5): p. 481-483.

304. Meier, R.C., et al., *Microfluidic integration of wirebonded microcoils for on-chip applications in nuclear magnetic resonance*. Journal of Micromechanics and Microengineering, 2014. **24**(4): p. 045021.

APPENDIX A: COPYRIGHT PERMISSIONS

A.1 Langmuir Permission

Below is permission for use of material in Chapter 3.

1/22/2015 RightsLink® by Copyright Clearance Center

Copyright Clearance Center RightsLink®

Home | Create Account | Help | Live Chat

ACS Publications Most Trusted. Most Cited. Most Read.

Title: Poly(N-isopropylacrylamide) Cross-Linked Coatings with Phototunable Swelling
Author: Vinicio Carias, Jing Wang, Ryan Toomey
Publication: Langmuir
Publisher: American Chemical Society
Date: Apr 1, 2014
Copyright © 2014, American Chemical Society

LOGIN
If you're a copyright.com user, you can login to RightsLink using your copyright.com credentials. Already a RightsLink user or want to learn more?

PERMISSION/LICENSE IS GRANTED FOR YOUR ORDER AT NO CHARGE

This type of permission/license, instead of the standard Terms & Conditions, is sent to you because no fee is being charged for your order. Please note the following:

- Permission is granted for your request in both print and electronic formats, and translations.
- If figures and/or tables were requested, they may be adapted or used in part.
- Please print this page for your records and send a copy of it to your publisher/graduate school.
- Appropriate credit for the requested material should be given as follows: "Reprinted (adapted) with permission from (COMPLETE REFERENCE CITATION). Copyright (YEAR) American Chemical Society." Insert appropriate information in place of the capitalized words.
- One-time permission is granted only for the use specified in your request. No additional uses are granted (such as derivative works or other editions). For any other uses, please submit a new request.

BACK | CLOSE WINDOW

Copyright © 2015 Copyright Clearance Center, Inc. All Rights Reserved. Privacy statement.
Comments? We would like to hear from you. E-mail us at customercare@copyright.com

A.2 IEEE Transactions on Components, Packaging and Manufacturing Technology Permission

Below is permission for use of material in Chapter 5.

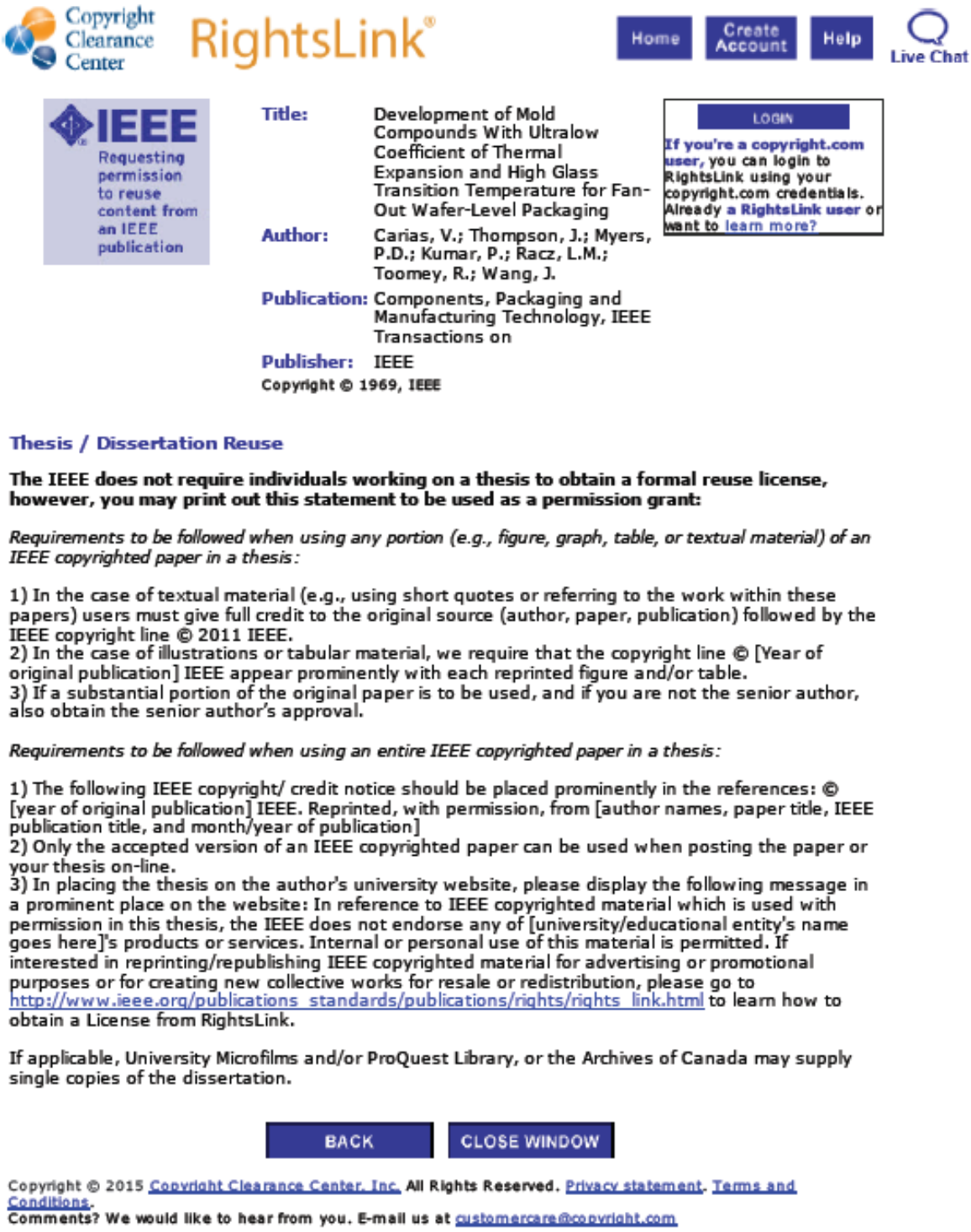

Copyright Clearance Center RightsLink®

Home | Create Account | Help | Live Chat

IEEE
Requesting permission to reuse content from an IEEE publication

Title: Development of Mold Compounds With Ultralow Coefficient of Thermal Expansion and High Glass Transition Temperature for Fan-Out Wafer-Level Packaging

Author: Carias, V.; Thompson, J.; Myers, P.D.; Kumar, P.; Racz, L.M.; Toomey, R.; Wang, J.

Publication: Components, Packaging and Manufacturing Technology, IEEE Transactions on

Publisher: IEEE

Copyright © 1969, IEEE

LOGIN

If you're a copyright.com user, you can login to RightsLink using your copyright.com credentials. Already a RightsLink user or want to learn more?

Thesis / Dissertation Reuse

The IEEE does not require individuals working on a thesis to obtain a formal reuse license, however, you may print out this statement to be used as a permission grant:

Requirements to be followed when using any portion (e.g., figure, graph, table, or textual material) of an IEEE copyrighted paper in a thesis:

1) In the case of textual material (e.g., using short quotes or referring to the work within these papers) users must give full credit to the original source (author, paper, publication) followed by the IEEE copyright line © 2011 IEEE.
2) In the case of illustrations or tabular material, we require that the copyright line © [Year of original publication] IEEE appear prominently with each reprinted figure and/or table.
3) If a substantial portion of the original paper is to be used, and if you are not the senior author, also obtain the senior author's approval.

Requirements to be followed when using an entire IEEE copyrighted paper in a thesis:

1) The following IEEE copyright/ credit notice should be placed prominently in the references: © [year of original publication] IEEE. Reprinted, with permission, from [author names, paper title, IEEE publication title, and month/year of publication]
2) Only the accepted version of an IEEE copyrighted paper can be used when posting the paper or your thesis on-line.
3) In placing the thesis on the author's university website, please display the following message in a prominent place on the website: In reference to IEEE copyrighted material which is used with permission in this thesis, the IEEE does not endorse any of [university/educational entity's name goes here]'s products or services. Internal or personal use of this material is permitted. If interested in reprinting/republishing IEEE copyrighted material for advertising or promotional purposes or for creating new collective works for resale or redistribution, please go to http://www.ieee.org/publications_standards/publications/rights/rights_link.html to learn how to obtain a License from RightsLink.

If applicable, University Microfilms and/or ProQuest Library, or the Archives of Canada may supply single copies of the dissertation.

BACK | CLOSE WINDOW

Copyright © 2015 Copyright Clearance Center, Inc. All Rights Reserved. Privacy statement. Terms and Conditions.
Comments? We would like to hear from you. E-mail us at customercare@copyright.com

APPENDIX B: PNIPAAm - 3 WT% MaBP SYNTHESIS PROCEDURE

B.1 Generating NIPAAm Crystals

1. Measure 5g of N-isopropylacrylamide
    a. This is from the commercial bottle
2. Place the 5g of N-Isopropylacrylamide in a 250 flask
3. Fill ¾ of the flask with hexane
4. Place the flask on a hot plate to dissolve the NIPAAm powder
    a. Use medium heat (~170°C)
5. After about 10 minutes take it off the hot plate and let it sit on the counter to cool down
    a. Make sure to cover the flask with Parafilm
6. Scratch the bottom of the flask with a spatula
    a. It is important to do this once the solution liquefies, Do not wait for fermentation to occur
    b. Recover the flask with Parafilm
7. Leave the mixture out on the counter overnight
8. Filter the solution that was left overnight

Figure B.1: Filtering process

a. Use a flask, a filtering funnel, and a glass microfiber filter

b. Remove all the liquid, leaving the crystals behind

9. Place the crystals inside a Schlenk tube

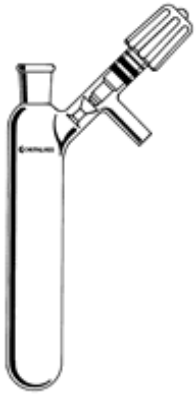

Figure B.2: Schlenk tube

a. Cover the Schlenk tube with a rubber septum

Figure B.3: Rubber septum

b. Dry the crystals using the vacuum pump

10. Use liquid nitrogen to freeze the crystals in the Schlenk tube

a. Wrap the Schlenk tube with aluminum foil

b. Dip the Schlenk tube in an insulating liquid nitrogen container until the crystals freeze

11. Turn the vacuum pump on and let it run for about 10 minutes

12. Open the valves in order

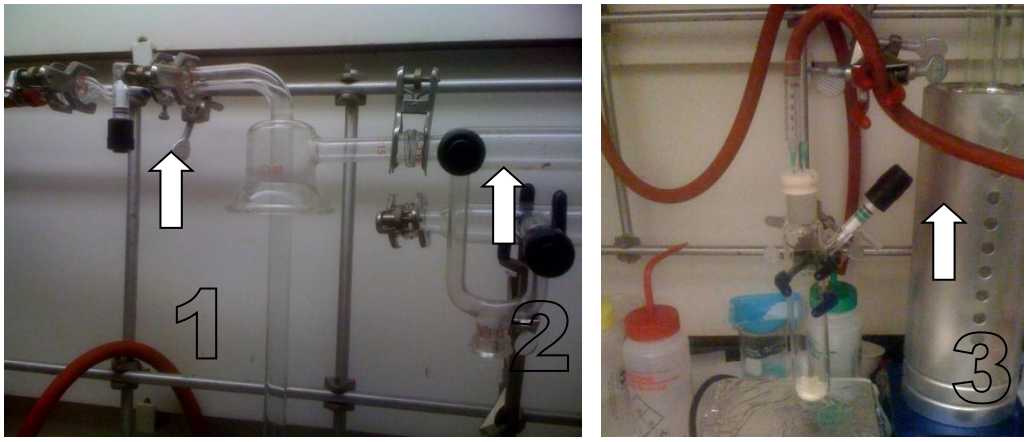

Figure B.4: Vacuum pump valves

a. Slowly open each valve in sequence

b. Since the crystals are almost a solid, the valve on the Schlenk tube may be opened all the way

i. The crystals should be completely dry

13. Once the crystals are completely dry, take them out of the Schlenk tube and weigh them

a. The first time we obtained 4.7444 g of crystals

14. At this point you want to calculate the values to start the polymerization process

B.2 Polymerization Process

Before you start anything, turn the water bath to 72°C to get it ready for later on in the polymerization process!!! Also, make sure that you have previously distilled (Day before) more than 20 mL of dioxane

B.2.1 Calculations

Determine the calculations according to the amount of crystals obtained. We will work with 4.75g of NIPAAm

B.2.1.1 Moles of NIPAAm

Table B.1: Moles of NIPAAm

4.75 g of NIPAAm	1 mole	= 0.04197596 moles of NIPAAm
	113.16 g of NIPAAm	

B.2.1.2 % Moles of NIPAAm

0.041976 * 0.03 = 0.00125928 moles of NIPAAm

B.2.1.3 Grams of MaBP with Respect to 3% of NIPAAm

Table B.2: Grams of MaBP with respect to 3% of NIPAAm

0.00125928 moles of NIPAAm	257 g of MaBP	= 0.32363468 g (323.6 mg) of MaBP
	1 mole	

B.2.1.4 0.5% Moles of NIPAAm

0.041976 * 0.005 = 0.00020988 moles of NIPAAm

B.2.1.5 Grams of Initiator (AIBN) with Respect to 0.5% of NIPAAm

Table B.3: Grams of AIBN with respect to 0.5% of NIPAAm

0.00020988 moles of NIPAAm	164.21 g of AIBN	= 0.03446436 g (34.5 mg) of AIBN
	1 mole	

B.3 Procedure

1. In a clean schlenk tube, place the measured NIPAAm crystals (4.75 g of NIPAAm)
2. Include the measured amount of MaBP in the schlenk tube (323.6 mg of MaBP)
3. Include the measured amount of initiator (AIBN) in the schlenk tube (34.5 mg of AIBN)
4. Add 20 mL of distilled dioxane to the mixture in the schlenk tube
5. Once the mixture is complete, cover the schlenk tube with a rubber septum and shake it up and down by hand
    a. This is done until the mixture is completely dissolved
    b. This could take a few minutes
6. Once the solution is completely dissolved, dip the Schlenk tube in an insulating liquid nitrogen container until the solution freezes
7. Take the Schlenk tube out of the liquid nitrogen and attach the vacuum pump hose to the tube opening and wait until a little liquid forms at the bottom
8. Attach the nitrogen gas hose to the Schlenk tube with a needle inserted from the top. With the nitrogen flowing, close the needle with a thumb for a few seconds then release. This procedure generates pressure and gets rid of air bubbles.
    a. Be careful with keeping the needle closed for too long because the pressure may force the top to pop out!
    b. Wait for the solution to become a liquid again.
9. Repeat steps 6 through 8
10. At this point the mixture is a liquid again
    a. This solution should have no bubbles
11. Cover the Schlenk tube opening with Parafilm

12. Place the Schlenk tube in the water bath
    a. The temperature should be at 72°C
    b. Leave the Schlenk tube in the water bath for 20 hours
13. After 20 hours a viscous solution should be observed
14. Follow steps 10 through 12 in section B.1 Generating NIPAAm Crystals
    a. This will remove most of the dioxane in the mixture
    b. This will also minimize the dioxane peak in the NMR spectrum
15. Next step is to precipitate

B.4 Precipitation

1. Place 200 mL of diethyl ether in a beaker
2. Insert a magnetic stir bar in the beaker
3. Set the beaker on a hot plate
    a. Heat at 0°C
    b. Stir between 600 - 800 rpm
4. Place 2 - 4 mL of acetone in a small test tube
5. Add the small amount of acetone to the Schlenk tube
    a. This will help dissolve the polymer
6. Place the Schlenk tube mixture into the 200 mL of diethyl ether
7. Filter the solution in the Schlenk tube
    a. Refer to Figure B.1: Filtering Process
    b. Use a flask, a filtering funnel, and a glass microfiber filter
    c. Remove all the liquid, leaving the polymer behind
8. Place the filtered polymer in a clean Schlenk tube

9. Wrap the tube with aluminum foil and close it with a rubber septum
10. Load the Dewar flask with liquid nitrogen
11. Once the Dewar flask is full, turn the vacuum pump on
    a. Let the vacuum pump run for about 10 minutes prior to using it
12. Dip the Schlenk tube in an insulating liquid nitrogen container until the solution freezes and liquid is no longer seen
13. Open the vacuum valves in order
    a. Refer to Figure B.4:Vacuum Pump Valves
    b. Slowly open each valve in sequence
    c. Since the crystals are almost a solid, the valve on the Schlenk tube may be opened all the way
14. Wait until solution is completely dry
    a. This process can take up to 24 hrs.
    b. After about 7 hours, refill the Dewar flask with liquid nitrogen

APPENDIX C: Fe_3O_4 NANOPARTICLE SYNTHESIS PROCEDURE

1. On weighing paper weigh 3.5317g of iron salt (Iron(III) Acetylacetonate) ≥ 99.9% metals basis
    a. ±0.0010 or ±0.0020 is okay for this measurement
2. Transfer the iron salt into a 500ml 3 neck flask
    a. Use weighing paper to generate a funnel to pour the iron salt into the 3 neck flask
    b. See Figure C.1: Using a Paper Funnel to Pour Iron Salt into a 3 Neck Flask

Figure C.1: Using a paper funnel to pour iron salt into a 3 neck flask

3. Pipette 50ml of Benzyl Ether 99% and pour it into the 3 neck flask
    a. Try not to touch the 3 neck flask with the pipette
    b. See Figure C.2: Pipetting Solution into a 3 Neck Flask

Figure C.2: Pipetting solution into a 3 neck flask

4. Pipette 50ml of Oleylamine and pour it into the 3 neck flask
    a. See Figure C.2: Pipetting Solution into a 3 Neck Flask
5. Add 10 porous boiling chips into the 3 neck flask
    a. This will help obtain a smoother boil
6. Add a magnetic bar of about 1 inch in length into the 3 neck flask
7. Add Teflon tape to the end of the condenser
    a. Due to high temperatures, it is hard to separate the condenser with the 3 neck flask after synthesis. Therefore the use of Teflon tape makes this separation easier
    b. See Figure C.3: Teflon Tape on the Condenser

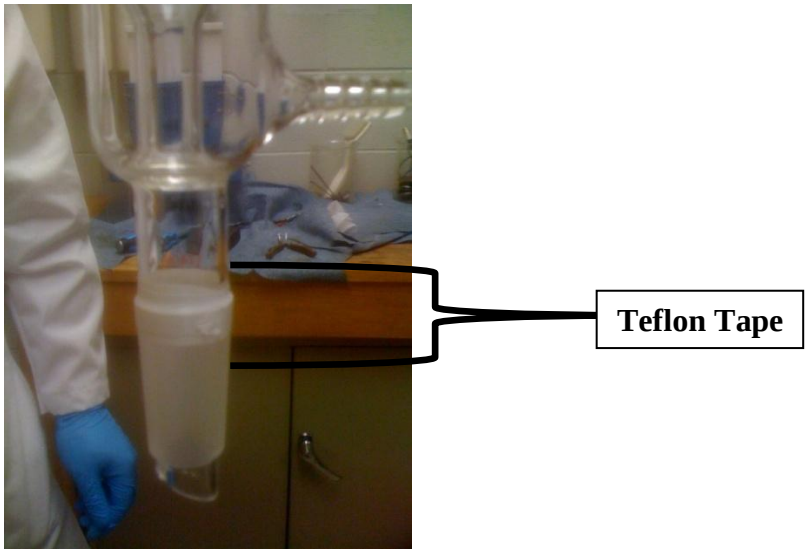

Figure C.3: Teflon tape on the condenser

8. Set a hot plate inside the fume hood. Place the 3 neck flask and a controllable heat pad over the hot plate
    a. Set the hot plate to a stir speed of about 7.5

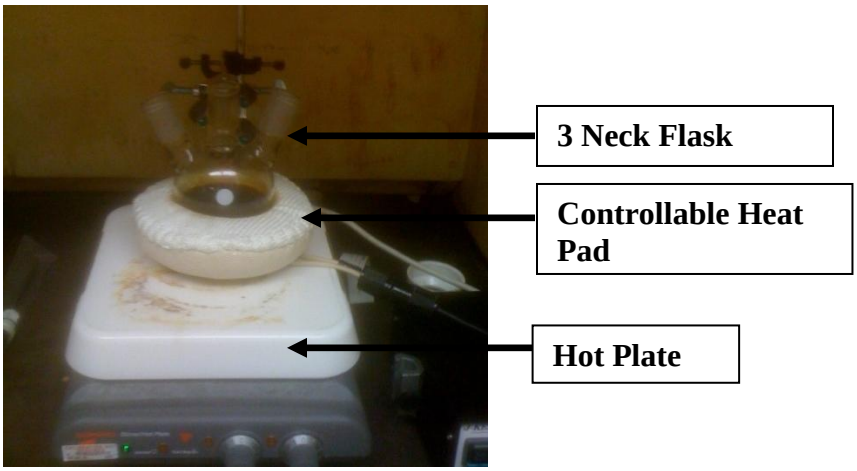

Figure C.4: Initial setup

9. Insert the controller thermocouple in the right flask neck
    a. See Figure C.5: Setup II
10. Connect the controllable heat pad to the controller

a. See Figure C.5: Setup II

11. Place a rubber seal to the left flask neck

a. See Figure C.5: Setup II

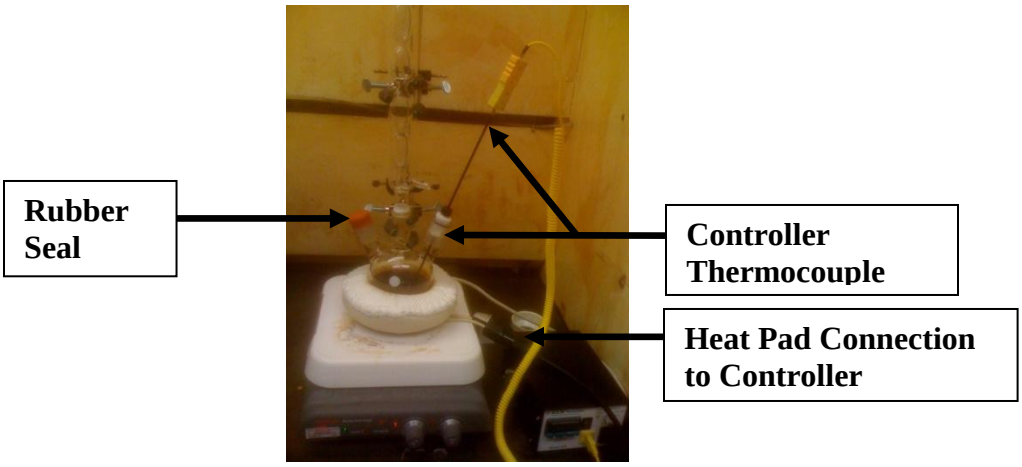

Figure C.5: Setup II

12. Place a rubber seal to the top of the condenser with 3 needles

a. This will slowly release pressure buildup in the condenser

b. See Figure C.6: Setup III

13. Insert an argon releasing needle to the rubber seal on the left side of the 3 neck flask

a. This will eliminate any oxygen inside the flask

b. Before inserting the needle, place the needle in a small tube containing acetone

i. Look for a small amount of bubbles

ii. Now insert into the rubber seal

c. See Figure C.6: Setup III

14. Connect the water hoses to the condenser

a. Water in is attached to the lower condenser opening

b. Water out is attached to the upper condenser opening

i. The other end of the water out hose goes into the sink

c. Once the hoses are well attached, open the water valve

i. A continuous water flow should be obtained

ii. The water pressure should not be excessive. This could force the hoses to pop out of place

d. See Figure C.6: Setup III

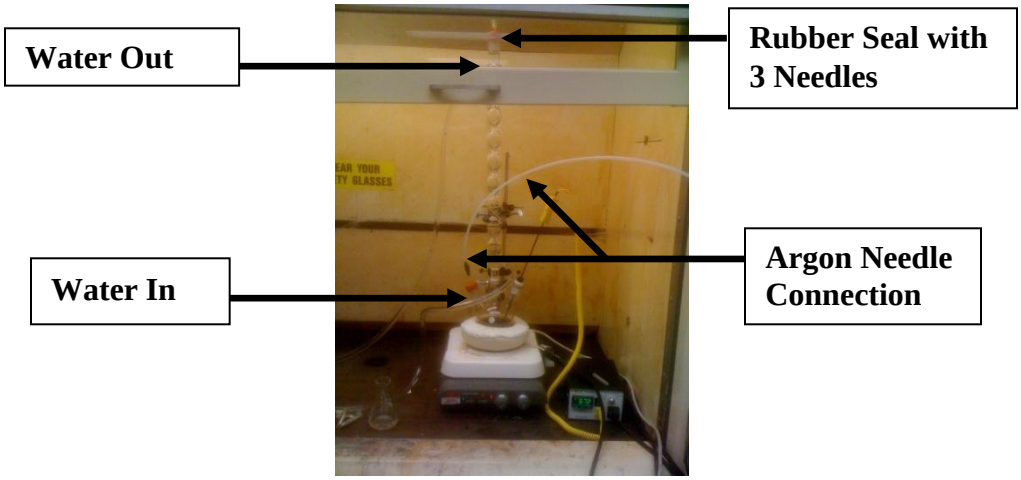

Figure C.6: Setup III

15. Using the controller, set the temperature to 110°C

a. Also, set the volume to 2 L

i. This will allow the temperature to reach its final temperature at a much faster rate

16. Once the temperature reaches 110°C, wait for 1 hour

17. Raise the temperature to 300°C, wait for 2 hours

18. Remove the heat pad

a. Let the solution cool down

i. Rest the flask on something firm while it cools down

b. Let the solution rest until the controller reads 50°C

c. See Figure C.7: Cooling Position

Figure C.7: Cooling position

19. Set up the nanoparticle cleaning station

a. This includes the centrifuge and the ultrasonic bath

20. Add 200ml of Ethanol 200 proof to the cooled solution

a. Use a long syringe

b. See Figure C.8: Adding Ethanol to the Cooled Solution

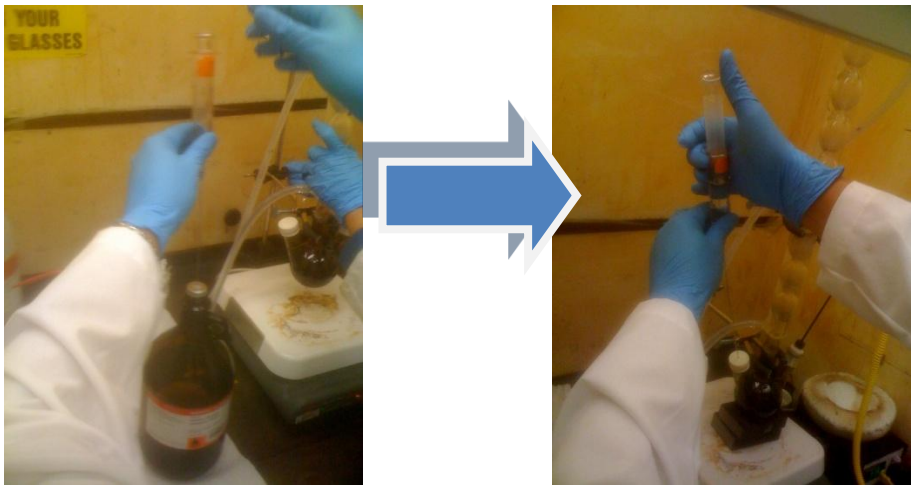

Figure C.8: Adding ethanol to the cooled solution

21. With the use of a glass rod, pour the solution into vials

    a. See Figure C.9: Pouring Solution into Vials with Glass Rod

Figure C.9: Pouring solution into vials with glass rod

22. Pour 12ml of solution into 12 vials. Place the 6 vials in the centrifuge

    a. Do not fill the vials to the top

    b. Set the time to 5 minutes

    c. Set the RPM to 5000

23. When the vials come out of the centrifuge, discard the liquid in a waste bottle leaving the solid nanoparticles behind

    a. Leave the 6 vials on the side

24. Place the remaining 6 vials in the centrifuge

    a. When the vials come out of the centrifuge, discard the liquid in a waste bottle leaving the solid nanoparticles behind

25. At this point there are 12 vials with discarded liquid

    a. Add 6ml of ethanol to each vial

b. Close the vials followed by placing parafilm around the cap

c. Place them in the ultrasonic bath until all the particles are removed from the inner wall of the vials

26. Merge 2 vials into 1 vial. Do this for the remaining vials

a. At this point there should be 6 full vials

b. Centrifuge the 6 vials

c. When the vials come out of the centrifuge, discard the liquid in a waste bottle leaving the solid nanoparticles behind

27. At this point there are 6 vials with discarded liquid

a. Add 6ml of ethanol to each vial

b. Close the vials followed by placing parafilm around the cap

c. Place them in the ultrasonic bath until all the particles are removed from the inner wall of the vial

28. Merge 2 vials into 1 vial. Do this for the remaining vials

a. At this point there should be 3 full vials

b. Centrifuge the 3 vials

c. When the vials come out of the centrifuge, discard the liquid in a waste bottle leaving the solid nanoparticles behind

29. At this point there are 3 vials with discarded liquid

a. Add 6ml of ethanol to each vial

b. Close the vials followed by placing parafilm around the cap

c. Place them in the ultrasonic bath until all the particles are removed from the inner wall of the vial

d. The particles in these 3 vials have gone through a complete cleaning

30. The remaining solution in the 3 neck flask can be placed in the empty vials

    a. These particles have to go through the aforementioned 3 step washing process

31. There may be no more solution in the 3 neck flask, but the magnetic bar is covered with nanoparticles. Therefore, add about 10ml of ethanol and use a dropper to rinse the magnetic bar and to take out the remaining solution.

    a. See Figure C.10: Using a Dropper to Clean the Magnetic Bar

    b. Fill remaining vials with this obtained solution

    c. Small amounts of ethanol may be used to completely clean the magnetic bar

Figure C.10: Using a dropper to clean the magnetic bar

32. Add small amounts of hexane to the clean nanoparticles in the vials

    a. Remove the nanoparticles in hexane and place them in a storing container

33. With the use of a dropper, add 5 drops of Oleylamine to the final solution

34. With the use of a dropper, add 5 drops of Oleic Acid to the final solution

35. Cover the storing container with Parafilm

ABOUT THE AUTHOR

Vinicio Carias received a B.S. degree in electrical engineering from Northeastern University, Boston, MA in 2009, and a M.S. degree in biomedical engineering and a graduate certificate in Entrepreneurship from the University of South Florida (USF) in 2011 and 2013, respectively.

In 2012, Vinicio was selected as a Leadership Fellow for the Graduate School's Doctoral Student Leadership Institute, which develops future leaders. That same year, Vinicio was selected to be a Graduate Student Ambassador to represent the College of Engineering within the Graduate School and throughout the university community. Here he served in an advisory capacity to the Graduate School Dean, operated as an official student representative for the Graduate School, and mentored new graduate students. From July 2010 to July 2012, Vinicio was a project leader for a Draper Laboratory University Research & Development (URAD) project titled "Implementation of Miniaturized On-Chip Passives and Antennas Based on Injection-Moldable Nanocomposites for Multi-Chip-Module (MCM) Technology". For his work with this project, Vinicio was recognized by the Florida High Tech Corridor Council's (FHTCC) Matching Grants Research Program (MGRP) for excellence in student research.

Vinicio has earned several awards and honors. He is a National Science Foundation (NSF) Bridge to the Doctorate Fellow and a Fulbright Scholar. Through the Fulbright award he was able to carry out his doctoral research at the University of Freiburg - Institute for Microsystems Technology (IMTEK), Freiburg, Germany (2013-2014).